

**ENABLING TWO-DIMENSIONAL FOURIER TRANSFORM ELECTRONIC
SPECTROSCOPY ON QUANTUM DOTS**

by

ROBERT JOHN HILL JR.

B.S., Purdue University, 2000

M.S., University of Colorado, 2008

A thesis submitted to the
Faculty of the Graduate School of the
University of Colorado in partial fulfillment
of the requirement for the degree of
Doctor of Philosophy
Department of Physics

2013

This thesis entitled:

Enabling Two-Dimensional Fourier Transform Electronic Spectroscopy on Quantum Dots

written by Robert J. Hill Jr.

has been approved for the Department of Physics

Henry C. Kapteyn

David M. Jonas

Date_____

The final copy of this thesis has been examined by the signatories, and we find that both the content and the form meet acceptable presentation standards of scholarly work in the above-mentioned discipline.

Hill Jr., Robert John (Ph.D., Physics)

Enabling Two-Dimensional Fourier Transform Electronic Spectroscopy on Quantum Dots

Thesis directed by Professor Henry C. Kapteyn

Colloidal semiconductor nanocrystals exhibit unique properties not seen in their bulk counterparts. Quantum confinement of carriers causes a size-tunable bandgap, making them attractive candidates for solar cells. Fundamental understanding of their spectra and carrier dynamics is obscured by inhomogeneous broadening arising from the size distribution. Because quantum dots have long excited state lifetimes and are sensitive to both air and moisture, there are many potential artifacts in femtosecond experiments. Two-dimensional electronic spectroscopy promises insight into the photo-physics, but required key instrumental advances. Optics that can process a broad bandwidth without distortion are required for a two-dimensional optical spectrometer. To control pathlength differences for femtosecond time delays, hollow retro-reflectors are used on actively stabilized delay lines in interferometers. The fabrication of rigid, lightweight, precision hollow rooftop retroreflectors that allow beams to be stacked while preserving polarization is described. The rigidity and low mass enable active stabilization of an interferometer to within 0.6 nm rms displacement, while the return beam deviation is sufficient for Fourier transform spectroscopy with a frequency precision of better than 1 cm^{-1} . Keeping samples oxygen and moisture free while providing fresh sample between laser shots is challenging in an interferometer. A low-vibration spinning sample cell was designed and built to keep samples oxygen free for days while allowing active stabilization of interferometer displacement to $\sim 1 \text{ nm}$. Combining these technologies has enabled 2D short-wave infrared spectroscopy on colloidal PbSe nanocrystals. 2D spectra demonstrate the advantages of this key instrumentation while providing valuable insight into the low-lying electronic states of colloidal quantum dots.

ACKNOWLEDGMENTS

I cannot thank my wife Carolyn enough for her years of support and sacrifice throughout this experience. She left her dream job as a health physicist so I could pursue my aspirations here at CU, Boulder. Since then, she been nothing but supportive when I needed it: the glue in our household when research and military responsibilities rendered me a proxy parent. She is the best companion a person could hope for.

I would like to thank David Jonas for allowing me to research a fascinating and vibrant topic under his guidance. This guidance has taught me that details, often overlooked, make a huge difference in scientific progress. It is often his attention to detail that seems to afford the greatest insights and understanding. Questioning what others have often assumed has demonstrated what it means to do quality science and what I should strive for. David's attention to detail extends beyond his research, as he takes all of his responsibilities seriously, and it shows in his teaching and interaction with others. With respect to people, it is the little things that matter most and that is part of his essence.

Henry Kapteyn has graciously always been available as an adviser to provide guidance when needed. In addition to his own scientific accomplishments, I have seen how he has been a catalyst for research groups around him, even at times when not formally collaborative. I was also fortunate enough to take an engaging and enjoyable lasers class from him with a wealth of practical information that I use all the time.

There are a number of people in my lab from whom I have been fortunate to learn from, work with, and count as friends. I would like to thank friends who I will miss dearly: Mike Yetzbacher was a natural teacher, always there to invest time in the younger graduate students. Trevor Courtney taught me the rewards of clear communication, as is evidenced by his pristine

notebooks--they are a labor of love. Trevor has also served as a sounding board for problems, frustrations, and insight. Bill Peters has a wealth of chemistry knowledge he is always happy to share. He has also helped pull me out of a scrape or two. As a friend, I appreciate his sound advice to me as a new parent. I will miss our many coffee discussions and his *uncountable* enthusiasm for quantum information. Danielle Buckley has been a good source of information with her knowledge of thin films and synthesis. She has brought to the lab just enough Texas to keep the office lively. Sam Park has been tremendously helpful in collecting 2D data on the spinning cell and quantum dots, and was kind enough to put up with a grumpy old man. Austin Spencer's enthusiasm for electronics and computers, as well perspective, have always lent to good discussion. I will miss hearing his recollection of Futurama episodes. Dmitry Baranov and Vivek Tiwari have been great to work with and always keep a good sense of humor. I will not forget many useful discussions with Byung-moon Cho, and his helping a cripple hobble through the cobbled streets of Italy. Cheers to finding the world's most expensive glass of orange juice and great memories!

I would like to thank other friends: Terry Brown for his help with the JILA loop filter; James Fung-a-fat, Carl Saurer, Ken Smith, and Don David for many great discussions on electronics. Also, my appreciation to Tracey Keep, Yehor Nocikov, and Todd Asnicar for tips on how to work with glass. I would like to thank Kim Hagen, Blaine Horner, Sid Gustavson, Hans Green, Tracey Keep, and Kels for machine shop training and advice. Thanks also to David Alchenberger for introducing me to the Fizeau interferometer and the diamond saw. I owe Rich Shoemaker a big thank you for loaning us the disk drive that made taking data possible.

Dana Anderson and Kelvin Wagner deserve thanks for a great course on advanced optics. I would also like to thank Jiangbo Gao of NREL for coating the substrates with thin films of

quantum dots and Matt Beard for helping me take data on the thin films. This work would not be possible without the useful collaborative efforts through the EFRC.

Finally, I would like to thank my parents, family, and grandmother for their years of love and support. Especially my dad, whose love for mathematics, puzzles, and taking things apart sparked a certain degree of curiosity in my view of the world.

TABLE OF CONTENTS

CHAPTER 1: INTRODUCTION	1
1.1 Quantum Dot Overview	1
1.1.1 Quantum Dots	1
1.1.2 Excitons.....	1
1.2 Research	5
1.2.1 A Case for Lead Chalcogenide Quantum Dots.....	5
1.2.2 Brief Introduction to Transient Absorption Pump-Probe Spectroscopy.....	6
1.2.3 Early Research	8
1.2.4 Absolute Signal Strength	9
1.3 Sample Exchange Under Oxygen-Free Conditions.....	10
1.4 Retroreflectors and Contributions to 2D Spectrometer	14
1.5 First Oxygen-Free and Sample Exchanged 2D Spectroscopy on Quantum Dots	16
1.6 Organization of Thesis	23
CHAPTER 2: LIGHTWEIGHT HOLLOW ROOFTOP MIRRORS FOR STABILIZED INTERFEROMETRY	31
2.1 Introduction	31
2.2 Experimental.....	32
2.3 Results	40
2.4 Conclusions	42
CHAPTER 3: INTERFEROMETRICALLY STABLE, HIGH-SPEED ROTATING SAMPLE CELL FOR AIR-FREE SOLUTIONS AND FILMS	46
3.1 Introduction	46
3.2 Construction	47
3.3 Experiments and Quantification	53
3.4 Conclusions	56
CHAPTER 4: FIRST 2D SPECTRUM ON OXYGEN-FREE AND SAMPLE EXCHANGED COLLOIDAL QUANTUM DOTS	61
4.1 Introduction	61
4.2 Experimental Setup	62
4.3 Pump-Probe Experiments on Quantum Dots	64
4.4 Two-Dimensional Spectroscopy on Quantum Dots	67
4.4.1 2D Colloidal Quantum Dots Measurements	67
4.4.2 Experimental Condition	68
4.4.3 Data Processing.....	69
4.4.4 Results.....	70
4.5 Pump-Probe Experiments on PbSe Thin-Film Dots	
4.5.1 Experimental Preparation.....	72
4.5.2 Experimental Conditions	73
4.5.3 Results.....	74
4.6 Conclusions	75

BIBLIOGRAPHY 80

APPENDIX A: HOLLOW ROOFTOP MIRROR CONSTRUCTION 92

APPENDIX B: FLUID SAMPLE CELL CONSTRUCTION 103

LIST OF FIGURES

Fig. 1.1. Channels between states	04
Fig. 1.2. Brillouin zone of lead chalcogenides	06
Fig. 1.3. Transient absorption experiment	07
Fig. 1.4. Chemical structure of DCOCI.....	08
Fig. 1.5. Evolution of spinner sample cell design.....	14
Fig. 1.6. 2D Spectroscopy field sample interaction time sequence.	19
Fig. 1.7. Three-level coupling.....	21
Fig. 1.8. Real part of simulated 2D Fourier transform spectrum.....	21
Fig. 1.9. 2D Sagnac interferometer for optimized interference detection of 2D spectra in the pump-probe geometry	23
Fig. 2.1. Bonding the retroreflector angle.....	35
Fig. 2.2. Adding side supports.....	37
Fig. 2.3. Mounting the hollow rooftop mirror to the aluminum base.	39
Fig. 3.1. Sample spinner assembly	49
Fig. 3.2. Hard disk glass substrate transmission spectra.....	50
Fig. 4.1. Schematic of Sagnac Interferometer	64
Fig. 4.2. NOPA spectrum for pump-probe experiment on PbSe quantum dots	65
Fig. 4.3. Absorption and photoluminescence spectra of 3 nm quantum dots	66
Fig. 4.4. Pump-probe transients of 1136 nm PbSe quantum dots	67
Fig. 4.5. 2D FT optical spectra comparison between spinning and static sample cells.....	71
Fig. 4.6. Projection in 2D optical spectrum onto ω_t	72
Fig. 4.7. Absorption spectra of 300 nm thick PbSe thin films.....	73
Fig. 4.8. Pump-probe comparison of spinning vs. static thin films	75
Fig. A.1. Cutting the retroreflector glass	92
Fig. A.2. Aligning the retroreflector glass for cutting	93
Fig. A.3. The retroreflector jig.....	94
Fig. A.4. Inside the Zygo® Fizeau interferometer	95
Fig. A.5. Rough retroreflector alignment	97
Fig. A.6. Fine retroreflector alignment	98
Fig. A.7. Completed Retroreflector 1 surface.....	100
Fig. A.8. Completed Retroreflector 2 surface.....	101
Fig. A.9. The effects of measurement masks on reporting	102
Fig. B.1. Electrochemical removal of hard disk drive coatings.....	104
Fig. B.2. Comparison between glass substrate surfaces.	105
Fig. B.3. Ring alignment for fluid cell.....	106
Fig. B.4. Bonding the first substrate in fluid cell.....	106
Fig. B.5. Bonding the second substrate in fluid cell.....	107
Fig. B.6. Linear absorption spectrum testing for oxygen or water in quantum dots	108

CHAPTER 1: INTRODUCTION

1.1 QUANTUM DOT OVERVIEW

1.1.1 Quantum dots

Quantum dots are nanometer-scale semiconductor crystals that have their surfaces passivated so that charge carriers are spatially confined in three dimensions; quantum dots are synthetic realizations of the quantum mechanical particle-in-a-box. Nanocrystal quantum confinement effects were first understood for quantum dots embedded in a glass-matrix by Ekimov and colleagues in 1980(1) and in colloidal solution a few years later by Brus.(2) An increasing interest in semiconductor nanocrystals within the solar energy research community started in 2004, when Schaller and Klimov, while investigating PbSe quantum dots as a laser gain medium,(3, 4) reported that singly excited dots whose carriers were excited with photons having energy of three times the bandgap had a transient absorption decay time commensurate with doubly excited quantum dots.(5) Before discussing Schaller and Klimov's interpretation of their data, it is worth discussing what an exciton is and how it is formed.

1.1.2 Excitons

In bulk semiconductor materials, if a valence band electron has sufficient energy to be removed from a site in the crystal lattice, but not enough energy to escape the Coulomb attraction to the positively charged *hole* created at that former site, a Wannier exciton is formed. Under the effective mass approximation, charge carriers (electrons and holes) possess an effective mass set by the inverse curvature (second derivative) of the band energy as a function of the carrier wave-vector at the excitation wavelength. The exciton has hydrogenic wavefunctions and energy levels in which the electron and hole orbit each other in a reduced

center-of-effective-mass frame. Because the high dielectric constant reduces the Coulomb attraction, Wannier excitons sample a relatively large path through a semiconductor crystal at their Bohr radius, averaging electro-optical properties over several unit cells.

In molecular crystals, the dielectric constant is smaller, so the Coulomb attraction is stronger, resulting in carriers confined to the same molecule (Frenkel excitons). The exciton is still mobile, and the coupling between molecules in the crystal can still delocalize a Frenkel exciton if the crystal is sufficiently ordered. A quantum dot is a semiconductor nanocrystal smaller than the Bohr exciton radius. Quantum dot excitons do not fit cleanly into either the Wannier or Frenkel exciton category. All excitons are overall charge neutral. Like a Frenkel exciton, quantum dot excitons have overlapping electron and hole wavefunctions and are thus charge neutral on a finer scale. Confinement energy in a quantum dot is marked by a blue shift relative to bulk exciton absorption energy; this confinement energy is usually much greater than Coulombic coupling. As a consequence, the main contribution to electron-hole correlation may not come from Coulombic coupling. Therefore confinement is closer to a “particle in a spherical box” than a “modified hydrogenic model” (using effective masses and bulk-property dielectric constants) used for the Wannier and Frenkel excitons. Unlike a Frenkel exciton, the electron-hole pair center of mass is not confined to a unit cell in quantum dots. A second aspect to quantum dots making them uniquely different from the Frenkel exciton is the high dielectric coefficients ($\epsilon_o = 204$ for PbSe and 169 for PbS while $\epsilon_\infty = 23$ and 17, for PbSe and PbS respectively)(6) that make the quantum dot exciton binding energy much less than that of a Frenkel exciton so that quantum dot excitons can easily dissociate at an interface.

A bi-exciton is a state in which two electron-hole pairs are excited, for example by a bandgap photo-excitation of a quantum dot that already has an exciton. Bi-excitons can yield hot

excitons through a process known as Auger recombination, when an electron recombines with a hole and transfers the recombination energy to another electron or hole. Measurement of the bi-exciton lifetime requires consideration of absorption statistics in low fluence experiments. If the absorption events in materials are independent of each other, the excitation probability is assumed to follow Poisson statistics. As independent events, there is a possibility of two-photon absorption by the same quantum dot. Such multi-photon absorption becomes more pronounced at higher photon fluences. The absorption of two photons produces two excitons, or a bi-exciton. At low fluence and high photon energy, one would not expect a significant fraction of bi-excitons due to Poisson statistics.

Bi-excitons possess a faster decay rate than a single exciton. Schaller and Klimov reported that absorption of a single photon with energy more than three times the bandgap produced the Auger lifetime decay signature of bi-excitons(5) as measured after two photon excitation at the bandgap. Thus, Schaller and Klimov interpreted their results as evidence for carrier multiplication, in which absorption of a single high energy photon excites one high energy (hotter) exciton and the high energy exciton generates another exciton. This bi-exciton state then decays via Auger recombination (see states in Fig 1.1). This process is often termed multiple exciton generation (MEG) due to the confined carriers at bandgap in the final product, but this name may give a possibly wrong impression of correlated motion between electron and hole high above the bandgap. With energy greater than exciton ionization energy in bulk, the hot electron and hole may be spatially overlapped by virtue of the finite size of the nanocrystal, but possess enough kinetic energy with little Coulombic potential energy to correlate them, so they may be essentially uncorrelated.

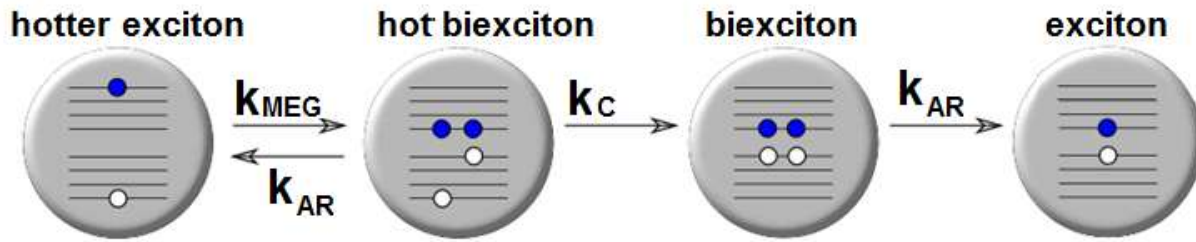


Fig 1.1 Channels between states, where k_{AR} represents an Auger recombination rate, k_{MEG} represents an multiple exciton generation, k_C represents a hot biexciton cooling rate and k_T represents a bi-exciton recombination rate. How long these states remain and their coupling strengths remain an active area of research in quantum dots. A set of figures may be generated for the hole that is the horizontally symmetric in population about the band gap.

Over ten years prior to Schaller and Klimov's experiment, Kolodinski and Queisser reported generating higher than unity quantum efficiency in bulk silicon and attributed it to impact ionization.(7) Neither the bulk silicon result nor Schaller and Klimov's result can be directly useful for solar cells due to the UV light required and the low solar output at UV frequencies. However, they provided materials for investigating carrier multiplication as a means to increase photocurrent in quantum dot photovoltaics.(8) The mechanism of carrier multiplication in quantum dots is not yet known.

There is a possibility that two artifacts may account for the initial reports which cited higher MEG yields than later reports: higher excitation probability at the front of the sample cell(9) and/or photo-excitation of the charged dots (previously thought to be relaxed).(10) Nonetheless, reports of excess photocurrent(11) and a solar cell with a certified external quantum efficiency greater than 100% for near-ultraviolet light(12) provide motivation for carefully eliminating artifacts, probing the dynamics of electron-hole pairs excited by photons well above the bandgap, and improving our understanding of quantum dot structure.

1.2 RESEARCH

1.2.1 A Case for Lead Chalcogenide Quantum Dots

PbS and PbSe have a number of interesting features that make them a desirable system for study. MEG was reported to exist in these systems with a higher efficiency than other binary semiconductor nanocrystals.(13, 14) Furthermore, since MEG was claimed to occur at two to three times bandgap,(5) and since PbS and PbSe both have low energy bandgaps, there is a greater domain over which the size can be tuned while also keeping the bandgap near optimal for a “third generation” photovoltaic exploiting carrier multiplication. For example, PbS quantum dots with a radius of 8 nm have a confined bandgap of 0.67 eV (1838 nm)(15) compared to a 0.286 eV bandgap in bulk (4335 nm).(6)

In contrast to II-VI and III-IV semiconductors, which have heavy holes, the effective mass of electrons and holes in PbS and PbSe are approximately the same near the bulk bandgap. PbS has electron and hole effective masses of $0.08 m_e$ and $0.075 m_e$, respectively, for a transverse direction and $0.105 m_e$ and $.0105 m_e$ for the longitudinal direction, where m_e is the mass of the electron in vacuum. PbSe has electron and hole effective masses of $0.040 m_e$ and $0.034 m_e$, respectively, for a transverse direction and $0.070 m_e$ and $.068 m_e$ for the longitudinal direction.(16) After photoexcitation, based on effective mass approximation, the excess kinetic energy and momentum are shared equally between electron and hole in the bulk material and were initially expected to be shared equally in PbS and PbSe quantum dots.(17, 18) More microscopic calculations have questioned this prediction,(19) which arises not only in the effective mass approximation but also in the $k \cdot p$ theory, as shown by Kang and Wise.(20) The strong confinement arising from the small effective mass in PbS and PbSe is evident in the large blue shift of the band edge in an absorption spectrum and causes the energy levels arising from

the valence and conduction bands to spread much farther apart than in quantum dots made for carriers with larger effective masses.(17) For this reason, some researchers expected a reduced phonon-carrier coupling.(17) Lead chalcogenides such as PbS and PbSe have a face-centered cubic lattice (the rock salt structure), belonging to the same symmetry class as NaCl.(16) Another interesting and unique feature of lead chalcogenide quantum dots is that the confinement at the bandgap occurs at the L-point in the first Brillouin zone,(20) unlike prototypical quantum dot semiconductors with bandgap at the Γ point (see Figure 1.2 below). Also, intervalley coupling has been predicted to occur in quantum dots, through the four degenerate valleys of the bulk semiconductor.(20)

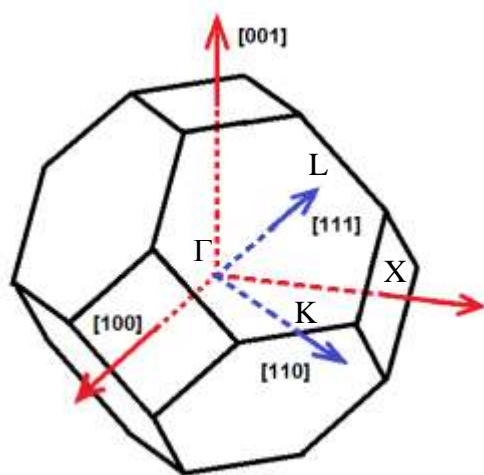


Fig 1.2. Brillouin zone of lead chalcogenides showing only a few key high points of symmetry. The axes represent the crystal momentum of the carriers along direction in the crystal with the Miller indices shown. The bandgap occurs at the L point here on the $k = [1\ 1\ 1]$ crystal axis coordinates. There appear to be eight L points, but opposite points are equivalent in the first Brillouin zone, so there are four L valleys.

1.2.2 Brief Introduction to Transient Absorption, Pump-Probe Spectroscopy

Femtosecond transient absorption spectroscopy is a type of femtosecond pump-probe spectroscopy, where the pump modulates optical transmission of the probe. The probe is time-

delayed with respect to the pump by a delay stage that changes time of arrival to the sample. See Figure 1.3.

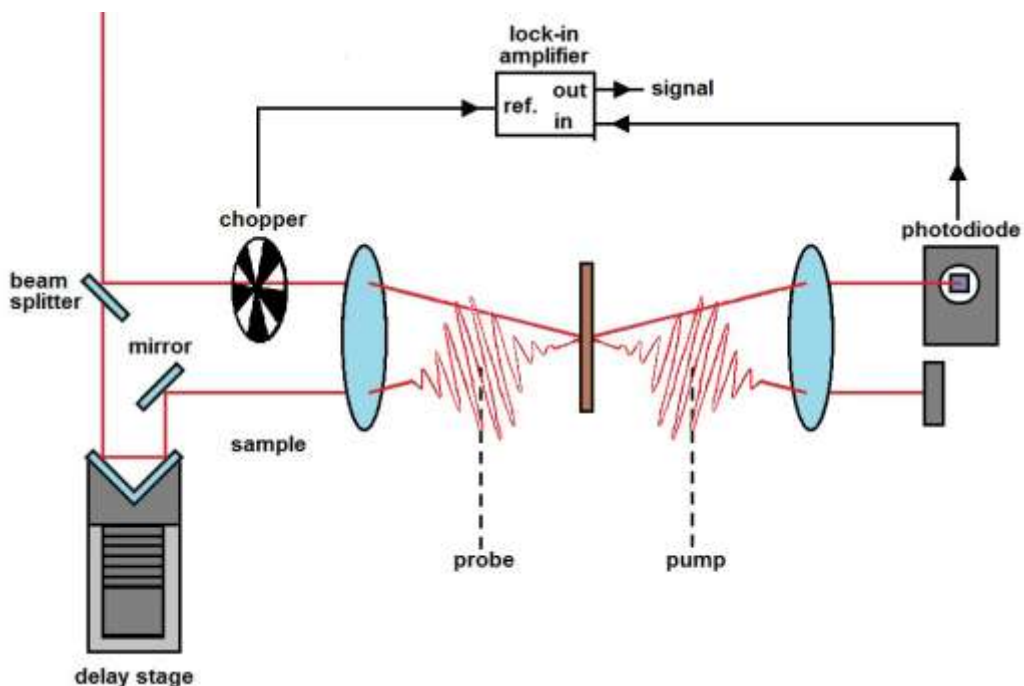


Fig. 1.3. Transient absorption experiment. The pump excites the sample, followed by a time-delayed probe pulse. By starting with coincident pump and probe pulses and sampling progressively larger time delays, the probe can measure the population in the excited state as a function of time delay. The chopper serves to create a high-frequency difference in detected probe transmission between pump on and pump off states. This difference is the pump-probe signal and can be detected with a lock-in amplifier referenced to the chopper.

In a typical transient absorption experiment, the pump excites the absorbing sample to the excited state, and change in probe-transmission is detected on a photodiode. If the signal is small, the sample is nearly transparent, there is no coherence, relaxation within each state is complete, and the signal is normalized against transmission, it measures nonequilibrium population decay as a function of time. The decay curve may look like a time-dependent single exponential decay and often reveals quantum coherences on top of this decay. I have used this technique for exploring the dynamics of photoexcitation in quantum dots.(21)

1.2.3 Early Research

Since MEG was reported to occur at three times the bandgap energy, I started research by collaborating on experiments probing hot carrier dynamics in PbS quantum dots at three times the bandgap energy.(21, 22) In addition to being a strong absorber, DQOCI is a known saturable absorber, an electronic two-level system where the ground state recovers population no faster than the excited state loses population. DQOCI has been used as a saturable absorber in mode-locked dye lasers.(23, 24) These pump-probe measurements showed a surprisingly small signal strength for quantum dots when compared with DQOCI (see Figure 1.4 below) at the same optical density.

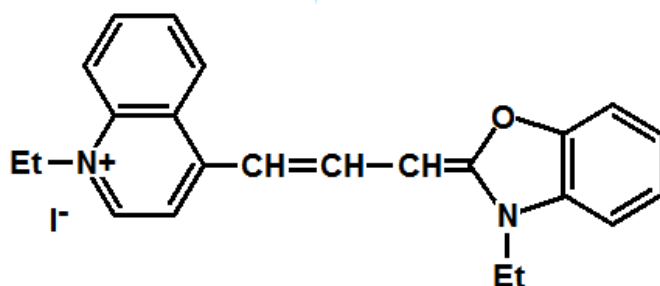


Fig. 1.4. The structure of DQOCI (C₂₃H₂₃N₂OI) is shown. The saturable absorber, DQOCI, has a peak absorption of 592 nm in ethanol.(25) The Chemical Abstract Service CAS registry number for DQOCI is 32151-96-5.

The quantum dot signal strength was 20 times weaker than that of the dye, despite the fact that the quantum dot, if acting as a single absorbing unit, was predicted to produce 30 times more signal because the molar extinction coefficient was 30 times larger.(21) Putting these together, the quantum dots had 1/600th the expected signal strength. The absence of a bleach at T = 0 for pump-probe measurements with 20 fs pulses indicated a dephasing time-scale faster than 10 fs, suggesting that one could rule out MEG theories based on longer-lived coherent oscillations between states. Many absorption spectra show that quantum-confined spectral

absorption peaks are blue-shifted by the presence of oxygen,(26-28) but sample oxygen exposure did not impact the early pump-probe decay lifetimes.

In 1983, Brus suggested that if a carrier scattered inelastically before reaching the edge of the dot, the carrier would be unable to distinguish between a nanocrystal and a bulk semiconductor(29) environment except for the collisions with the surface. Bulk semiconductors are not perfect crystals; defects and phonons that scatter carriers can destroy coherence. Consequently light is not absorbed over the whole volume of the semiconductor, but within the confines of a coherence volume. Some researchers have estimated the magnitude of the nonlinear optical response by considering the size of the absorbing unit in bulk semiconductors to be on the order of a unit cell.(30) Since an 8 nm diameter PbS quantum dot contains ~1200 unit cells, it appears that hot carriers are more like hot carriers in the bulk than band edge quantum dot excitons.

1.2.4 Absolute Signal Strength

Weaker-than-expected pump-probe signal strength at photon energies higher than three times the bandgap, wide variation in the reported MEG yields,(14) and reports about possible MEG artifacts,(10) showed where there was an increasing need for absolute pump-probe signal strength measurements with well-characterized experimental parameters like sample refresh rate, spatial beam profile, pulse energies, etc. Such measurements could act as an experimental benchmark for a systematic study of the effects of sample preparation and handling on MEG. I collaborated in using the fluorescein molecule to test experimental signal strength measurements against the absolute pump-probe signal expected from theory for a system with two electronic states. Fluorescein produces the symmetric absorption and emission spectra expected from the Frank–Condon principle for a small change in molecular geometry. Calculations of absolute

pump-probe signal strength were based on experimentally determined parameters: sample pathlength accounting for attenuation of the propagating pulses; spatial beam profile and laser pulse spectrum; the anisotropic transition probability for polarized light; and measured time-dependent electronic population relaxation (in fluorescein, this was first measured via spontaneous emission and not pump-probe). The ability to measure pump-probe signals absolutely should allow quantum dot experiments to be cross-compared among research groups. It may enable absolute determination of the MEG quantum yield, and can certainly reduce the number of assumptions involved.

1.3 SAMPLE EXCHANGE UNDER OXYGEN-FREE CONDITIONS

Investigation of colloidal quantum dots comes with a unique set of experimental challenges. Air-free sample preparation and protection of the nanocrystal surface from water and oxygen are critical. Each laser pulse, for fixed time delay, represents a repeated measurement. Exchanging the sample between laser shots ensures that the sample volume does not buildup photoproducts from prior measurements.

The first consideration comes down to understanding that surface treatments usually serve at least two functions: to create and define an energy level boundary for a confinement potential and to keep the surface free from undesirable energy levels that could act as surface traps and bonding sites. Without surface protection, nanocrystals can undergo size changes such as irreversible aggregation, whereby dots coalesce to form larger ones, and in extreme cases the solution can no longer support a colloidal suspension of the larger crystals, causing them to drop out of solution. Greasy ligands, like oleic acid or oleylamine, are a type of capping agent that is used for surface passivation and to protect against aggregation. Even still, surface ligands are insufficient and to protect the surface against oxygen or water that will compromise the

electronic structure of lead chalcogenide nanocrystals.(31) Reaction with water or oxygen replaces sulfur or selenium with oxygen, which effectively results in size reduction of the quantum dots and can be identified by a blue-shifted exciton absorption peak.(32) To avoid sample degradation, quantum dots should be synthesized in environments with oxygen and moisture levels less than 0.1 ppm. These requirements come not only from sensitivity to oxygen and water of the quantum dots, but also from the fact that many of the chemical precursors such as TOP and $(\text{TMS})_2\text{S}$ will become contaminated with unknown oxidation products leading to unknowns in the synthesis. Furthermore, some of the precursors are volatile. The second consideration involves protecting the sample over the course of the experiment by exchanging a clean sample between pulses in order to avoid buildup up of photoproducts,(33) photodegradation,(34, 35) increases in temperature,(36) or burning sample material onto the cell windows. Due to closely packed matter that affords rapid energy redistribution and better passivated surfaces, this effect is virtually nonexistent for many solid-state systems at sufficiently low intensities. In liquid samples, where interaction with the bath (solvent) takes time to redistribute energy, these effects have been appreciated for decades but were not considered properly in some studies of quantum dots. After recognizing these artifacts, a number of groups reported markedly lower MEG yields.(9, 37) Quantum dot thin films, like their colloidal counterparts, are also sensitive to oxygen, moisture, and repeated photoexcitation. Currently, there are no reports in which film samples have been exchanged between laser shots. Thus, experiments with a sample exchange are critical for elimination of repetitive photoexcitation effects.

Our group has used sealed spinning sample cells to keep samples oxygen and water free. The colloidal solution of quantum dots was trapped between two O-ring compression fittings

while a Teflon ring between windows set a calibrated optical path length of about 200 μm . This entire sample cell was screwed into a housing that was axially concentric with a set of ball bearings. The first quantum dot experiments were completed with a first generation spinner design by the JILA machine shop (see Figure 1.5 (a) below). Mechanical bearings were a dominant source of vibrational and acoustic noise. In spite of the loud noise at a few thousand RPM, this was sufficient for many colloidal quantum dot pump-probe experiments.

Two-dimensional optical spectroscopy, which will be discussed later, relies on accurate time delayed steps in an interferometer. The interferometer displacement must be known, and can be determined through active stabilization using a reference laser and an out-of-loop laser to verify stabilization and measure displacement. In a test-bed Mach–Zehnder interferometer that I actively stabilized, noises such as voices in the room could be seen on the photodiodes through the oscilloscope. As this interferometer would set critical time delay in a 2D spectrometer, acoustic and vibrational coupling to mirrors makes the spinning sample cell approach daunting. Furthermore, DC motors used to spin the cell-generated heat that could be transferred to the sample, or in prolonged usage, shut down the motor. Therefore the assembly required water cooling. Finally, for practical considerations, the assembly was inconveniently large. I eventually solved DC motor heating problems by using a DC brushless design powered and driven by radio controlled aircraft electronics. This solution has been borrowed for implementation in Ralph Jimenez’s lab.

Several iterations of spinning sample cells were constructed to reduce acoustic and vibrational effects. Common mechanical bearings appeared to be a dominant source of acoustic noise, while more precise bearings (such as Timken Fafnir Super Precision Bearings, 2MM9308WICRDUL) proved to be challenging due to “pre-load”; too much pre-load would

reduce the noise at the expense of overloading the motor. Hard disk motors, known to be acoustically quiet, contained proprietary bearings not easily sourced, and attempts to replicate the duplex bearing design using single housed versions of the same make and model bearings were unsuccessful. I tried a design in which a sample cell was positioned between three hard disk drive spindles (one master, driven by a motor, and two slaves, see Fig. 1.5 (b) and (c) below). O-ring “gears” pinned the optical cell’s grooved track in an equilateral triangle at the center. The slave drive spindle’s positions could be adjusted to pin the sample in place. After experimenting with different groove designs, offsets, and elastomer O-rings, this design turned out to be about 25 dB quieter than our other mechanical designs.(38) However, it suffered similar preload problems, and demanded far more experimental finesse to position the cell between the three points of pressure.

The second approach used a compact laptop hard disk drive assembly where the acoustically and vibrationally quiet bearings could be used directly. A new design that directly uses the glass hard disk substrates was appealing but presented a new set of challenges: bonding, solvent compatibility, filling, sealing, and keeping the cell under vacuum and moisture-free conditions. That it would refresh the sample under interferometrically stable conditions was uncertain at the time. Before uncoated hard disk substrates could be procured, I electrochemically etched the coating off hard drive disks, but unfortunately this was a low-yield process (1 in 16).

The latest design, Figure 1.5 (d) and (e) has been demonstrated to keep quantum dot samples water and oxygen free, while allowing active stabilization of interferometer displacement to within ± 1 nm (details discussed in Chapter 3). While the fluid sample cell can ensure a fresh sample for each laser shot at repetition rates over 100 kHz, its greater achievement

is demonstrated in Chapter 4, where it was used to record 2D Fourier transform spectra on PbSe quantum dots. It is believed that this device will prove useful for moving the last excited sample out of the beam between laser shots in thin film experiments, and we have provided a similar device to National Renewable Energy Laboratory (NREL) for collaboration. For pump-probe experiments, the device, with 23 cm^2 of fluid sample area, may be combined with a beam scanning technique that I helped to develop(39) to achieve refresh times on the order of 10 seconds, which should increase the number of experiments that can be conducted with sufficient sample exchange.

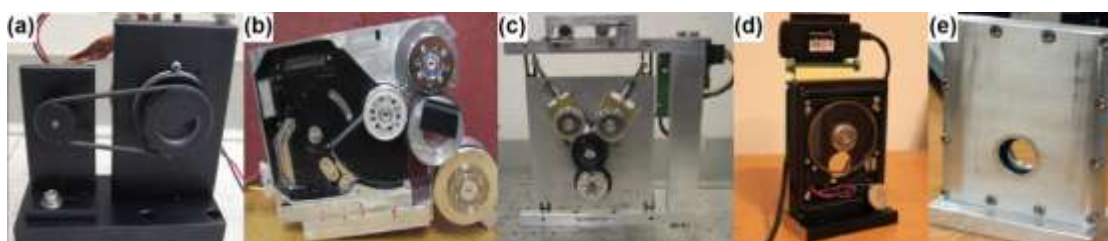


Fig. 1.5. The evolution of spinner sample cell design. On the left is the JILA spinner design (a) that uses ball bearings and a DC-bushed motor. The second design [(b) and (c)] uses hard drive bearings, a hard drive DC brushless motor, and the same sample cell holder as (a). The design was more challenging to load, but was acoustically quieter. Different in many respects, the third design [(d) and (e)] used hard drive bearings, and a sealed fluid cell made using hard disk substrates, a hard drive DC brushless motor, a smaller power supply, and a chamber to hermetically seal the environment surrounding the spinning fluid cell. This design enabled 2D spectroscopy and thin film pump-probe measurements (Chapter 4). The last spinning sample cell and chamber (e) was an improvement over (d) in reducing the rate of oxygen leakage into the sample chamber.

1.4 RETROREFLECTORS AND CONTRIBUTIONS TO 2D SPECTROMETER

Retroreflectors have found many precision metrology uses, from early measurements of earth-moon distances,(40) machining,(41) stabilized interferometers, (42, 43) and simple uses on bicycles, street signs, road paint, and clothing.(44, 45) The main advantage of using a retroreflector over a mirror is that it returns the light to its source without great sensitivity to alignment. While the number of retroreflector designs are many, hollow retroreflectors serve an

important role in Fourier transform spectroscopy,(46, 47) laser stabilization,(48) and other interference-based ultrafast techniques.(49) Hollow retroreflectors are preferred over other designs because they have lower masses than solid retroreflectors. For ultrafast spectroscopy, stabilization is often accomplished by 90° reflection from a single displacement stabilized mirror, but this leads to phase shifts that are readily detectable with Fourier transform spectral interferometry.(50) These phase shifts can be eliminated by mounting retroreflectors on piezoelectric transducers.(43)

I contributed to construction of a broadband stabilized 2D spectrometer by designing and fabricating small dihedral hollow “rooftop” retroreflectors (Chapter 2) designed for low mass (~3 g compared with 150 g commercial) so that a wider stabilization bandwidth could be achieved. When the retroreflector was attached to a piezoelectric transducer used to actively stabilize our Mach–Zehnder interferometer, the rms displacement could be stabilized to 0.8 nm rms.

Building a broadband Mach–Zehnder interferometer that ranges from 1100 to 1600 nm has a unique set of challenges. Dielectric beamsplitters that can separate HeNe beams at 594.1 and 632.8 nm from the femtosecond beam that ranges from 1100 to 1600 nm are too dispersive to be useful in femtosecond 2D short-wave infrared (IR) spectroscopy. The hollow roof top retroreflector design solves this problem by allowing us to stack beam paths and spatially separate the short-wave IR femtosecond probe beam path (used for 2D spectroscopy), from the 632.8 nm continuous wave laser (used for active stabilization and delay scanning) and the second 594.1 nm continuous wave laser (used for displacement and stability characterization). The silver mirrors afford a broad bandwidth with low dispersion, and the dihedral geometry preserves the short-wave IR polarization.

The feedback loop uses a ceramic piezoelectric transducer (often abbreviated PZT, for Plumbum (lead) Zirconium Titanate) to apply displacement feedback to the system. The piezoelectric transducer in the feedback loop is effectively a mass on a spring. The unipolar operated piezo electric transducer, Piezomechanik catalog #PCh150/10x10/2, has a spring constant of 1900 N/μm. The retroreflector mass attached is approximately 3.1 g (including the attachment base), yielding a resonance frequency of 124.6 kHz, compared with a 500 kHz unloaded piezo electric transducer, based on the simple harmonic oscillator:

$$f = \frac{1}{2\pi} \sqrt{\frac{k}{m}}, \quad (1)$$

where f is cyclic frequency, m is mass, and k is the spring constant. Since the mass is the limitation on feedback with this controller,(51) achieving a mass 50 times lighter than commercial affords a larger bandwidth by a factor of 7.

1.5 FIRST OXYGEN-FREE AND SAMPLE EXCHANGED 2D SPECTROSCOPY ON QUANTUM DOTS

The strength in the 2D spectroscopy technique is an ability to measure what one-dimensional nonlinear spectroscopies cannot. The information contained in a 2D spectrum reveals *inter-* and *intra-*molecular or atomic coupling on an ultrafast timescale. For example, electronic, vibrational, and rotational coupling strengths can be resolved, and homogeneous broadening effects can be separated from inhomogeneous broadening effects, separating the spectra of molecular systems in instantaneously different environments. The problem is that if the 2D technique is incorrectly implemented, artifacts can easily be mistaken for features, and these features will be mistaken for physics. A discussion of the basic technique follows to provide background for Chapter 4.

Two-dimensional optical spectroscopy makes use of the nonlinear interaction of three electric fields with a sample material. The signal is generated through a four-wave mixing process by way of the sample's third order nonlinear polarization vector, which radiates a fourth electric field. The time domain response of the nonlinear polarization generally appears as:

$$\vec{P}^{(3)}(t) = \epsilon_0 \int_{-\infty}^{\infty} dt_1 \int_{-\infty}^{\infty} dt_2 \int_{-\infty}^{\infty} dt_3 R^{(3)}(t; t_1, t_2, t_3) : \vec{E}(t-t_1) \vec{E}(t-t_2) \vec{E}(t-t_3), \quad (2)$$

where $R^{(3)}(t_1, t_2, t_3)$ is the microscopic third-order polarization impulse response for the sample, a fourth rank tensor. (52) Eq. (2) is local, holding at a single point in space. In Eq. (2), \vec{E} is the total electric field coming from all incident pulses at that point in space. The nonlinear polarization is excited throughout the sample and radiates fields that emerge in several distinct directions. In the context of two-dimensional spectroscopy, the radiated field in the phase

matched direction, $k_s = -k_a + k_b + k_c$, $\vec{E}_{-a,+b,+c}^{(3)}(t; t_a, t_b, t_c)$ is:

$$\vec{E}_{-a,+b,+c}^{(3)}(t; t_a, t_b, t_c) = \epsilon_0 \int_{-\infty}^{\infty} d\tau_a \int_{-\infty}^{\infty} d\tau_b \int_{-\infty}^{\infty} d\tau_c S_{-a,+b,+c}^{(3)}(t; \tau_a, \tau_b, \tau_c) : \vec{E}_a(t-t_a-\tau_a) \vec{E}_b(t-t_b-\tau_b) \vec{E}_c(t-t_c-\tau_c). \quad (3)$$

where t_a, t_b, t_c are the experimentally controlled time delays of the incident pulses, with fields \vec{E}_a, \vec{E}_b , and \vec{E}_c distinguished by their wave vectors, k_a, k_b , and k_c respectively, and $S_{-a,+b,+c}^{(3)}$ is a macroscopic response function for the particular radiated signal detected, which includes the microscopic impulse response $R^{(3)}$, bulk phase-matching, and directional filtering effects. (53)

The total electric field in Eq. (2) is:

$$\vec{E} = \vec{E}_a + \vec{E}_b + \vec{E}_c. \quad (4)$$

If the sample is “stationary” in the sense that the signal has the same time delay relative to the sequence of three excitation pulses no matter when the pulse sequence arrives at the

sample, then the four times in Eq. (3) can be replaced by three time differences.(54)

Furthermore, with the stationary assumption, the frequencies from each electric field are summed:

$$\omega_s = -\omega_a + \omega_b + \omega_c. \quad (5)$$

This stationary assumption underlies the 3D Fourier transform relationship between the third-order nonlinear susceptibility and the third-order nonlinear impulse response. This stationary assumption is not valid for repetitive photoexcitation (laser repetition rates) lacking sufficient time between pulse sequences to allow for complete thermal equilibration with the surroundings. This is particularly worth mentioning since none of the reported 2D experiments on quantum dots(55-57) have exchanged samples between laser shots, and this has the potential to undermine experiments since “photocharging” is thought to persist for seconds in quantum dots.(58)

Pulse a , with electric field $\vec{E}_a(t-t_a)$ need not precede pulse b with field $\vec{E}_b(t-t_b)$ in time. The difference in time between the pulses constitutes a time delay, $\tau = (t_a - t_b)$, which may be either positive (a first) or negative (b first). In this experiment, both pulses a and b arrive before pulse c , $\vec{E}_c(t-t_c)$, as shown in Figure 1.6.

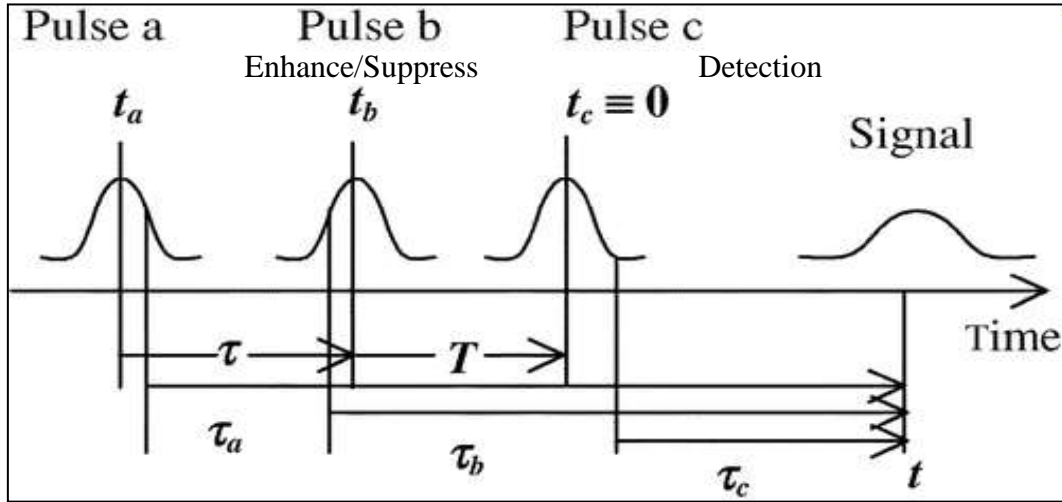


Fig. 1.6.(59) 2D Spectroscopy electric field sample interaction time sequence. $\vec{E}_a(t-t_a)$ puts the sample in a superposition of eigenstates, oscillating at their own frequencies during evolution. Field $\vec{E}_b(t-t_b)$ enhances or suppresses those oscillations. After a variable waiting period, T , field $\vec{E}_c(t-t_c)$ excites the sample to radiate a signal for detection with the reference pulse. The time delays t_a, t_b , and t_c are created through pathlength differences using retro-reflectors on a translation stage for displacement. The positive time intervals τ_a, τ_b , and τ_c represent the intervals between signal radiation and interaction with each pulse appearing in the response function, Eq (3).

The fourth signal field, generated with angular frequency ω_s , interferes with a reference field derived from an input field using a beam splitter. The signal-reference pulse pair is sent through a grating spectrometer where it is resolved into frequency components and sampled with a CCD. The interference pattern in this spectrum (or spectral interferogram) is given by:

$$I_{\text{int}}(\omega) = \left| E_s(\omega) + E_r(\omega) \right|^2. \quad (6)$$

$$= I_s(\omega) + I_r(\omega) + \sqrt{I_s(\omega)I_r(\omega)} \cos(\Delta\phi(\omega)), \quad (7)$$

where $I_s(\omega)$ is the signal spectrum, $I_r(\omega)$ is the reference spectrum, and $\Delta\phi(\omega)$ is the spectral phase difference between signal and reference. The spectral phase difference may be written as:

$$\Delta\phi(\omega) = \Delta\phi_o + \omega t_d + \frac{1}{2} \Delta\phi''|_{\omega_o} (\omega - \omega_o)^2 \quad (8)$$

where $\Delta\phi_o$ is the constant phase shift, t_d is the delay, and $\Delta\phi''$ is difference in chirp. For a pure time delay, the frequency spectrum has a cosinusoidal intensity modulation with period $\Delta\omega = \frac{2\pi}{t_d}$.

. A constant phase shift uniformly shifts the frequencies of the interference fringe maxima while changes in chirp cause a frequency dependent fringe spacing. If the reference pulse is transform limited, then $\Delta\phi(\omega)$ and $I_s(\omega)$ completely characterize the signal field, mapping out one dimension of the two-dimensional spectrum. Equally stepped time delays between pulses a and b , (i.e., τ), each with a spectrally signal-reference resolved interferogram, are fast Fourier transformed to construct the other axis of the two-dimensional spectrum. The 2D spectrum produced shows how excitation of a sample at one frequency changes the absorption of that sample across a spectrum of frequencies. One can consider sweeping a frequency ω_I along the frequency domain ω_τ axis to look at coupling between states (Figure 1.7), whose information is usually buried under the lineshape (as in one-dimensional spectroscopies like spectrally resolved pump-probe). Our lab's convention is to represent positive peaks in 2D spectra as more light on the detector, corresponding to ground state bleach (GSB) and excited state emission (ESE). Meanwhile, negative peaks in 2D spectra represent less light hitting the detector, corresponding to excited state absorption (ESA). The diagonal feature along the diagonal is total line broadening, shown in Figure 1.8. Cross-diagonal features in Figure 1.8 roughly represent homogenous broadening. This will be discussed for the 3 nm quantum dot PbSe system in Chapter 4.

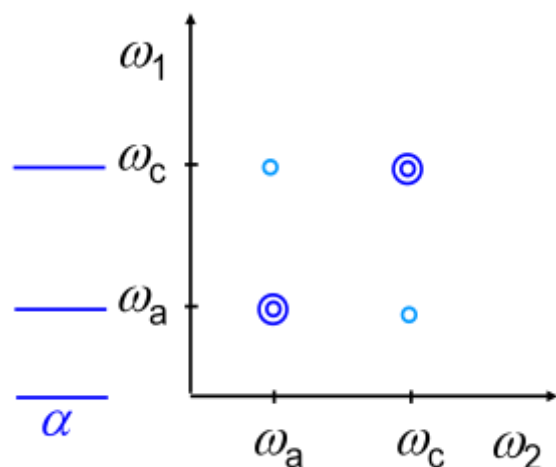


Fig 1.7. Three-level coupling. Coupling between frequencies ω_a and ω_c , shown by cross-peaks off the main diagonal. The two circles illustrate that the diagonal signal is comprised of both excited state emission and ground state bleach.(49) The y-axis may be considered excitation and the x-axis detection. Excitation of ω_a affects the absorption of ω_c through their common ground state.

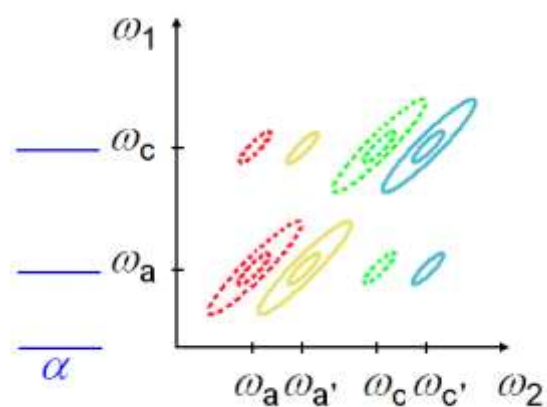


Fig. 1.8. Real part of simulated 2D Fourier transform spectrum. The dashed lines (negative) show excited state absorption, while the solid lines (positive) show ground state bleach and excited state emission.(49) The wider diagonal reflects total line broadening, both homogenous and inhomogenous, while the narrower cross diagonal represents homogenous broadening, whose lineshapes have been explored with analytic models.(60)

All third order nonlinear ultrafast spectroscopies can be cast as some limiting case of a 2D optical Fourier transform experiment by changing the geometry, timing, and number of fields

included. As a consequence, the 2D spectrum should be expected to contain all of the information and more than the dimensionally reduced experiments. For example, a limit where the first two excitation pulses are collinear, and temporally coincident, and cross the third pulse at the sample, which may be delayed with respect to the other two generates a signal field that overlaps the third pulse. If the third pulse is spectrally integrated, this is a pump-probe experiment. Another case exists when the first two fields are spatially and temporally overlapped with sufficient crossing angle to create a population grating. This grating contains excited states in constructive fringes and ground states in the destructive fringes. The third pulse c will diffract off of the grating to be collected in a CCD. Taken as a function of time delay between a/b and c , this describes the transient grating experiment.

The 2D Sagnac interferometer (Figure 1.9) used for the experiments in Chapter 4 is a non-collinear pump-probe geometry 2D combining the homotime absorption response detection (HARD) geometry(61) with the pump-probe geometry of a Sagnac.(62) The difficulty of using a pump-probe geometry in 2D is that the third order signal created from the four wave mixing of pulses a , b , and c is small compared to a the local oscillator pulse c (whose noise may be comparable with the interference). In the Sagnac, however, a reference pulse is sent through a pristine sample, and in some sense balances out against pulse c . A Sagnac can be optimized to amplify any imbalance between counter-propagating pulses. In this case, that imbalance comes from the 2D generated signal. See Ref. (63) for a more complete description. The spinning sample cell (Chapter 3), was filled with 3 nm PbSe quantum dots and was placed in the stabilized 2D spectrometer. Two-dimensional data were taken. The measurements are the first of their kind with exchanged sample, oxygen- and water-free quantum dots, and precisely locked and equally stepped 2D Fourier transform data.

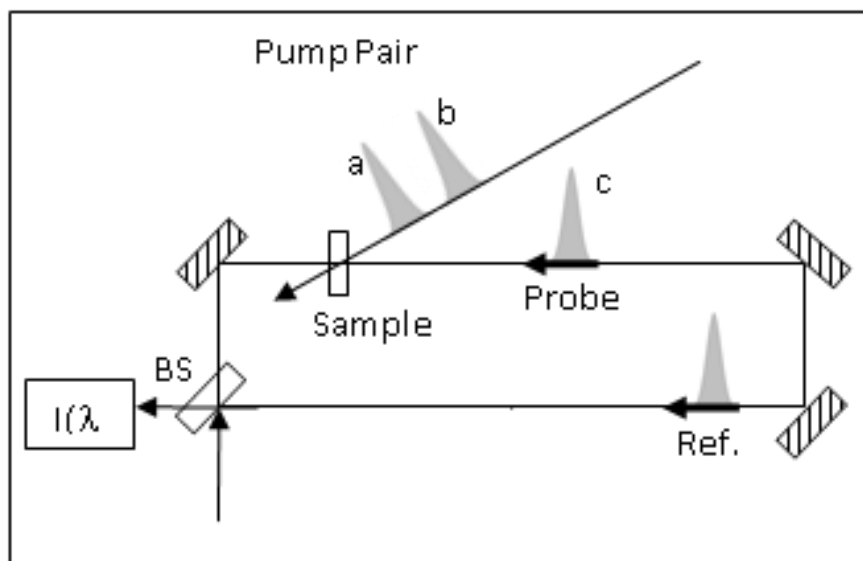


Fig. 1.9. 2D Sagnac interferometer for optimized interference detection of 2D spectra in the pump-probe geometry. The Sagnac beam splitter (BS) splits the input pulse into counter-propagating probe and reference pulses. The reference passes through the pristine sample before all other pulses. In contrast, the probe absorption will be reduced by the pump pulse pair (from a Mach-Zehnder interferometer). The spectrum of this disturbance of destructive interference between probe and reference at the “dark” output arm is detected.

1.6 ORGANIZATION OF THESIS

Chapter 2 discusses a miniature hollow rooftop retroreflector that weighs $\sim 3\text{g}$ and is ~ 50 times lighter than commercial products. It covers the technique and materials that are not covered in the optical fabrication books,(64-66) or with any level of detail in the literature.(67, 68) Testing of the surface is covered in Appendix A. This allowed us to attach it to a piezo-electric transducer and actively stabilize our 2D interferometer to $\sim 0.6\text{ nm}$.(69)

Chapter 3 of this thesis introduces a compact spinning sample cell that affords a number of important new experimental capabilities, namely: i) An ability to renew samples in an oxygen- and water-free environment; ii) Remaining interferometrically stable to $\sim 1\text{ nm}$.; and iii) a possible ability to renew sample on quantum dot thin films. The first capability, for reasons explained in Chapter 2, allows us to do actively-stabilized 2D spectroscopy on quantum dots,

while the work in Chapter 3 provides a new experimental capability to researchers working on quantum dots and quantum dot thin films.

The results of this endeavor are the subject of Chapter 4, a comparative study of the first colloidal quantum dot 2D spectra with the sample exchanged between laser shots under oxygen- and moisture-free conditions. Two-dimensional spectra are compared for static and sample-exchanged colloidal PbSe quantum dots that are measured in the short-wave IR under displacement-locked conditions. The results suggest that quantum dot 2D spectra are deleteriously affected by repetitive excitation and show the critical-need for sample exchange under excitation.

REFERENCES FOR CHAPTER 1

1. A. A. O. A.I. Ekimov, V.A. Tzehomskii, *Sov. Phys. Chem. Glass (Fiz. Khim. Stekla)* 6(511 (1980)
2. R. Rossetti, S. Nakahara and L. E. Brus, "Quantum size effects in the redox potentials, resonance Raman spectra, and electronic spectra of CdS crystallites in aqueous solution," *The Journal of Chemical Physics* 79(2), 1086-1088 (1983)
3. V. Klimov, A. Mikhallovsky, S. Xu, A. Malko, J. Hollingsworth, C. Leatherdale, H. J. Eisler and M. Bawendi, "Optical gain and stimulated emission in nanocrystal quantum dots," *SPIE milestone series* 180(366-369 (2005)
4. V. I. Klimov, A. Mikhailovski, J. A. Hollingsworth, C. A. Leatherdale and M. G. Bawendi, "Optical amplifiers and lasers," *US Patent 6819692* (2004)
5. R. D. Schaller and V. I. Klimov, "High efficiency carrier multiplication in PbSe nanocrystals: implications for solar energy conversion," *Physical review letters* 92(18), 186601 (2004)
6. Y. I. Ravich, "Lead Chalcogenides: Basic Physical Features," in *Lead Chalcogenides: Physics & Applications* D. Khokhlov, Ed., pp. 3-34, Taylor and Francis, New York (2003).
7. S. Kolodinski, J. H. Werner, T. Wittchen and H. J. Queisser, "Quantum efficiencies exceeding unity due to impact ionization in silicon solar cells," *Applied Physics Letters* 63(17), 2405-2407 (1993)
8. A. J. Nozik, "Spectroscopy and hot electron relaxation dynamics in semiconductor quantum wells and quantum dots," *Annual Review of Physical Chemistry* 52(1), 193-231 (2001)
9. M. Ben-Lulu, D. Mocatta, M. Bonn, U. Banin and S. Ruhman, "On the absence of detectable carrier multiplication in a transient absorption study of InAs/CdSe/ZnSe core/shell1/shell2 quantum dots," *Nano Letters* 8(4), 1207-1211 (2008)
10. J. A. McGuire, J. Joo, J. M. Pietryga, R. D. Schaller and V. I. Klimov, "New Aspects of Carrier Multiplication in Semiconductor Nanocrystals," *Accounts of Chemical Research* 41(12), 1810-1819 (2008)
11. J. B. Sambur, T. Novet and B. A. Parkinson, "Multiple Exciton Collection in a Sensitized Photovoltaic System," *Science* 330(6000), 63-66 (2010)
12. O. E. Semonin, J. M. Luther, S. Choi, H.-Y. Chen, J. Gao, A. J. Nozik and M. C. Beard, "Peak External Photocurrent Quantum Efficiency Exceeding 100% via MEG in a Quantum Dot Solar Cell," *Science* 334(6062), 1530-1533 (2011)

13. M. C. Beard, A. G. Midgett, M. C. Hanna, J. M. Luther, B. K. Hughes and A. J. Nozik, "Comparing Multiple Exciton Generation in Quantum Dots To Impact Ionization in Bulk Semiconductors: Implications for Enhancement of Solar Energy Conversion," *Nano Letters* 10(8), 3019-3027 (2010)
14. G. Nair, L.-Y. Chang, S. M. Geyer and M. G. Bawendi, "Perspective on the prospects of a carrier multiplication nanocrystal solar cell," *Nano letters* 11(5), 2145-2151 (2011)
15. W. K. Peters, B. Cho, R. J. Hill, T. L. Courtney and D. M. Jonas, "Band Filling Dynamics and Auger Recombination in Lead Sulfide Nanocrystals," in *Ultrafast Phenomena XVII*, Oxford University Press, New York (2010).
16. N. W. Ashcroft and N. D. Mermin, *Solid State Physics*, Saunders College, Philadelphia (1976).
17. F. W. Wise, "Lead Salt Quantum Dots: the Limit of Strong Quantum Confinement," *Accounts of Chemical Research* 33(11), 773-780 (2000)
18. K. K. Nanda, F. E. Kruis, H. Fissan and S. N. Behera, "Effective mass approximation for two extreme semiconductors: Band gap of PbS and CuBr nanoparticles," *Journal of Applied Physics* 95(9), 5035-5041 (2004)
19. A. Franceschetti, J. M. An and A. Zunger, "Impact ionization can explain carrier multiplication in PbSe quantum dots," *Nano Letters* 6(10), 2191-2195 (2006)
20. I. Kang and F. W. Wise, "Electronic structure and optical properties of PbS and PbSe quantum dots," *Journal of the Optical Society of America* 14(7), 1632-1646 (1997)
21. B. Cho, W. K. Peters, R. J. Hill, T. L. Courtney and D. M. Jonas, "Bulklike Hot Carrier Dynamics in Lead Sulfide Quantum Dots," *Nano Letters* 10(7), 2498-2505 (2010)
22. B. Cho, W. K. Peters, R. J. Hill, T. L. Courtney and D. M. Jonas, "Hot Carrier Dynamics in Lead Sulfide Nanocrystals," in *Ultrafast Phenomena XVII*, Oxford University Press, New York (2010).
23. E. Lill, S. Schneider and F. Dörr, "Passive mode-locking of a flashlamp-pumped fluorol 7GA dye laser in the green spectral region," *Optics Communications* 20(2), 223-224 (1977)
24. R. S. Adrain, E. G. Arthurs, D. J. Bradley, A. G. Roddie and J. R. Taylor, "Amplification of picosecond dye laser pulses," *Optics Communications* 12(2), 140-142 (1974)
25. U. Brackmann, *Lamdachrome Laser Dyes*, Lambda Physik, Gottingen (1986).
26. J. Tang, L. Brzozowski, D. A. R. Barkhouse, X. H. Wang, R. Debnath, R. Wolowiec, E. Palmiano, L. Levina, A. G. Pattantyus-Abraham, D. Jamakosmanovic and E. H. Sargent, "Quantum Dot Photovoltaics in the Extreme Quantum Confinement Regime: The Surface-

- Chemical Origins of Exceptional Air- and Light-Stability," *ACS Nano* 4(2), 869-878 (2010)
27. J. W. Stouwdam, J. Shan, F. van Veggel, A. G. Pattantyus-Abraham, J. F. Young and M. Raudsepp, "Photostability of colloidal PbSe and PbSe/PbS core/shell nanocrystals in solution and in the solid state," *Journal of Physical Chemistry C* 111(3), 1086-1092 (2007)
 28. Q. Dai, Y. Wang, Y. Zhang, X. Li, R. Li, B. Zou, J. Seo, Y. Wang, M. Liu and W. W. Yu, "Stability study of PbSe semiconductor nanocrystals over concentration, size, atmosphere, and light exposure," *Langmuir* 25(20), 12320-12324 (2009)
 29. L. E. Brus, "A Simple-Model for the Ionization-Potential, Electron-Affinity, and Aqueous Redox Potentials of Small Semiconductor Crystallites," *Journal of Chemical Physics* 79(11), 5566-5571 (1983)
 30. B. P. Fingerhut, M. Richter, J.-W. Luo, A. Zunger and S. Mukamel, "Dissecting biexciton wave functions of self-assembled quantum dots by double-quantum-coherence optical spectroscopy," *Physical Review B* 86(23), 235303 (2012)
 31. M. Sykora, A. Y. Kuposov, J. A. McGuire, R. K. Schulze, O. Tretiak, J. M. Pietryga and V. I. Klimov, "Effect of Air Exposure on Surface Properties, Electronic Structure, and Carrier Relaxation in PbSe Nanocrystals," *ACS Nano* 4(4), 2021-2034 (2010)
 32. I. Moreels, K. Lambert, D. De Muynck, F. Vanhaecke, D. Poelman, J. C. Martins, G. Allan and Z. Hens, "Composition and size-dependent extinction coefficient of colloidal PbSe quantum dots," *Chemistry of Materials* 19(25), 6101-6106 (2007)
 33. D. Hecht, W. Bond, R. Pantell and H. Puthoff, "Dye lasers with ultrafast transverse flow," *IEEE Journal of Quantum Electronics* 8(1), 15-19 (1972)
 34. H. Gratz, A. Penzkofer, C. Abels, R. M. Szeimies, M. Landthaler and W. Bäumlner, "Photoisomerisation, triplet formation, and photo-degradation dynamics of indocyanine green solutions," *Journal of Photochemistry and Photobiology A: Chemistry* 128(1-3), 101-109 (1999)
 35. W. Holzer, M. Mauerer, A. Penzkofer, R. M. Szeimies, C. Abels, M. Landthaler and W. Bäumlner, "Photostability and thermal stability of indocyanine green," *Journal of Photochemistry and Photobiology B: Biology* 47(2-3), 155-164 (1998)
 36. X. R. Zhu and J. M. Harris, "Studies of excited state absorption and photoisomerization of cyanine dyes by using laser induced anharmonic thermal gratings," *J. Opt. Soc. Am. B* 7(5), 796-802 (1990)
 37. A. G. Midgett, H. W. Hillhouse, B. K. Hughes, A. J. Nozik and M. C. Beard, "Flowing versus Static Conditions for Measuring Multiple Exciton Generation in PbSe Quantum Dots," *The Journal of Physical Chemistry C* 114(41), 17486-17500 (2010)

38. R. J. Hill, [3/29/2010, notebook 2, page 90] Unpublished raw data. ((2010)
39. A. P. Spencer, R. J. Hill, W. K. Peters, D. V. Baranov and D. M. Jonas, "Shot-to-shot Sample Renewal Using Beam Scanning with Applications to Pump-Probe Spectroscopy," *Review of Scientific Instruments* (To be submitted)
40. P. Bender, D. Currie, R. Dicke, D. Eckhardt, J. E. Faller, W. Kaula, J. Mulholland, H. Plotkin, S. Poultney and E. Silverberg, "The lunar laser ranging experiment," *Science* 182(4109), 229-238 (1973)
41. K. Iwasawa, A. Iwama and K. Mitsui, "Development of a measuring method for several types of programmed tool paths for NC machine tools using a laser displacement interferometer and a rotary encoder," *Precision Engineering* 28(4), 399-408 (2004)
42. T. Zhang, C. Borca, X. Li and S. Cundiff, "Optical two-dimensional Fourier transform spectroscopy with active interferometric stabilization," *Optics Express* 13(19), 7432-7441 (2005)
43. M. K. Yetzbacher, T. L. Courtney, W. K. Peters, K. A. Kitney, E. R. Smith and D. M. Jonas, "Spectral restoration for femtosecond spectral interferometry with attosecond accuracy," *JOSA B* 27(5), 1104-1117 (2010)
44. J. Luoma, J. Schumann and E. C. Traube, "Effects of retroreflector positioning on nighttime recognition of pedestrians," *Accident Analysis & Prevention* 28(3), 377-383 (1996)
45. R. D. Blomberg, A. Hale and D. F. Preusser, "Experimental evaluation of alternative conspicuity-enhancement techniques for pedestrians and bicyclists," *Journal of Safety Research* 17(1), 1-12 (1986)
46. J. Hua, P. Wang and M. Wang, "Fourier interferometry for spaceborne atmospheric sounding," *Proceedings of SPIE* 4891(169-179 (2003)
47. I. Notingher, R. E. Imhof, P. Xiao and F. C. Pascut, "Spectral Depth Profiling of Arbitrary Surfaces by Thermal Emission Decay – Fourier Transform Infrared Spectroscopy," *Applied Spectroscopy* 57(12), 1494-1501 (2003)
48. Y. Ma, H. Li, J. Lin and X. Yu, "Greatly improved stability of passively Q-switched Ce: Nd: YAG laser by using corner cube prism," *Laser Physics* 20(9), 1802-1805 (2010)
49. D. M. Jonas, "Two-dimensional femtosecond spectroscopy," *Annual Review of Physical Chemistry* 54(1), 425-463 (2003)
50. C. Dorrer, N. Belabas, J.-P. Likforman and M. Joffre, "Spectral resolution and sampling issues in Fourier-transform spectral interferometry," *J. Opt. Soc. Am. B* 17(10), 1795-1802 (2000)

51. T. Briles, D. Yost, A. Cingöz, J. Ye and T. Schibli, "Simple piezoelectric-actuated mirror with 180 kHz servo bandwidth," *Optics Express* 18(10), 9739-9746 (2010)
52. G. He and S. H. Liu, *Physics of Nonlinear Optics*, World Scientific Publishing Company Incorporated (1999).
53. N. Belabas and D. M. Jonas, "Three-dimensional view of signal propagation in femtosecond four-wave mixing with application to the boxcars geometry," *J. Opt. Soc. Am. B* 22(3), 655-674 (2005)
54. P. N. Butcher and D. Cotter, *The Elements of Nonlinear Optics*, Cambridge University Press, New York (1991).
55. J. Bylsma, P. Dey, J. Paul, S. Hoogland, E. H. Sargent, J. M. Luther, M. C. Beard and D. Karaiskaj, "Quantum beats due to excitonic ground-state splitting in colloidal quantum dots," *Physical Review B* 86(12), 125322 (2012)
56. E. Harel, S. M. Rupich, R. D. Schaller, D. V. Talapin and G. S. Engel, "Measurement of electronic splitting in PbS quantum dots by two-dimensional nonlinear spectroscopy," *Physical Review B* 86(7), 075412 (2012)
57. L. A. Yurs, S. B. Block, A. V. Pakoulev, R. S. Selinsky, S. Jin and J. Wright, "Multiresonant Coherent Multidimensional Electronic Spectroscopy of Colloidal PbSe Quantum Dots," *Journal of Physical Chemistry C* 115(46), 22833-22844 (2011)
58. J. J. Peterson and T. D. Krauss, "Fluorescence Spectroscopy of Single Lead Sulfide Quantum Dots," *Nano Letters* 6(3), 510-514 (2006)
59. J. D. Hybl, A. W. Albrecht, S. M. Gallagher Faeder and D. M. Jonas, "Two-Dimensional Electronic Spectroscopy," *Chemical Physics Letters* 297(307-313) (1998)
60. M. E. Siemens, G. Moody, H. Li, A. D. Bristow and S. T. Cundiff, "Resonance lineshapes in two-dimensional Fourier transform spectroscopy," *Optics Express* 18(17), 17699-17708 (2010)
61. S. M. Gallagher Faeder and D. M. Jonas, "Two-Dimensional Electronic Correlation and Relaxation Spectra: Theory and Model Calculations," *Journal of Physical Chemistry A* 103(49), 10489-10505 (1999)
62. K. Misawa and T. Kobayashi, "Femtosecond Sagnac interferometer for phase spectroscopy," *Optics Letters* 20(1550-1552) (1995)
63. T. L. Courtney, "Bringing Two-Dimensional Fourier Transform Electronic Spectroscopy into the Short-Wave Infrared," Ph.D. Thesis, p. 206, University of Colorado, Boulder, Colorado (2012).

64. A. S. De Vany, "Master optical techniques," *Wiley Series in Pure and Applied Optics*, New York: Wiley, 1981 1((1981)
65. P. R. Yoder, "Mounting optics in optical instruments," SPIE-International Society for Optical Engineering (2008).
66. H. H. Karow, *Fabrication Methods for Precision Optics*, Wiley, New York (1993).
67. P. Yoder Jr, "High Precision 10-cm Aperture Penta and Roof-Penta Mirror Assemblies," *Applied Optics* 10(10), 2231-2234 (1971)
68. M. S. Lipkins, "Hollow retroreflector mount," *US Patent 3,977,765* (1976)
69. T. L. Courtney, S. D. Park, R. J. Hill and D. M. Jonas, "Enhanced Interferometric Detection in 2D Spectroscopy with a Sagnac Interferometer," *Optics Letters* (to be submitted)

CHAPTER 2: LIGHTWEIGHT HOLLOW ROOFTOP MIRRORS FOR STABILIZED INTERFEROMETRY

2.1 INTRODUCTION

Retroreflectors have found many precision metrology uses, from measurements of distances(1) and machining(2) to stabilized interferometers.(3, 4) The main advantage of using a retroreflector over a mirror is that it returns the light to its source without great sensitivity to alignment.(5) While there are many retroreflector designs, hollow retroreflectors serve an important role in Fourier transform spectroscopy,(6) laser stabilization,(7) and interference-based ultrafast techniques.(3, 4) Hollow retroreflectors are preferred over other designs because they have lower masses than solid retroreflectors. They also minimize the chromatic dispersion that lengthens ultrafast pulses. For ultrafast spectroscopy, stabilization is often accomplished by 90° reflection from a single displacement stabilized mirror, but this leads to phase shifts that are readily detectable with Fourier transform spectral interferometry.(8) These phase shifts can be eliminated by mounting retroreflectors on piezoelectric transducers.(4)

Hollow rooftop mirrors have advantages because they allow beams to be stacked and because they preserve polarization (unlike trihedral retroreflectors). For a 90° angle between plane mirror surfaces, hollow rooftop mirrors have retroreflecting properties for light incident in planes perpendicular to the mirror joint (dihedral retroreflection). The drawbacks to hollow rooftop mirrors are that dihedral retroreflection is sensitive to the inclination angle of the incident beam to the mirror joint,(6) that the polarization and stacking advantages are sensitive to rotation of the rooftop mirror in the plane of the aperture, and that preservation of *s* or *p* polarization is sensitive to the inclination angle.

A reflector's mass limits the achievable bandwidth governing displacement-stability in interferometers,(9) providing motivation to reduce retroreflector mass in order to achieve greater displacement-stability. The primary difficulty in constructing hollow rooftop(10) and trihedral(11) retroreflectors can be traced to the mechanical design joining the mirrors. This challenge becomes amplified when scaling down to smaller and lighter retroreflectors that can have reduced contact area between mirrors, in contrast to difficulties encountered when scaling up the size of prisms.(12) References that discuss solid prism fabrication(13) mention solid retroreflectors as master cubes for hollow retroreflectors, but a detailed description of hollow trihedral (corner cube) retroreflector fabrication(11, 14) is rare; in particular, critical bonding materials are usually omitted as proprietary.(10, 15-17) One route involves assembly of coated mirrors in a permanent support structure followed by measurement and adjustment while bonding and curing;(16, 17) the other involves assembly and direct bonding of uncoated mirrors on a master prism, followed by coating.(10, 11) The method presented here bonds coated mirrors directly while measuring and adjusting the dihedral angle, allowing fabrication of hollow rooftop mirrors that are lighter and have a greater surface area to mass ratio than those commercially available.(17)

2.2 EXPERIMENTAL

Two hollow rooftop mirrors (HRMs) were each constructed from a rectangular enhanced silver broadband visible and infrared metal and dielectric mirror with a $\lambda/10$ front surface (JML MPS 14407309), mirror dimensions of 17.8 mm \times 13.8 mm, and a 3.2 mm substrate thickness. The mirror was cut into two pieces with a low speed diamond wheel saw (South Bay Technology® Model 650, typically used for cutting semi-conductor wafers), using a 3"

diameter, 0.006" thick blade. Letting a represent the thickness of the glass substrate, the total length (17.8 mm here) is cut into two pieces with lengths L and $L+a$, making $L = 7.3$ mm. This gives each hollow rooftop mirror a total projected area of $10.3 \text{ mm} \times 13.8 \text{ mm}$.

A jig was constructed by bolting two kinematic mirror mounts (New Focus, 9809 Classic Corner Mirror Mounts) to the plane of a free standing aluminum block wall. The mirror mounts formed a 90° 'V' angle with each mirror at 45° angle with respect to the base of the block wall (see Appendix A, Figure A.3). The two mirror halves were placed in the 'V' groove with their mirrored-surface facing up, as shown in Figure 2.1.

A Fizeau interferometer, (Zygo, GPI-XP) characterizes the two dimensional phase profile by sending out a 632.8 nm Helium Neon laser plane wave to reflect off the hollow rooftop mirrors and interfere with a reference plane wave. With respect to a reference, bright fringes represent phase differences of $2n\pi$ (integers n), while alternating dark fringes represent phase differences $(2n+1)\pi$. Counting fringes across a retroreflector determines the phase profile across that surface. For a retroreflector, the phase difference between two points measured with a Fizeau interferometer is exactly twice the optical pathlength difference (in 632.8 nm waves) between those points.

To achieve the final result, mirror angles were aligned in the jig three times while monitoring the interference fringes. The first alignment sets the jig up correctly with the mirrors simply resting on it; this alignment step is necessary because the mirror of length $L+a$ makes contact with both mirror mounts of the jig (see Figure 2.1). A single fringe across the entire surface rendered the two mirrors *nearly* indistinguishable from a flat mirror and was indicative of an ideal 90° angle whose continuity was broken by a thin line where the two halves were joined (see Appendix A, Figure A.6, marker 3). To set the approximate bonding angle and position, the

mirror of length $L+a$ was then affixed to one mirror mount with a layer of molten optical wax less than 0.25 mm thick. The shorter mirror was then slid into position using the mirror mount as a guide ramp until the side cut with the diamond saw rested on the reflective surface of the longer mirror (Figure 2.1). In preparation for bonding, a second alignment restored a single fringe across both mirrors. Then, a thin (~ 1 mm) bead of glue (Torr Seal®, Kurt J. Lesker Co.) was applied to the cut side of the shorter mirror and it was slid back into position, bonding the two mirrors. The third alignment took place immediately after this application of glue to the joint between mirrors.

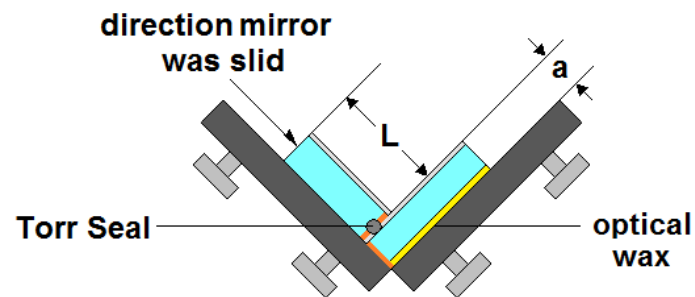


Fig. 2.1. The longer mirror was firmly affixed to the optics mount (on the right) by pressing it into a thin layer of molten optical wax (yellow). To prevent smearing Torr Seal on the longer mirror, the shorter mirror was slid in the direction of the arrow along the optic mount into its bonding position to form a 90° contact-angle with the longer mirror; the mirror edges cut with the diamond saw are shown in orange.

While the glue cured during the first two hours, small and incremental adjustments were made to the dihedral angle. As the glue dried completely, smaller drifts, typically much less than $\lambda/20$ occurred over the following ~24 hrs. Heating the underside of the optical mount allowed removal of the hollow rooftop mirror from the wax without softening the glue at the hollow rooftop mirror joint.

Using Torr Seal® as the glue was crucial. A number of bonding agents were attempted without success, including two part epoxy (Hardman Double/Bubble Extra Fast Setting Epoxy), UV curable epoxy adhesive (Epo-Tek OG116), two component thermally cured epoxy (Epo-Tek 353ND), cyanoacrylate (Duro Super Glue), and white glue (Elmer's Glue-All). The common problem was that large changes in the angle between mirrors occurred while curing. Two glues and a tongue and groove assembly for minimizing such changes have been discussed.(11) Exploration of the variety of specialized bonding cements and additives was inhibited by costs in the hundreds of dollars for a few ounces. Torr Seal®, on the other hand, has long been used for bonding windows(18) and end mirrors in stabilized laser cavities, suggesting a mechanically stable bond compatible with an actively stabilized interferometer element.

To reduce bending modes in the hollow rooftop mirror during active interferometer stabilization with the piezoelectric transducer, side supports were added. These reinforcements were constructed of glass microscope cover slips (VWR Micro Cover Glasses, #48366-205, 18 mm x 18 mm x 0.18 mm) cut into a shape resembling a Superman® shield (see Figure 2.2) and attached with Torr Seal®. After pressing the support into place, the hollow rooftop mirror was positioned so that the support was on top of the hollow rooftop mirror as the glue cured (Figure 2.2). The glue for the first support was allowed to cure for 24 hrs before the second was attached in the same manner and allowed to cure for 24 hours.

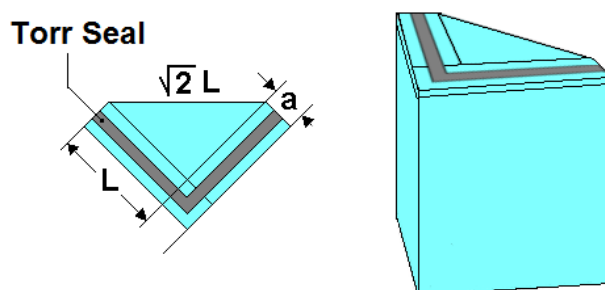


Fig. 2.2. (Left) The side supports were attached with a thin (~ 1 mm) bead of Torr Seal®. (Right) After the side support was pressed firmly into place, the assembly was set with the new side support facing up so as to dry under uniform, minimal pressure from its own weight.

Finally, the hollow rooftop mirror was glued into a 'V' groove in a 1/2" diameter cylindrical aluminum base with a flat back surface (for attachment to the piezo-electric transducer). The flat back surface of the base was mounted to the jig with double-sided tape so that one face of the base's 'V' groove would remain horizontal while the other remained vertical, see Figure 2.3. A thin piece of paper set an air gap between the vertical side of the 'V' groove and the smaller mirror. The largest mirror was pressed into Torr Seal® on the horizontal surface of the 'V' groove so that only gravity applied pressure across the resting surface while it cured. When bonding the hollow rooftop mirror to the aluminum base, the vertical air gap was necessary in order to prevent mechanical interference from misaligning the precision of the bond angle as the Torr Seal® cured. While cutting the aluminum base at the reflective point of symmetry could reduce the mass further, this was not done to minimize undue torques on the piezoelectric transducer. After the Torr Seal had cured for 24 hrs, the hollow rooftop mirrors were placed inside the Fizeau interferometer for final analysis.

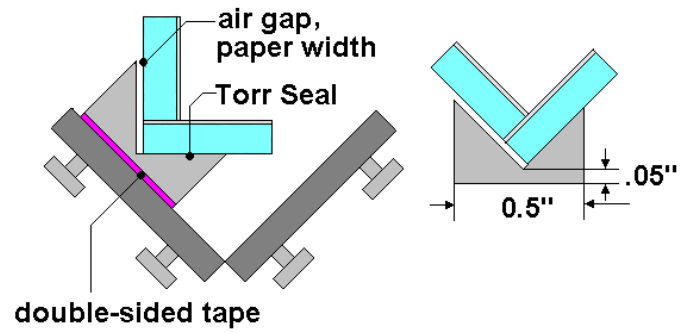


Fig. 2.3. Mounting the hollow rooftop mirror in the aluminum base. The hollow rooftop mirror was positioned in the base so that gravity exerted uniform pressure on the bond while it dried.

2.3 RESULTS

Like an ideal plane mirror, an ideal hollow rooftop with a 90° mirror joining angle returns a wavefront with a flat phase, so the quality of the hollow rooftop mirror can be measured with the same surface figures using the Fizeau interferometer. The first standard surface figure is the peak-to-valley wavefront distortion, which measures the maximum retroreflected wavefront difference with respect a planar surface in units of the measuring wavelength. The second standard surface figure is the rms wavefront distortion, which measures the root mean square deviation (in waves) of the retroreflected wavefront from a linear fit (the linear fit will remove any retroreflected beam deviation). The first hollow rooftop retroreflector (mass 3.4 g) had retroreflected wavefront distortions of ~ 0.07 waves rms and 0.24 waves peak-to-valley over 90% of its 9.5 mm x 13.8 mm aperture. The second hollow rooftop mirror (mass 3.2 g) had ~ 0.03 waves rms and 0.17 waves peak-to-valley wavefront distortions over 90% of a 9 mm x 13.8 mm aperture.

Independent of the angle of incidence within planes perpendicular to the mirror joint, a retroreflector mirror joining angle of $(\pi/2) + \alpha$ will return the incident beam at $\pi + 2\alpha$, so that the retroreflector beam deviation is 2α . The maximum ratio of wavefront difference f to lateral distance d determines the worst-case retroreflector beam deviation, $2\alpha = \arctan(f\lambda/d)$. For a simple error in joining angle, the peak to valley wavefront difference occurs over a distance of half the clear aperture.⁽⁵⁾ With $f_{p-v} = 0.17$ wave (0.24 wave) and using half the clear aperture for the distance, $d_{p-v} = 4$ mm (4.3 mm), the retroreflected beam deviation is 5 seconds of arc (7 arc seconds). For the two hollow rooftop mirrors, the actual peak-to-valley distance is in one case greater than (and in the other case equal to) half the clear aperture, so these estimates of retroreflected beam deviation are conservative.

These low mass hollow rooftop mirrors were used in both arms of a small Mach-Zehnder interferometer mounted on a breadboard on top of a vibration isolated table; the interferometer was open to air. The beams enter the hollow rooftop mirrors on one side and leave on the other,(6) enclosing an area of about 10 cm^2 . A piezo-electric transducer was attached to the back of one hollow rooftop mirror to actively stabilize the interferometer displacement using feedback from a polarized continuous wave 632.8 nm wavelength HeNe laser.(4, 19) Interferometer displacement was independently monitored outside of the feedback loop using a polarized continuous wave 594.1 nm wavelength HeNe laser.(4) The yellow and red beams were co-propagating; the hollow rooftop mirrors allowed femtosecond laser beams to be stacked above them inside the interferometer. A displacement stability of $\pm 0.8 \text{ nm rms}$ was measured over 0.1Hz to 10kHz, demonstrating the structural rigidity of the hollow rooftop mirror required for use in actively stabilizing an interferometer.

The retroreflected beam deviation determines the maximum lateral movement of the beam center as the retroreflector is translated. For a 25 mm translation with 6 arc sec retroreflected beam deviation, the beam would have a lateral walk off of $0.8 \text{ }\mu\text{m}$. This beam deviation has a minimal effect on use of the interferometer for Fourier transform spectroscopy. By fitting the peak of the Fourier transform (resolution ~ 0.0005 waves), a scan using steps of one red HeNe wave and a displacement range of 2047 waves measured the number of additional yellow waves per red wave in air as 1.06546 ± 0.00002 . Using a red HeNe wavenumber(20) [in dry air at local atmospheric pressure ($\sim 620 \text{ Torr}$)] of 15801.6 cm^{-1} , this leads directly to a yellow HeNe wavenumber of $16836.0 \pm 0.3 \text{ cm}^{-1}$ in dry air at local atmospheric pressure (16832.2 cm^{-1} in vacuum); this compares well to the yellow HeNe wavenumber of 18632.3 cm^{-1} in vacuum

calculated from the energy difference between the Ne $2s^2 2p^5 ({}^2P^0_{1/2}) 5s^2 [1/2]^o J=1$ and $2s^2 2p^5 ({}^2P^0_{3/2}) 3p^2 [5/2] J=2$ levels.(21, 22)

2.4 CONCLUSIONS

Two 3.3g hollow rooftop mirrors with clear apertures of 9 mm x 13.8 mm, return beam deviations of 6 arc seconds, and wavefront distortions of $\sim\lambda/20$ rms at 632 nm were fabricated and tested in actively stabilizing an interferometer. Compared to the lightest commercially available hollow roof mirrorsTM (PLX model RM-10-05, 25 mm x 63 mm clear aperture, 150 g mass), these hollow rooftop mirrors provide 8% of the surface area with only 2% of the mass. Typically, rms wavefront distortion increases with retroreflector clear aperture, while the return beam deviation decreases with retroreflector clear aperture. Compared to trihedral retroreflectors with clear apertures larger by a factor of five(11) or ten, (14) the rms wavefront distortion here is 5 or 20 times smaller, and the return beam deviation here is comparable(11) or 2 times larger.(14) For hollow penta-prisms that are a factor of 10 larger, beam deviations smaller by a factor of 6 have been reported with wavefront distortions larger by a factor of 5.(15) The beam deviation is comparable to that of commercially available trihedral retroreflectors with similar clear apertures, larger wavefront distortions, and twice the mass (PLX model OW-05-5, 5 second beam deviation, 12 mm clear aperture, 0.3 wave p-v wavefront distortion, 7 g mass).(17) We did not investigate whether a tongue and groove joint design for the bonded mirror surfaces(11) or alternative cements(11) would lead to improvements because the reported use of the tongue and groove approach yielded the same retroreflected beam deviation found here (but with greater wavefront distortion). It may be possible to hollow out the aluminum base to reduce its mass(15) without reducing torsional stability. A merit of the fabrication process is that it does not require

a master optical corner cube for reference, but can be constructed using standard optics mounts and a Fizeau interferometer.

The small size of these hollow rooftop mirrors allows a smaller and intrinsically more stable interferometer. Assuming the motions required for stabilization are the same, the factor of 50 reduction in mass compared to commercial hollow rooftop mirrors reduces the power required to stabilize the interferometer by a factor of 50. Further, a stabilized interferometer's active-feedback bandwidth is often limited by the actuator's mechanical resonant frequencies(9). Since the resonance frequency is inversely proportional to the square root of the mass, the factor of 50 mass reduction suggests a factor of seven increase in active feedback bandwidth. Together, these gains have enabled active stabilization of a Mach-Zehnder interferometer so that the displacement was maintained to within ± 0.8 nm.

REFERENCES FOR CHAPTER 2

1. P. Bender, D. Currie, R. Dicke, D. Eckhardt, J. E. Faller, W. Kaula, J. Mulholland, H. Plotkin, S. Poultney and E. Silverberg, "The lunar laser ranging experiment," *Science* 182(4109), 229-238 (1973)
2. K. Iwasawa, A. Iwama and K. Mitsui, "Development of a measuring method for several types of programmed tool paths for NC machine tools using a laser displacement interferometer and a rotary encoder," *Precision Engineering* 28(4), 399-408 (2004)
3. T. Zhang, C. Borca, X. Li and S. Cundiff, "Optical two-dimensional Fourier transform spectroscopy with active interferometric stabilization," *Opt. Express* 13(19), 7432-7441 (2005)
4. M. K. Yetzbacher, T. L. Courtney, W. K. Peters, K. A. Kitney, E. R. Smith and D. M. Jonas, "Spectral restoration for femtosecond spectral interferometry with attosecond accuracy," *J. Opt. Soc. Am. B* 27(5), 1104-1117 (2010)
5. Z. Bleier, I. Vishnia and J. Lipkins, "Hollow Retroreflectors Promote Precision Optical Alignment," *Photonics Spectra* 38(3), 82-91 (2004)
6. W. H. Steel, *Interferometry*, Cambridge University Press, Cambridge (1967).
7. Y. F. Ma, H. J. Li, J. P. Lin and X. Yu, "Greatly improved stability of passively Q-switched Ce:Nd:YAG laser by using corner cube prism," *Laser Phys.* 20(9), 1802-1805 (2010)
8. C. Dorrer, N. Belabas, J.-P. Likforman and M. Joffre, "Spectral resolution and sampling issues in Fourier-transform spectral interferometry," *J. Opt. Soc. Am. B* 17(10), 1795-1802 (2000)
9. T. C. Briles, D. C. Yost, A. Cingöz, J. Ye and T. R. Schibli, "Simple piezoelectric-actuated mirror with 180 kHz servo bandwidth," *Opt. Express* 18(10), 9739-9746 (2010)
10. D. T. Shen, "Frameless Hollow Roof Mirror and Method of Manufacture," *US Patent* 7,324,733 B2 (2008)
11. J. J. Lyons and P. A. Hayes, "High-optical-quality cryogenic hollow retroreflectors," *Proc. SPIE* 2540(15 September), 94-100 (1995)
12. H. S. Rana and N. B. Mullett, "Fabrication challenges in large prisms," *Proc. SPIE* 4411(5 February), 140-141 (2002)
13. A. S. De Vany, *Master Optical Techniques*, Wiley, New York (1981).
14. A. Preston and S. Merkwitz, "Hollow Retroreflectors for Lunar Laser Ranging at Goddard Space Flight Center," in *International Technical Laser Workshop 2012 (ITLW-*

- 12) M. Pearlman and S. Dell'Agnello, Eds., pp. Thursday 8 November, Session 6: Talk 2, Frascati (Rome), Italy (2012).
15. P. Yoder Jr, "High Precision 10-cm Aperture Penta and Roof-Penta Mirror Assemblies," *Applied Optics* 10(10), 2231-2234 (1971)
 16. M. S. Lipkins, "Method and Device for Assembling Hollow Retroreflectors," *US Patent 3,936,194* (1976)
 17. M. S. Lipkins, "Hollow retroreflector mount," *US Patent 3,977,765* (1976)
 18. W. E. Bell, "Vacuum sealing of gas laser windows," *US Patent 3,390,351* (1968)
 19. D. J. Jones, E. O. Potma, J. X. Cheng, B. Burfeindt, Y. Pang, J. Ye and X. S. Xie, "Synchronization of two passively mode-locked, picosecond lasers within 20 fs for coherent anti-Stokes Raman scattering microscopy," *Rev. Sci. Instrum.* 73(8), 2843-2848 (2002)
 20. W.-K. Lee, H. S. Suh and C.-S. Kang, "Vacuum wavelength calibration of frequency-stabilized He-Ne lasers used in commercial laser interferometers," *Opt. Eng.* 50(5), 054301 (2011)
 21. H. G. Heard and J. Peterson, "Super-Radiant Yellow and Orange Laser Transitions in Pure Neon," *Proc. IEEE* 52(10), 1258 (1964)
 22. "NIST Atomic Spectra Database Levels Data (Ne I)," <http://physics.nist.gov/cgi-bin/ASD/energy1.pl>

CHAPTER 3: INTERFEROMETRICALLY STABLE, HIGH-SPEED ROTATING SAMPLE CELL FOR AIR-FREE SOLUTIONS AND FILMS

3.1 INTRODUCTION

For spectroscopy on samples with long recovery times after excitation (such as molecular and nanomaterial pump-probe experiments), it is essential to refresh the sample volume between measurements to prevent buildup of photoproducts,(1) an increase in temperature,(2) photodegradation,(3, 4) or burning sample material onto the windows. Similar concerns apply to laser gain media.(5-9). For pulsed spectroscopy, the product of the beam diameter and the laser repetition rate gives the minimum velocity needed so that the next laser shot excites a fresh sample. Approaches to exchanging liquid samples between shots include flow through a cuvette,(10-15) stirring(16, 17), microfluidics,(18) nanofluidics,(19) liquid jets,(20, 21) and wire-guided flowing liquid jets.(22) Flow cells use less volume than jets, but laminar flow has zero velocity next to a window, so stirring or flowing samples inside a cell always subjects a portion of sample to repetitive excitation. Liquid jets can completely exchange a fluid sample between laser shots but require large reservoir volumes.(23, 24) Approaches applicable to liquids or solids include moving the beam with a spinning lens,(25) spinning the sample cell,(26-33) translating the sample cell,(21) or spinning and translating the sample cell.(34) Spinning lenses and spinning fluid sample cells typically use acoustically audible bearings that also couple to interferometer displacement.

A spinning fluid sample cell can completely exchange the sample between shots, requires small sample volumes, can be used for liquids and solids, and allows a number of shots up to the ratio of the annular area of the fluid sample cell to the spot size of the laser before a given sample volume is re-excited. Probed at a fixed radius, a spinning cell must probe sample volumes again

after a number of shots equal to the circumference divided by the beam diameter. Hard disk drives are acoustically and vibrationally quiet, suggesting compatibility with interferometric techniques, such as 2D optical spectroscopy, where errors in interferometer displacement due to vibration will lead to spectral artifacts when Fourier transformed.

3.2 CONSTRUCTION

The spinning disk uses parts sourced from a laptop 20 GB storage capacity hard disk drive that spins at 4200 rpm (Hitachi, Travelstar, part number 92P6327). All components but the motor were removed from the hard disk drive chassis. The longer side of the chassis, not under the hard drive disk, was cut off, leaving a nearly square portion with sides approximately equal to the width of the original chassis. Four springs used as DC brushless motor contacts were removed from the motor and four magnet wires, which have a thin insulating coating, soldered in their place. These magnet wires run behind the hard disk chassis, and were soldered to a vacuum feed-through connector. The original electronic driver board, which spins the motor, was relocated outside the sample chamber and soldered to wires connected to the sample chamber feedthrough, where it received power by connecting its IDE (Integrated Drive Electronics) pins to a computer Serial Advanced Technologies Attachment (SATA)/IDE to Universal Serial Bus (USB) 2.0 Adapter drive (Vantec, model CB-ISATAU2), utilizing a wall plug or a USB power supply. Clearance holes drilled in the hard disk drive chassis are used to bolt the size-reduced chassis into the 4.8 mm deep sample chamber cavity.

The drive motor assembly can be used with fluid sample cells or thin-film coated hard disk glass substrates. To provide an oxygen-free environment for thin films on substrates, the casing has a lid with a viewport window for hermetically sealing the rotating substrate sample

disk using 2-046 Viton O-rings for a high vacuum seal. Fused silica windows are used as viewports.

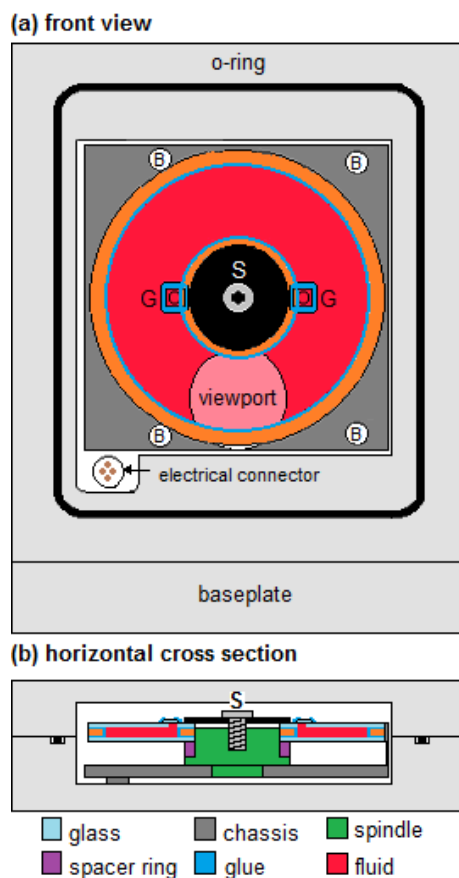


Fig. 3.1. Sample spinner assembly. The hard disk drive chassis (dark gray) has been cut down to approximately a square shape (the left hand side was cut off, removing the hard drive readout) and bolted down to the sample chamber (light gray) with bolts (B) running through the chassis into tapped holes in the sample chamber. Parts of the chassis that do not show up in the horizontal cross section establish the spacing between the chassis and the bottom of the sample chamber cavity. A 29/32 in. viewport (pink) was cut in the chassis to let the optical beams pass through the fluid sample cell (red). In the front view, the center of the viewport was roughly horizontally aligned with the spindle center (S) and vertically about 23 mm below. The fluid sample was held in place by 200 μm thick and 0.1 in. width titanium sample spacer rings (orange), which were glued between the glass substrates. The sample cell was filled through the two 1 mm diameter holes cut in the substrate glass shown at (G). A square sealing cover slip at (G) covered these holes and optical glue formed a seal around the cover slip. The entire fluid sample cell was slipped over the spindle (green) on top of a 2.28 mm thick hard drive spacer ring (purple), of ID 20 mm and OD 23.65 mm, which is part of the original hard disk drive assembly and was found to be the same dimension for several different hard drives. The fluid sample cell is bolted in place with a spindle retaining plate (S), shown in black. Taking power from a wall plug, SATA/IDE power supply was connected to the hard disk drive circuit board. Four wires were soldered to the board and to the exterior of the electrical feed-through. The inner electrical feed through was soldered to four magnet wires that ran in the space behind the hard disk chassis, where they were soldered to the four DC brushless motor connections. The entire enclosure is 117 mm tall \times 101.8 mm wide \times 19.7 mm thick, not including the base plate.

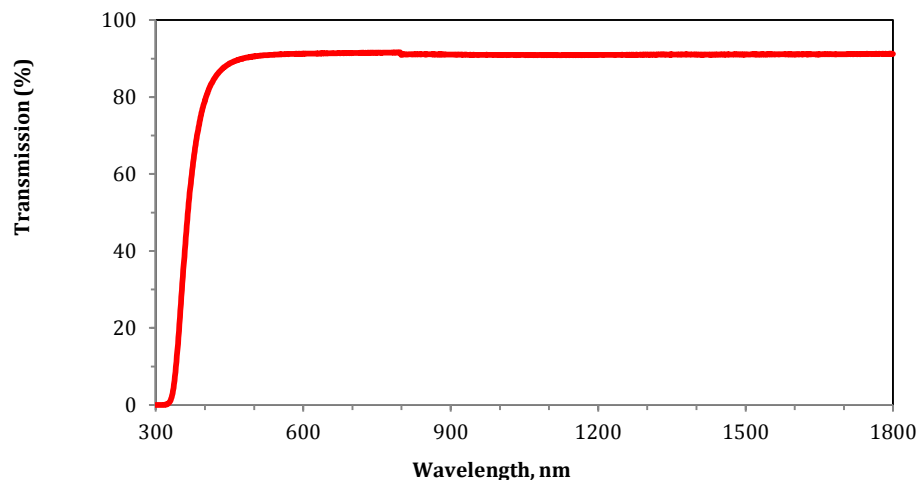


Fig. 3.2. Hard disk glass substrate transmission spectra. Spectra were sampled with a Cary 500 UV-VIS-IR spectrophotometer from 300–1800 nm. The slight discontinuity near 800 nm is the detection optics changeover point from visible to IR.

Hard disk technology requires a high degree of surface flatness⁽³⁵⁾ and a tight fit. A substrate can be directly coated for thin film studies. Proprietary-blend substrate glass with the transmission spectrum shown in Figure 3.2 was obtained from Konica Minolta (0.632 mm \pm 0.003 mm thickness, 64.979 \pm 0.003 mm outer diameter, 19.998 \pm 0.025 mm inner diameter, measured with micrometers and calipers, respectively). The surface flatness measured with a Fizeau interferometer (Zygo, GPI-GXP model) showed the largest gradient in the radial direction, with 2.5 μ m height change over 22 mm. Fluid samples used two substrates for each cell. Titanium spacer rings, 200 μ m high and \sim 0.1 in. annular radial width, set the optical path length. The inner ring's inner diameter matches (or is slightly larger than) that of the glass substrate. The outer ring has an exterior diameter that matches the glass substrate.

The titanium rings were glued to the glass substrate sequentially, starting from the inner ring. This assembly process worked best with two people and began with bonding titanium rings as inner and outer path-length spacers for the optical cell. First, the rings were fixed to an aluminum base with double-sided tape (Scotch®) in order to prevent bowing. Then, a small

amount of UV curable adhesive, Loctite® 352, was spread on the inner ring, and the glass substrate was lowered onto it with an aluminum slug (20 mm diameter) in the center, ensuring the concentric position of the glass with respect to the ring (Appendix B, Figure B.3). With the glass aligned and the slug removed, one person applied pressure to the substrate with four contact points, while the other cured the glue with a UV light. (It was difficult for one person to both hold the substrate down and use the curing lamp without the substrate slipping, hence the two-person assembly.) Next, the glass with the attached ring was taken off the aluminum base and visually inspected to ensure that no air bubble tracks had formed in the bond between the ring and the substrate. Initial misalignment may leave a small track of glue on the interior glass; this glue residue may be cleaned up after the UV cure. The curing process described for the inner ring was repeated for the outer ring. The bond cured in less than 5 min. After both rings had been attached, the cell was removed from the aluminum base, flipped over, and inspected for optical cleanliness. Any extra strands of glue may be cleaned off with acetone or methanol. With the inner surface of the cell clean, the base substrate with titanium rings facing up was lowered and fixed back onto the aluminum base with double-sided tape. A thin layer of glue was applied to the top of the titanium rings for bonding the top glass substrate. A thin ring of glue was applied with a 21-gauge hypodermic needle on the interior side of both titanium rings.

The top glass substrate had two diametrically opposite 1 mm diameter holes drilled 3.9 mm from the inner diameter with a diamond bit. The top substrate was lowered into place using a hard disk drive spindle to mechanically guide the alignment; the spindle was removed before the UV curing procedure. Hand pressure was applied to the top substrate while sequentially curing the glue (Appendix B, Figure B.5), sealing first the inner ring and then the outer ring. For a final cure of the glue, the cell was baked in an oven at 120 °C for 30 min. The

total thickness of the fluid sample cell was measured at the inner diameter as 1.52 mm and at the outer diameter as 1.47 mm, with no significant angular variation in either thickness (less than ± 0.01 mm). This radial thickness variation is likely caused by different glue thicknesses sealing the inner and outer spacers, which implies that optical path lengths vary between 197 and 246 μm across the accessible radii of the sample; this is consistent with measurements of the optical density of the sample as a function of radius. The fluid sample cell was placed in an argon-filled glovebox (MBRAUN UNIlab, 2.1 mbar of positive argon pressure, UHP grade argon, AirGas) with sub-0.1 ppm levels of O_2 and H_2O . The fluid sample cell was filled through the 1 mm fluid sample cell holes (marked as [G] in Figure 3.1) using a syringe. A microscope cover slip, cut small enough to just cover the holes, was wiped with light-curable adhesive (Loctite®, 352) and then pressed against the fluid sample cell. A small bead of the light-curable adhesive was placed around the slide to ensure against any possible leaks between the cover slip and the fluid sample cell. A pre-fashioned mask was placed over the cell so as to minimize UV exposure while curing the seal to the cover slips.

The sample cell chamber was machined of aluminum to house the hard disk drive motor and designed to keep moisture and air out of the chamber. The nearly planar symmetric clam-shell design had an O-ring grooved track for a 3/16 in. O-ring on one mating surface, and a flat mating surface on the other. Both sides were bored out to accommodate the disk drive chassis and attached fluid spinning disk. The hard disk drive chassis is bolted to the O-ring grooved side, which was in turn bolted to a 1/2 in. baseplate with two equally-spaced 1/4-20 bolts. Each half had small inset lip (~0.1 in.), to which 1 in. diameter viewport windows were internally bonded with Torr Seal. The two halves were sealed by tightening twelve equally spaced 9/64 Allen head bolts around the exterior perimeter (not shown in Figure 3.1). A hole was drilled in the lid above the

viewport and tapped with normal pipe thread (NPT). A Swagelok valve fitted to the NPT for pressure testing. The rough test involved applying 80 psi to the chamber and submerging it in water to look for small visible leaks, followed by a soapy leak-test at the aforementioned pressure. The sample cell chamber was filled with helium at a pressure of 10–20 psi. Sampling the seals, a helium leak detector (Varian Auto Test®, Model 948) found nothing above background levels at $8.5 \times 10^{-8} \text{ cm}^3/\text{s}$. The NPT Swagelok valve and the NPT port was capped off, and sealed with Teflon tape.

3.3 EXPERIMENTS AND QUANTIFICATION

Samples that can be electronically excited in the visible and short-wave infrared are usually sensitive to oxygen and water. For example, colloidal quantum dots(16, 36, 37) show a blue shift of the first exciton peak upon oxidation (due to the shrinking in size of the quantum confined crystalline core)(38). To make this sample cell suitable for air- and moisture-sensitive samples, both the fluid sample cell and the sample chamber could be independently kept air- and moisture-free for the duration of a typical spectroscopic experiment (48 h).

Tests on the fluid sample cell were performed with solution of PbSe nanocrystals in isocetane. A sample of ~2.5 nm diameter PbSe nanocrystals, sensitive to oxygen and water, was synthesized according to Refs. (39, 40); the first exciton peak is at 1122 nm. When the adhesive had completely cured, the cell was transferred into the glovebox, filled with solution of nanocrystals, sealed, and exposed to air for three days. Comparing the linear absorption spectrum to a spectrum of unexposed PbSe nanocrystals after three days, the first exciton peak shows no blue shift within the measurement uncertainty ($\pm 1 \text{ nm}$). In contrast, a sample of the same nanoparticle solution exposed to air for the same time duration shows a peak shift of ~4 nm.

A long-term air test was performed by monitoring the reaction of a solution of sodium benzophenone (NaBZ) in toluene. NaBZ is a stable diphenylketyl radical which is oxygen- and water-sensitive. NaBZ has an intense blue color,(41) which becomes colorless upon oxidation, allowing determination of the extent of the radical depletion spectrophotometrically. Before NaBZ tests, the disassembled sample cell chamber was degassed inside the antechamber using a form of flushed desorption (see Appendix B),(42) and O-rings were baked at 100°C for 9 h inside the glovebox.(43) The sample chamber was assembled with an open cuvette of NaBZ in toluene inside; it sat in the glovebox for 24 h. No change in color saturation was observed by eye over this period. Next, the sample chamber with NaBZ solution inside was exposed to air. The blue color of NaBZ is quenched upon reaction with water in 1:1 mole ratio and upon reaction with oxygen in 1:0.08 mole ratio.(44) Using $1.25 \times 10^4 \text{ M}^{-1} \cdot \text{cm}^{-1}$ for the extinction coefficient of NaBZ at 630 nm,(45) an initial optical density of the NaBZ solution of 1.546 in 1 mm pathlength at 630 nm, and a solution volume of 0.4 mL, we estimated the amount of NaBZ reacted over the course of 50 h to be ~150 nmol. Thus, if the NaBZ reacted exclusively with O₂, then it would consume ~12 nmol (~268 nL at STP conditions) of oxygen; if it reacted exclusively with H₂O, then it would consume ~150 nmol (~2.7 μL) of water.

Results of the tests with NaBZ suggest that oxygen leaks into the cell chamber at a rate dictated by permeation through the O-ring seal, as calculated based on Ref. (46), using the partial pressure of oxygen. Assuming a constant leak rate over time, and 21% oxygen content by volume, oxygen leaks into the chamber at 7.2×10^{-9} standard cm³/s. The calculated oxygen permeation rate(46) for an O-ring seal of 4.25 in. inner diameter is $(4-10) \times 10^{-9}$ standard cm³/s.

The cell was filled with a solution of IR144 dye in methanol with an optical density of 0.14 at 800 nm, and pump-probe signals were recorded by measuring the pump-induced change

in transmitted probe photon number. The pump and probe pulses were 80 fs in duration at 800 nm center wavelength. The repetition rate was 10 kHz, and the beam diameter was 50 μm . A pump-probe time delay trace was recorded by average from five sequential scans. For time delays between 220 and 480 fs, the average signal-to-noise ratio was 55 for the spinning cell vs. 41 for the static sample, which also had 10% less signal.

An accelerometer on the same optical breadboard as the spinning fluid sample cell showed that the 70 Hz rotational speed had a peak acceleration of 7×10^{-4} g at the fundamental frequency, 70 Hz, and of 3.5×10^{-4} g at the third harmonic, 210 Hz. The effect of spinning sample cell vibrations on an actively stabilized Mach–Zehnder interferometer was negligible.

Briefly, a feedback loop used an error signal derived from a 632.8 nm red laser beam to adjust a lightweight dihedral retroreflector with a piezoelectric transducer. Displacement stability was measured out of loop using a 594.1 nm yellow laser beam that propagated parallel to, but slightly above, the red beam. The intensity of the yellow interferometer output as detected on a photodiode has the form:

$$V(d) = \Delta V \cos\left(\frac{2\pi}{\lambda_y} d\right) + V_{\text{DC}}, \quad (5)$$

where V is a measured amplitude, ΔV is half the peak to peak voltage change, d is the interferometer displacement, $\lambda_y = 594$ nm is the yellow HeNe wavelength, and V_{DC} is an offset.

For small fluctuations in displacement, the rms displacement and voltage are related by

$\delta d = \delta V / (\partial V / \partial d)$, where $\partial V / \partial d$ is evaluated at the locked displacement, d_0 . Stability was

measured for a locked displacement with $V(d_0) \approx V_{\text{DC}}$, where sensitivity to displacement

fluctuations (δd) is greatest. The rms displacement fluctuation was found to be $\delta d = \pm 1$ nm for

the sample cell both when stationary and when spinning at 4200 rpm.

3.4 CONCLUSIONS

The spinning sample cell described here is compatible with interferometry and with air- and moisture-sensitive samples. Drawbacks of the current design include single use of the fluid sample cell, a radial variation in sample path length, and a leak rate of 7×10^{-9} standard cm^3/s . Uniform pressure and simultaneous curing of both seals might generate a more uniform pathlength. Since the leak rate is commensurate with oxygen permeation of the high vacuum O-ring seal, UHV seals and procedures (47) could reduce it by three orders of magnitude. Demonstrated advantages of the spinning sample cell include small liquid sample volumes (~ 0.5 ml), low vibration, and sample velocities of 140 cm/s for thin films and 120 cm/s for liquids.

REFERENCES FOR CHAPTER 3

1. T. Yoshizawa and G. Wald, "Pre-Lumirhodopsin and the Bleaching of Visual Pigments," *Nature* 197(4874), 1279-1286 (1963)
2. X. R. Zhu and J. M. Harris, "Studies of excited state absorption and photoisomerization of cyanine dyes by using laser induced anharmonic thermal gratings," *J. Opt. Soc. Am. B* 7(5), 796-802 (1990)
3. H. Gratz, A. Penzkofer, C. Abels, R. M. Szeimies, M. Landthaler and W. Bäumlner, "Photoisomerisation, triplet formation, and photo-degradation dynamics of indocyanine green solutions," *Journal of Photochemistry and Photobiology A: Chemistry* 128(1-3), 101-109 (1999)
4. W. Holzer, M. Mauerer, A. Penzkofer, R. M. Szeimies, C. Abels, M. Landthaler and W. Bäumlner, "Photostability and thermal stability of indocyanine green," *Journal of Photochemistry and Photobiology B: Biology* 47(2-3), 155-164 (1998)
5. D. Hecht, W. Bond, R. Pantell and H. Puthoff, "Dye lasers with ultrafast transverse flow," *IEEE Journal of Quantum Electronics* 8(1), 15-19 (1972)
6. S. Basu, "Nd-YAG and Yb-YAG rotary disk lasers," *IEEE Journal of Selected Topics in Quantum Electronics* 11(3), 626-630 (2005)
7. R. L. Byer, "High power solid state laser," *US Patent 4555786* (1985)
8. S. Basu, T. Kane and R. Byer, "A proposed 1 kW average power moving slab Nd:Glass laser," *IEEE Journal of Quantum Electronics* 22(10), 2052-2057 (1986)
9. S. Basu and R. L. Byer, "Average power limits of diode-laser-pumped solid state lasers," *Applied Optics* 29(12), 1765-1771 (1990)
10. V. De Waele, M. Beutter, U. Schmidhammer, E. Riedle and J. Daub, "Switching dynamics of the photochromic 1,1-dicyano-2-(4-cyanophenyl)-1,8a-dihydroazulene probed by sub-30 fs spectroscopy," *Chemical Physics Letters* 390(4-6), 328-334 (2004)
11. B. N. Toleutaev, T. Tahara and H. Hamaguchi, "Broadband (1000 cm⁻¹) multiplex CARS spectroscopy: Application to polarization sensitive and time-resolved measurements," *Applied Physics B* 59(4), 369-375 (1994)
12. Y. Su and G. N. R. Tripathi, "Time-Resolved Resonance Raman Observation of Protein-Free Riboflavin Semiquinone Radicals " *Journal of the American Chemical Society* 116(10), 4405-4407 (1994)
13. D. M. Jonas, M. J. Lang, Y. Nagasawa, T. Joo and G. R. Fleming, "Pump-probe polarization anisotropy study of femtosecond energy transfer within the photosynthetic

- reaction center of *Rhodobacter sphaeroides* R26," *Journal of Physical Chemistry* 100(30), 12660-12673 (1996)
14. J. Bredenbeck and P. Hamm, "Versatile small volume closed-cycle flow cell system for transient spectroscopy at high repetition rates," *Review of Scientific Instruments* 74(6), 3188-3189 (2003)
 15. M. Boiteux and O. de Witte, "A Transverse Flow Repetitive Dye Laser," *Applied Optics* 9(2), 514-515 (1970)
 16. J. A. McGuire, J. Joo, J. M. Pietryga, R. D. Schaller and V. I. Klimov, "New Aspects of Carrier Multiplication in Semiconductor Nanocrystals," *Accounts of Chemical Research* 41(12), 1810-1819 (2008)
 17. G. Nair, S. M. Geyer, L.-Y. Chang and M. G. Bawendi, "Carrier multiplication yields in PbS and PbSe nanocrystals measured by transient photoluminescence," *Physical Review B* 78(12), 125325 (2008)
 18. J. L. Lubbeck, K. M. Dean, H. Ma, A. E. Palmer and R. Jimenez, "Microfluidic Flow Cytometer for Quantifying Photobleaching of Fluorescent Proteins in Cells," *Analytical Chemistry* 84(9), 3929-3937 (2012)
 19. D. Kraemer, M. L. Cowan, A. Paarmann, N. Huse, E. T. J. Nibbering, T. Elsaesser and R. J. D. Miller, "Temperature dependence of the two-dimensional infrared spectrum of liquid H₂O," *Proceedings of the National Academy of Sciences of the United States of America* 105(2), 437-442 (2008)
 20. N. Pugliano, S. Gnanakaran and R. M. Hochstrasser, "The dynamics of photodissociation reactions in solution," *Journal of Photochemistry and Photobiology A: Chemistry* 102(1, Supplement 1), 21-28 (1996)
 21. J. Oberle, E. Abraham, A. Ivanov, G. Jonusauskas and C. Rulliere, "Picosecond CARS and transient absorption studies of 1,4-diphenylbutadiene and trans-stilbene: A study of photoinduced formation of a radical cation," *Journal of Physical Chemistry* 100(24), 10179-10186 (1996)
 22. M. J. Tauber, R. A. Mathies, X. Chen and S. E. Bradforth, "Flowing liquid sample jet for resonance Raman and ultrafast optical spectroscopy," *Review of Scientific Instruments* 74(11), 4958-4960 (2003)
 23. B. Wellegehausen, H. Welling and R. Beigang, "A narrowband jet stream dye laser," *Applied Physics* 3(5), 387-391 (1974)
 24. H.-P. Harri, S. Leutwyler and E. Schumacher, "Nozzle design yielding interferometrically flat fluid jets for use in single-mode dye lasers," *Review of Scientific Instruments* 53(12), 1855-1858 (1982)

25. D. Ionascu, F. Rosca, F. Gruia, A. Yu and P. M. Champion, "Optical scanning instrument for ultrafast pump-probe spectroscopy of biomolecules at cryogenic temperatures," *Review of Scientific Instruments* 77(6), 064303-064307 (2006)
26. B. A. West, J. M. Womick and A. M. Moran, "Influence of temperature on thymine-to-solvent vibrational energy transfer," *The Journal of Chemical Physics* 135(11), 114505-114509 (2011)
27. B. A. West and A. M. Moran, "Two-Dimensional Electronic Spectroscopy in the Ultraviolet Wavelength Range," *The Journal of Physical Chemistry Letters* 3(18), 2575-2581 (2012)
28. W. Kiefer and H. J. Bernstein, "A Cell for Resonance Raman Excitation with Lasers in Liquids," *Applied Spectroscopy* 25(4), 500-501 (1971)
29. U. Åberg, E. Åkesson, J. L. Alvarez, I. Fedchenia and V. Sundström, "Femtosecond spectral evolution monitoring the bond-twisting event in barrierless isomerization in solution," *Chemical Physics* 183(2-3), 269-288 (1994)
30. M. Lim, T. A. Jackson and P. A. Anfinrud, "Nonexponential protein relaxation: dynamics of conformational change in myoglobin," *Proceedings of the National Academy of Sciences of the United States of America* 90(12), 5801-5804 (1993)
31. F. Rosca, A. T. N. Kumar, D. Ionascu, T. Sjodin, A. A. Demidov and P. M. Champion, "Wavelength selective modulation in femtosecond pump-probe spectroscopy and its application to heme proteins," *The Journal of Chemical Physics* 114(24), 10884-10898 (2001)
32. J. L. Herek, W. Wohlleben, R. J. Cogdell, D. Zeidler and M. Motzkus, "Quantum control of energy flow in light harvesting," *Nature* 417(6888), 533-535 (2002)
33. R. Fanciulli, I. Cerjak and J. L. Herek, "Low-noise rotating sample holder for ultrafast transient spectroscopy at cryogenic temperatures," *Review of Scientific Instruments* 78(5), 053102-053105 (2007)
34. P. Nuernberger, G. Krampert, T. Brixner and G. Vogt, "Rotation-translation device for condensed-phase spectroscopy with small sample volumes," *Review of Scientific Instruments* 77(8), 083113-083116 (2006)
35. B. Marchon and T. Olson, "Magnetic Spacing Trends: From LMR to PMR and Beyond," *IEEE Transactions on Magnetics* 45(10), 3608-3611 (2009)
36. P. Kambhampati, "Unraveling the Structure and Dynamics of Excitons in Semiconductor Quantum Dots," *Accounts of Chemical Research* 44(1), 1-13 (2010)

37. H. Zhu, Y. Yang and T. Lian, "Multiexciton Annihilation and Dissociation in Quantum Confined Semiconductor Nanocrystals," *Accounts of Chemical Research* (2012)
38. M. Sykora, A. Y. Kuposov, J. A. McGuire, R. K. Schulze, O. Tretiak, J. M. Pietryga and V. I. Klimov, "Effect of Air Exposure on Surface Properties, Electronic Structure, and Carrier Relaxation in PbSe Nanocrystals," *ACS Nano* 4(4), 2021-2034 (2010)
39. W. W. Yu, J. C. Falkner, B. S. Shih and V. L. Colvin, "Preparation and Characterization of Monodisperse PbSe Semiconductor Nanocrystals in a Noncoordinating Solvent," *Chemistry of Materials* 16(17), 3318-3322 (2004)
40. C. M. Evans, M. E. Evans and T. D. Krauss, "Mysteries of TOPSe Revealed: Insights into Quantum Dot Nucleation," *Journal of the American Chemical Society* 132(32), 10973-10975 (2010)
41. H. V. Carter, B. J. McClelland and E. Warhurst, "Studies of organo-alkali metal complexes. Part 4.-Absorption spectra in the visible region," *Transactions of the Faraday Society* 56(0), 455-458 (1960)
42. A. Berman, "Water vapor in vacuum systems," *Vacuum* 47(4), 327-332 (1996)
43. D. J. Crawley and L. de Csernatony, "Degassing characteristics of some 'O' ring materials," *Vacuum* 14(1), 7-9 (1964)
44. J. Farina and P. A. Bouis, "Use of ether solvents in organometallic synthesis the good the bad and the ugly," *Abstracts of Papers of the American Chemical Society* 214(Part 2), ORGN-132 (1997)
45. Y. Yamamoto, S. Nishida, X. H. Ma and K. Hayashi, "Pulse radiolysis of trans-stilbene in tetrahydrofuran. Spectral shift and decay kinetics of the radical anions in the presence of quaternary ammonium salts," *The Journal of Physical Chemistry* 90(9), 1921-1924 (1986)
46. Anonymous, "Vacuum Seals Design Criteria," in *Preferred Reliability Practices, Practice No. PD-ED-1223*, NASA, Lewis Research Center, Cleveland, OH (1998).
<http://engineer.jpl.nasa.gov/practices/1223.pdf>
47. J. H. Moore, C. C. Davis, M. A. Coplan and S. C. Greer, *Building Scientific Apparatus*, Cambridge University Press, New York (2009).

CHAPTER 4: FIRST 2D SPECTRUM ON OXYGEN-FREE AND SAMPLE-EXCHANGED COLLOIDAL QUANTUM DOTS

4.1 INTRODUCTION

For most samples, persistent dark states occur in single molecule spectroscopy.(1, 2) Such persistent states in quantum dots result in blinking. The mechanism of blinking is controversial but one hypothesis involves some kind of persistent charge separation or “charging.” Optical excitation of a charged dot can generate a trion comprised of an exciton (electron and hole) and a third charge (electron or hole). Trions decay via an Auger process, where the exciton component recombines to impart energy to the third charge.(3) Trion decay is reported to have a longer lifetime than bi-exciton decay by a factor of 7.5 ± 1.7 , and a shorter lifetime than single exciton decay by a factor of 2.2 ± 0.4 in colloidal CdSe/CdS core/shell quantum dots films.(4) As synthesis procedures and quantum dot materials are explored, variations in preparation and handling may cause differences in photo-physical behavior.

For fixed time delay, every pulse from the laser is an independent experiment on the sample; therefore any persistent state with a lifetime longer than the repetition rate of the laser necessitates sample-exchange (physical removal of the laser-excited sample volume) to ensure the sample is thermalized between shots. The consequence of ignoring this possibility could lead to a build-up of photo products, resulting in lifetimes and process quantum-yields that are muddled by persistent state populations; for example, it has been reported that trions arising from charging have been mistaken for bi-excitons arising from multiple exciton generation.

Two-dimensional spectroscopy is an important technique to explore coherent electronic and vibrational coupling in quantum dots, while thin film experiments can determine key photo-

physics for devices.(5) To date, no two-dimensional spectroscopy experiments have been reported for sample-exchanged colloidal quantum dots, nor has sample exchanging been reported on quantum dot thin films outside of our research group.(6) This chapter describes using the spinning sample cell characterized in Chapter 3 to conduct 2D spectroscopy on PbSe quantum dots and pump-probe experiments on quantum dot thin films.

4.2 EXPERIMENTAL SETUP

The experimental arrangement and characterization of the two-dimensional spectrometer has been described in detail in prior work(7, 8) but is summarized below to highlight key points. A 1 kHz repetition rate Ti:Sapphire regenerative amplifier (Spectra Physics, Spitfire Pro) pumps 40 μJ into a single-pass, short-wave infrared (IR) non-collinear optical parametric amplifier (NOPA)(9) that uses a Periodically Poled Stoichiometric Lithium Tantalate (PPSLT) crystal as the mixing medium with a ~ 2 μJ seed. Energy measurements were made with an energy meter (Molelectron, EMP 1000). Although spectral bandwidths of several hundred nanometers have been achieved with this particular NOPA,(8) a tuning-dependent bandwidth will be reported for each experiment. Pulse energy fluctuations of less than 0.5% were measured out of the NOPA.

The NOPA pulse is sent to a grating compressor with a 19-channel micro-machined membrane deformable mirror (Flexible Optical, BV model MMDM linear 11x39mm 19 ch). A genetic algorithm uses increases in the second harmonic generation (SHG) pulse energy to select individuals (mirror deformations) between generations. This approach has been implemented and described in other laser optimizations techniques.(10) This iteration continues until an acceptable fitness value shows convergence between generations (maximized for SHG pulse energy). The beam is then spatially filtered in the optical Fourier plane for collimation using a

250 μm pinhole. This pinhole transmitted approximately 690 nJ, 80% of the NOPA's input power, with an instability of less than 1%.

The *s*-polarized light is routed to the 2D spectrometer where it is split into two paths: one to a Mach-Zehnder interferometer mounted on a breadboard on top of a vibration-isolated table, the other to a Sagnac-interferometer (Figure 4.1 below). The Mach-Zehnder interferometer uses Inconel-alloy neutral density (ND) filters (New Focus, 523X) on a 1 mm thick glass substrate (Corning 7059) at Brewster's angle to preserve *s*-polarization, eliminate secondary reflections, minimize dispersion, and accommodate the broad bandwidth (1100–1600 nm) of the short-wave IR laser.

In this experiment, the Mach-Zehnder interferometer generates pulses *a* and *b*. The time delay between *a* and *b* is τ . The time delay between pulse *c* and the previous pulse (either *a* or *b*) is the waiting time, *T*. The time *t* is measured with respect to the center of pulse *c*. The delay between pulses *a* and *b* is actively stabilized by locking the interferometer displacement at integer multiples of the 632.8 nm HeNe wavelength with displacement errors of ~ 1 nm rms. This chapter discusses the use of this spectrometer for colloidal quantum dots. The spectrometer may be used for 2D short-wave IR spectroscopy as shown in the configuration of Figure 4.1, or one arm of the Mach-Zehnder interferometer can be blocked to perform pump-probe spectroscopy experiments.

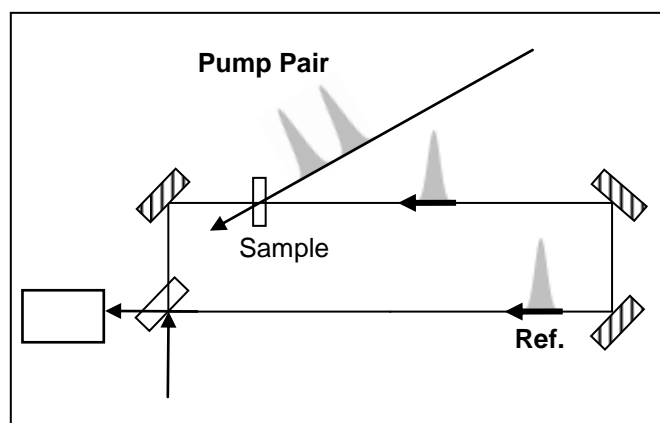


Fig. 4.1. Schematic of Sagnac interferometer for near-optimized interference detection of 2D spectra in the pump-probe geometry. The Sagnac input beam is split into a probe beam and reference beam by a beamsplitter (BS), with the reference beam passing through the sample before any other beam. Absorption of the probe by the sample will be modified by the pump pulse pair (from an actively stabilized Mach-Zehnder interferometer). The spectrum of this pump-pair disturbs the destructive interference between probe and reference beam at the “dark” output arm; this disturbance is the detected signal.

4.3 PUMP-PROBE EXPERIMENTS ON QUANTUM DOTS

A wavelength degenerate pump-probe experiment was conducted on ~ 3 nm PbSe quantum dots with 1136 nm exciton bandgap (FWHM of 128 nm) using an 1125 nm centered NOPA, with a 143 nm bandwidth (Figure 4.2). The experiment used 30 fs pulse durations with a ~ 10 nJ pump beam, at 1 kHz repetition rate. Figure 4.2 shows the bandwidth and center laser frequency of the NOPA output spectrum as resolved with a monochromator (SPEX, model 340S) and captured with an InGaAs optical multi channel analyzer (Princeton Instruments, OMA-V:1024-LN-2.2). This also shows that the laser spectrum possesses structure that could influence the shape of the 2D spectra. A sample-exchanged pump-probe measurement was compared to that for a static sample. The difference in amplitude of the photobleaching suggests that dark states persist for times longer than the period of the pulsed laser repetition.

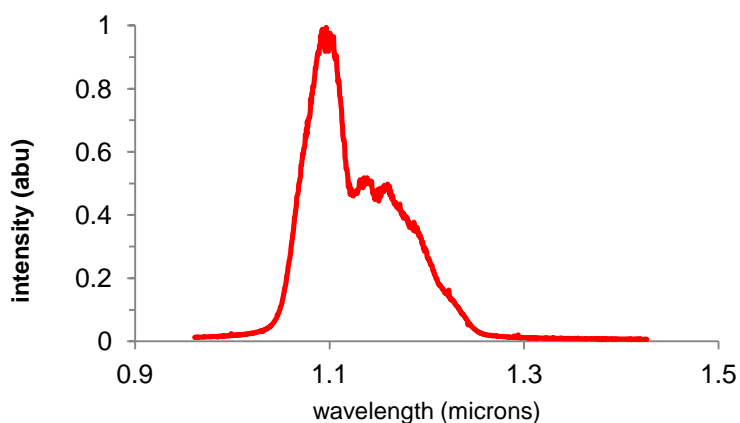


Fig. 4.2. The NOPA spectrum for pump-probe experiments on PbSe quantum dots. The center of the spectrum is 1.125 μm wavelength (1.1 eV), with a bandwidth of 143 nm.

Figure 4.3 shows photoluminescence and absorption spectra of the same PbSe quantum dot sample used for both the pump probe and the 2D quantum experiment. For quantum dots, it has been suggested that the shape and width of the emission peak matching those of the absorption peak is indicative of good surface passivation.⁽¹¹⁾ The peak in the linear absorption spectrum, taken with a UV-Vis-NIR spectrometer (Shimadzu, UV-3101) indicates an 1136 nm (1.09 eV) excitation bandgap. The photoluminescence spectrum was excited at 550 nm, filtered with an 800 nm long-pass filter, and then detected with a NIR spectrofluorometer (Photon Technologies, International Quantamaster).

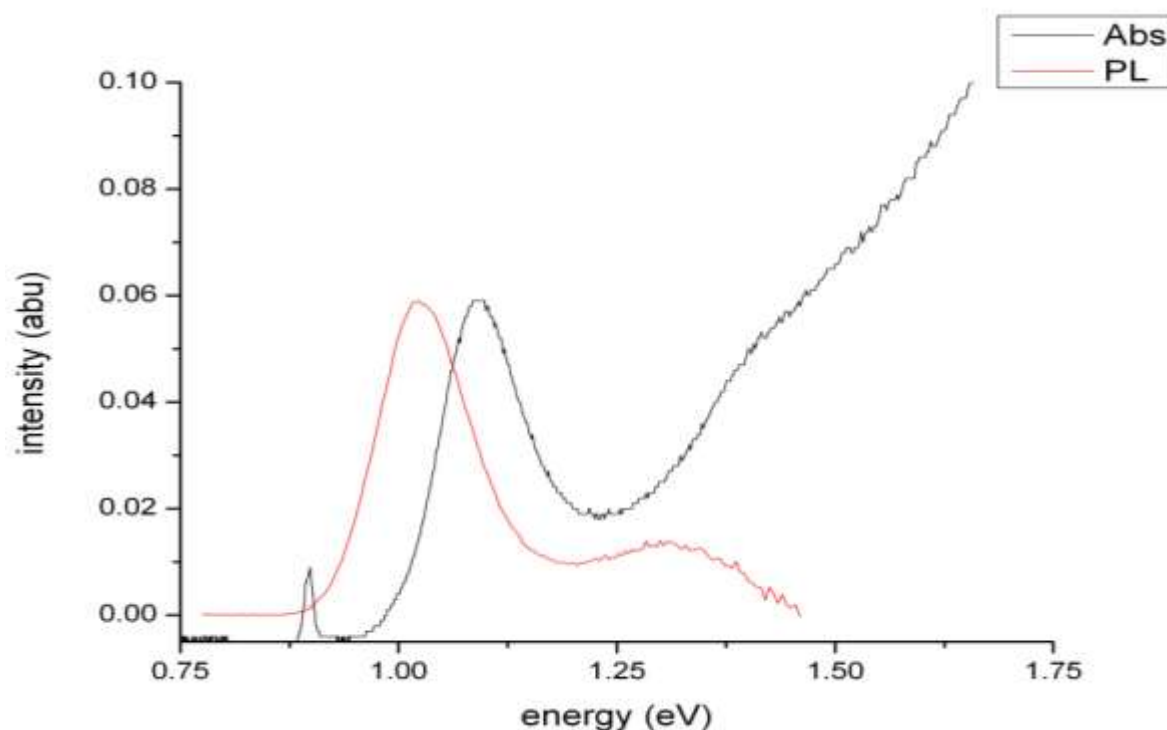


Fig 4.3. Absorption and photoluminescence spectra of 3 nm quantum dots. The peak shift between the two is indicative of a ~ 0.07 eV Stokes shift.

The higher pump-probe signal strength while spinning, shown in Figure 4.4, indicates that, for the static sample, some quantum dots are not in the equilibrium state. As will be shown later in the chapter, even though the noise has increased with a spinning sample cell over a static one, the signal-to-noise ratio with the spinning cell is still sufficient to obtain a 2D signal. Sample exchange with a spinning cell appears to produce a 2D spectrum that is different from the 2D spectrum in the static sample cell. This difference suggests that non-equilibrium states persist-for times longer than the period (1 ms) of the pulsed laser repetition (1 kHz). This illustrates the need to exchange samples between laser shots. Since photo-charging has been suggested to persist longer than 10s of milliseconds,(12) and is a proposed explanation of the dark states observed in the pump-probe experiment,(13) “photocharged” dots may be the persistent state causing altered 2D spectra in the static sample.

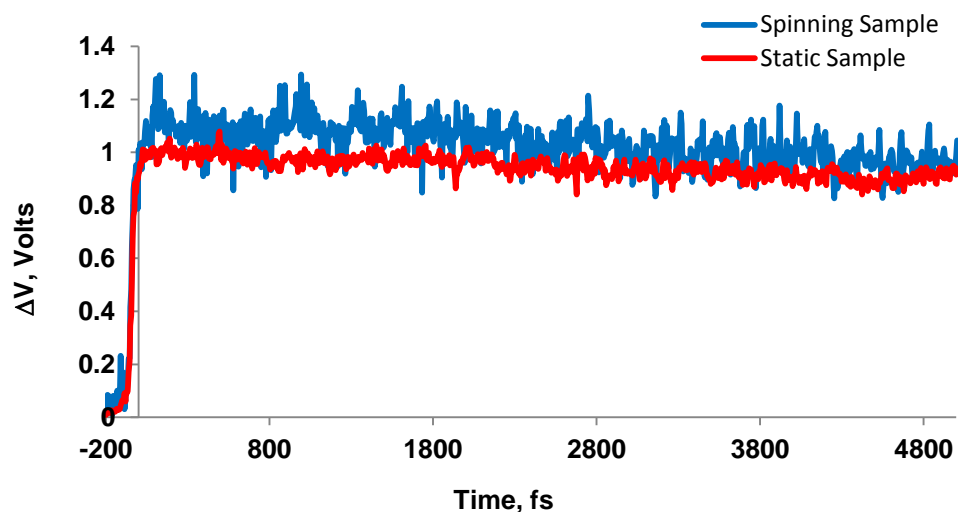


Fig. 4.4. Pump-probe transients of 1136 nm PbSe quantum dots (OD = 0.3), show an ~8% increase in differential transmission for the spinning cell over the static cell.

4.4 TWO-DIMENSIONAL SPECTROSCOPY ON QUANTUM DOTS

4.4.1 2D Colloidal Quantum Dot Measurements

A few groups have measured 2D spectra of quantum dots, though in none of these were the samples exchanged between shots. Wright and co-workers(14) used a tunable laser to map out 2D frequency domain spectra on PbSe. The technique lacks time-resolution shorter than the picosecond duration of the laser. They reported that the $1S \rightarrow 1S$ exciton fell down into a surface trap after ~1.5 ps. Three groups have reported experiments on colloidal quantum dots using 2D Fourier transform optical spectroscopy. Using a 5 kHz laser with a 12 fs duration pulses centered on 590 nm wavelength, Scholes and co-workers(15) measured 2D spectra for ~6 nm diameter CdSe, dissolved in toluene with 0.1 optical density in a 1 mm cuvette. They reported coupling and beating between the first two excitons in CdSe. Inhomogeneous broadening, negative features from exciton to bi-exciton absorption, and a 25 meV bi-exciton binding energy were reported. Spectra for waiting times T – less than 20 fs were not reported. Using pulses with 750–870 nm wavelength and 40 fs pulse duration at 5 kHz, Engel and co-workers(16) measured 2D

spectra for 2–3nm diameter PbS quantum dots. The sample was static in a 200 μm cuvette with 0.12 OD at 800 nm. They reported three peaks under the $1S \rightarrow 1S$ transition and attributed these peaks to intervalley splitting. Spectra for T less than 25 fs were not reported. The third group, Bylsma et al.,(17) did their experiments on a static ~ 3 nm PbS drop cast thin film at 833 nm using a 76 MHz rep rate Ti:sapphire laser with 100 micron spot size. They reported a 175 fs beating period corresponding to 24 meV energy difference that they attributed to intervalley splitting. In addition, Bawendi and Ruhman have measured spectrally resolved pump-probe transients from which they deduce a bi-exciton binding energy of 16 meV in PbSe.(18)

A number of predictions more relevant to PbSe(19-21) have been made about intervalley splitting.(22) Zunger(21) predicted two absorption peaks in spherical PbSe quantum dots due to this intervalley coupling. Mukamel and co-workers(23) predicted additional peaks in the 2D spectra for epitaxially charged quantum dots.(23) Some have ascribed blinking to photo-charging,(24, 25) while others have suggested alternative hypotheses.(26)

With these predictions, we set out to conduct 2D optical spectroscopy experiments on PbSe quantum dots. The first order was to examine the differences between 2D spectra taken with a static sample compared to a spinning sample designed to help avoid repetitive excitation. The quantum dots would be probed at bandgap so that many of the aforementioned measurement considerations and predictions involving the $1S \rightarrow 1S$ transitions are applicable.

4.4.2 Experimental Conditions

Three nanometer diameter PbSe quantum dots in isocetane solution were prepared with a 0.3 OD in an optical path length of 200 μm . Prior to the experiment, the 2D spectrometer was used to make measurements on dye IR26 to ensure the spectrometer was producing results that were consistent with prior work in our group.(8) The dots were measured with a transmission

electron microscope (Philips, FEI CM200) and found to have two sizes: 3-3.2 nm on the short dimension, and 4.3-4.6 nm on the longer dimension. The PbSe quantum dots had a first exciton absorption peak at 1136 nm with a FWHM of 128 nm. Pulse energies were too weak to be measured with our current joule meter (10 nJ sensitivity), but were estimated to be between 5 and 10 nJ by measuring the input pulse energy and calculating for the reflections and transmissions through ND beamsplitters before it reached the sample. Beam sizes of ~ 3 mm were focused down to ~ 50 μm at the sample using an $f = 7.5$ cm focal length plano-convex lens (1 in. diameter).

4.4.3 Data Processing

For any given mixing period T , the evolution period τ was scanned by setting the delay of pulse b at T , moving pulse a forward from $(\tau + T)$ to T , and then moving pulse b backward from T to $(\tau + T)$, in time steps of red HeNe lockpoints of 2.11 fs. Spectral interferograms between pulse c and the signal were taken at each position. To ensure an overlap of pulses a and b , a buffer of 30 fs (nearly 1 beat cycle of the red and yellow Helium Neon laser's) was added to our 300 fs τ -scan. The mixing period, T , was set within 0.66 fs accuracy by fitting symmetric pump-probe and probe-pump scans to hyperbolic tangents and determining the crossing point to be $T = 0$ fs. The overlapping stage position for $\tau = 0$ was interferometrically determined by routing the collinear pump pulses to a photodiode. While determining $\tau = 0$, the yellow and red HeNe lasers were measured concurrently with the interferograms to find the stitching point (nearest $\tau = 0$) for the two halves of our interferograms.

In the partially non-collinear geometry, the desired 2D signal co-propagates with our third pulse. Rephasing and non-rephasing signals are collected simultaneously. In the pump-probe geometry, the signal selectively measures absorptive (real) 2D spectra. Additional signals

that appear in the same phase matched direction include free induction decay from pulse c and pump-probe signals from pulses a and b separately. The desired 2D signal is isolated by Fourier transformation with respect to τ . Because the signal field is real in the time domain (hence $E^*(\omega_\tau) = E(-\omega_\tau)$ in the frequency domain), the amplitude modulated signal should be symmetric at about $\tau = 0$. Thus, no phase correction is needed, and processing requires only inclusion of the actual delays τ due to the uniform shift of all data points off an integer number of HeNe periods in the piezo-electric transducer locking scheme. In other words, the data points are obtained at roughly $\tau = (n+1/4)$ (2.11 fs), so there is no $\tau = 0$ point, etc. This uniform time domain shift of all data points can be accounted for in processing by Fourier transforming the data into the frequency domain where the frequency-dependent phase for the time delay shift is removed. After inverse Fourier transforming back into the time domain, one can verify that the frequency dependent phase has been removed by confirming that the time domain interferograms are even about $\tau = 0$. Any peaks in the imaginary 2D spectra are believed to arise from noise, which is on the order of 10% here.

4.4.4 Results

A two-dimensional Fourier transform spectra was collected with the cell spinning and a static cell for $T = 0$ and $T = 100$ fs. A key point is that 2D data can be collected with a spinning cell. Although the data are preliminary, spinning is likely to be useful for this experiment. The 2D spectra have the same overall shape but may differ in small details. For example, a feature near 1.08 eV seems to be less prominent in the spinning data, but this has not been confirmed by repeated measurement. All spectra show three features in common and both $T = 0$ 2D spectra show a negative region above the diagonal.

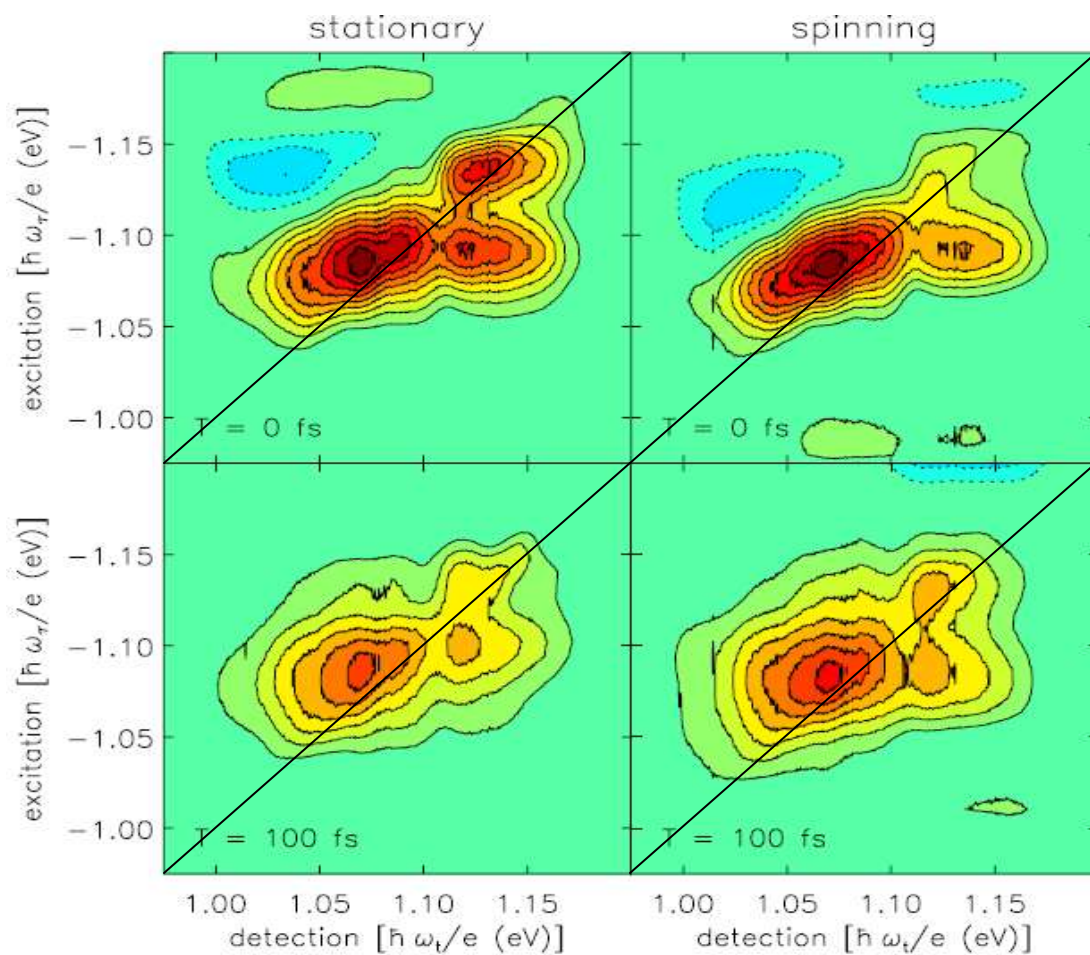


Fig. 4.5. 2D FT optical spectra for spinning (right) and static (left) samples of ~ 3 nm PbSe quantum dots with exciton transitions at 1136 nm. The upper row contains data at waiting time $T = 0$. The lower row is $T = 100$ fs.

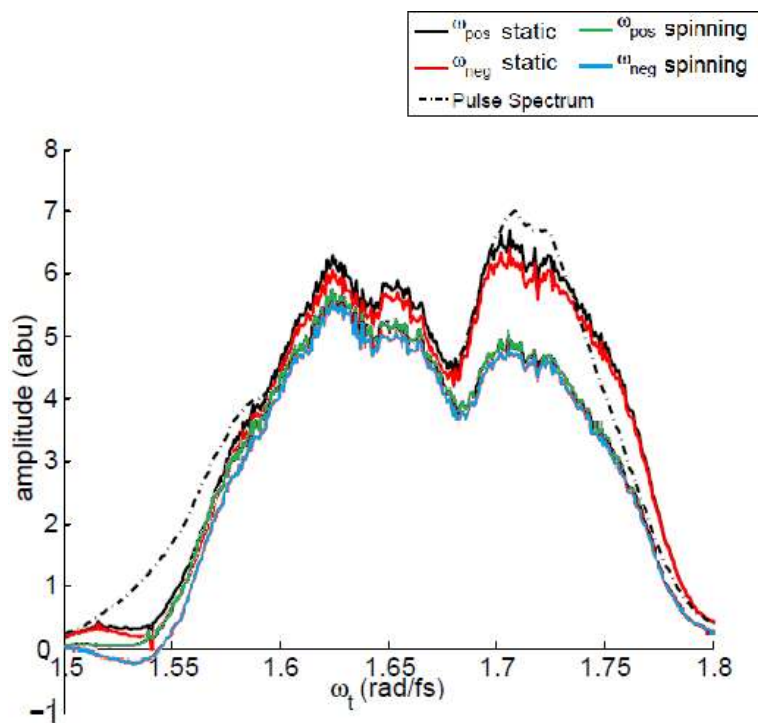


Fig. 4.6. A projection in the 2D FT optical spectrum onto ω_t reveals that features of the laser pulse spectra have been mapped into the 2D spectra, notably the split peak.

4.5 PUMP-PROBE EXPERIMENTS ON PBSE THIN-FILM DOTS

4.5.1 Experimental Preparation

The thin films for this experiment were made by repeatedly dipping a hard disk glass substrate into a solvated colloidal PbSe quantum dot solution. This was repeated until a sufficient thickness, on the order of 200 μm , was deposited on the hard disk glass substrate. This hard disk glass substrate is the same that was characterized in Chapter 3. The films were then treated with EDT (1,2-ethanedithiol, $\text{HS-CH}_2\text{-CH}_2\text{-SH}$)^(27, 28) and then loaded into the sample chamber while in the glovebox. The transmission spectra in Figure 4.7 were taken for the following purposes: to characterize the first exciton peak at 1530 nm; to measure the optical density of the sample (~ 0.4 at 1530 nm); and to test for oxygen leaks over the course of the experiment, in this case, over more than 36 hours. PbSe is quite sensitive to oxygen and has been known to oxidize

in a matter of minutes when exposed to air.(29, 30) Based on the absorption peak and an empirically-derived equation for sizing PbSe quantum dots from Hens and co-workers,(31) the quantum dots are ~5 nm in diameter. After the initial absorption spectra were measured, the sample was placed in the pump-probe apparatus described below.

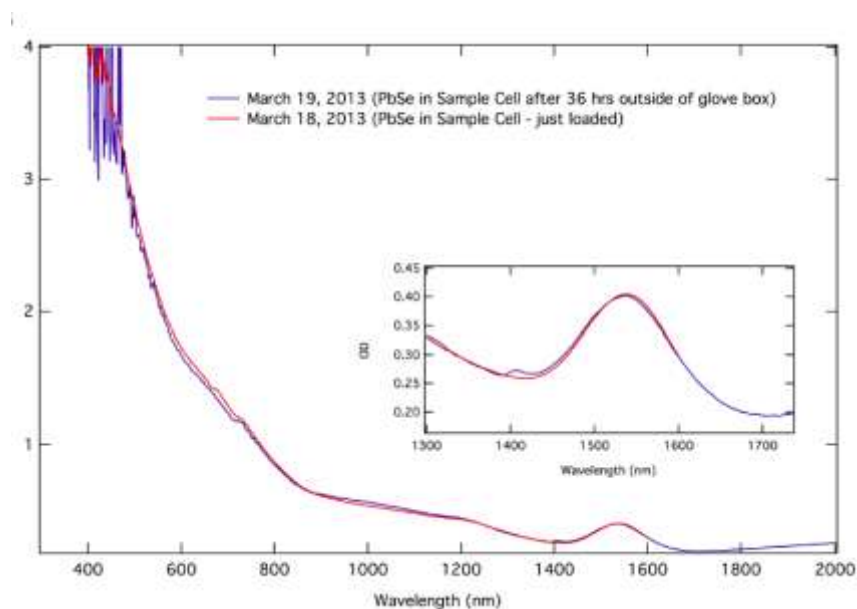


Fig. 4.7. Absorption spectra of (300 nm thick) thin films of PbSe sample chamber after the sample chamber was sitting in the open air for 36 h outside the glove box with 1530 nm exciton peak. The instrumental and substrate base line has not been subtracted off the spectra, which gives the non-zero features to the right of the exciton peak.

4.5.2 Experimental Conditions

A Ti:sapphire oscillator (KM Labs, Chinook) seeds a Ti: sapphire amplifier (Quantronix, Integra-E) , to produce a 60 fs, 810 nm pump, for two independently tunable OPAs (Light Conversion, TOPAS). One of these OPAs is used as a 1530 nm probe, while the other produces the pump for both experiments described below. The pump is chopped (New Focus, model 3501) at a 500 Hz rate synchronized to the 1 kHz laser repetition rate. The light is collected on a

photodiode and data sampled with a SRS Boxcar analyzer. Additional details may be found in reference. (32, 33) The first experiment used a 6 nJ pump (at 1200 nm wavelength) and a 1530 nm probe. The second experiment used a 10 nJ pump (at 330 nm wavelength) and a 1530 nm probe. The probe beams were less than 150 microns in diameter and about one-third of the pump beam diameter to avoid spatial inhomogeneities of the pump beam. A reference pulse routed around the sample was used to account for pulse-to-pulse variability of the laser through normalization.

4.5.3 Results

The pump probe measurements, Figure 4.8, show a characteristically faster initial decay time scale for the 330 nm pumped sample compared with the 1200 nm pumped sample. The 330 nm photon energy would be above the threshold needed for multiple exciton generation.(34) In the 300 nm experiments, it would appear that there is no noticeable difference between the spinning sample cell and the static sample cell. This is less obvious for the lower energy experiment, pumped at 1200 nm. The peak is not well-resolved in the sub-75 ps regime, and longer averaging in that range is needed to elucidate whether sample exchange makes a difference in the apparent decay rate. This is especially important when trying to determine accurate rates for processes such as Auger recombination.

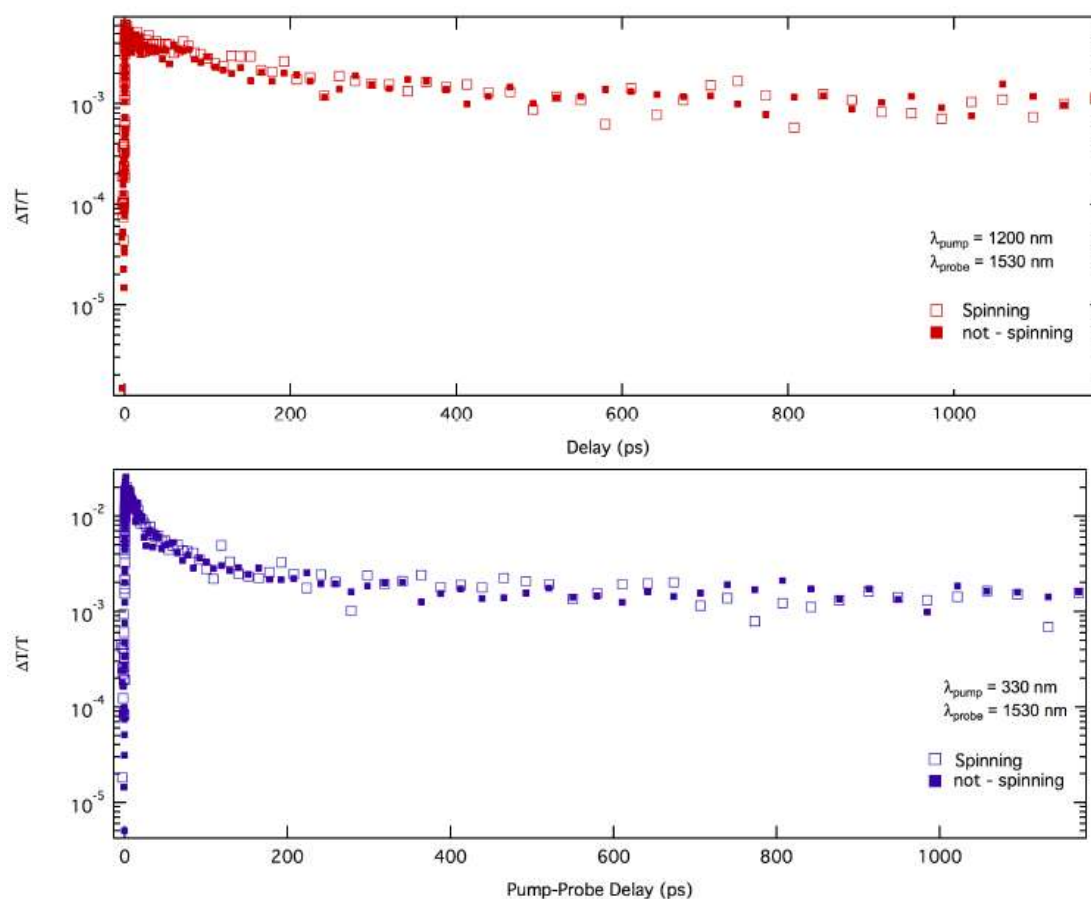


Fig. 4.8. Comparison of thin film measurements on spinning vs. static samples of PbSe thin films, $\sim 300 \text{ nm}$ thick. The top transient is for an experiment pumped at $h\nu = 1.2 \times$ bandgap and probed at bandgap, 1530 nm. The bottom transient is for an experiment pumped at $h\nu = 4.6 \times$ bandgap and also probed at the 1530 nm bandgap.

4.6 CONCLUSIONS

The pump-probe data suggest that there is no difference between spinning and static cases for this PbSe thin film with this surface treatment at a pump wavelength of 330 nm. More experimentation should be done with 1200 nm pumped thin films. These results may or may not apply for other samples; however, this new capability for thin film quantum dot experiments should afford a means of directly removing longer-lived photo products between laser shots.

For 2D spectroscopy measurements and pump-probe, experiments on colloidal quantum dots show that sample exchange makes a difference. Demonstrating that the 2D spectrometer can remain displacement-locked during measurements while keeping the sample oxygen-free is an accomplishment. The pump-probe measurements establish that static measurements probe some non-equilibrium states of quantum dots. Determining what possible specific differences mean in the 2D spectra, and what the structure of the 2D spectrum implies about the photo-physics of quantum dots under repetitive vs. single excitation will likely require careful analysis and repeated measurements under a variety of conditions.

REFERENCES FOR CHAPTER 4

1. P. Tyagi and P. Kambhampati, "False multiple exciton recombination and multiple exciton generation signals in semiconductor quantum dots arise from surface charge trapping," *Journal of Chemical Physics* 134(9), 10 (2012)
2. I. Rasnik, S. A. McKinney and T. Ha, "Nonblinking and long-lasting single-molecule fluorescence imaging," *Nat Meth* 3(11), 891-893 (2006)
3. N. Poklonskii, A. Syaglo and S. Vyrko, "Analog of the Auger effect in radiative decay of a trion in a quantum well," *Journal of Applied Spectroscopy* 68(3), 371-376 (2001)
4. P. P. Jha and P. Guyot-Sionnest, "Trion Decay in Colloidal Quantum Dots," *ACS Nano* 3(4), 1011-1015 (2009)
5. O. E. Semonin, J. M. Luther, S. Choi, H.-Y. Chen, J. Gao, A. J. Nozik and M. C. Beard, "Peak External Photocurrent Quantum Efficiency Exceeding 100% via MEG in a Quantum Dot Solar Cell," *Science* 334(6062), 1530-1533 (2011)
6. Danielle M. Buckley, Austin P. Spencer; Dmitry Baranov; Trevor L. Courtney; David M. Jonas, "Degenerate Femtosecond Pump Probe Studies of Lead Sulfide Nanocrystals at the Band Gap," in *23rd Rocky Mountain Regional Meeting of the American Chemical Society*, Westminster, CO, United States (2012).
7. T. L. Courtney, S. D. Park, R. J. Hill and D. M. Jonas, "Enhanced Interferometric Detection in 2D Spectroscopy with a Sagnac Interferometer," *Optics Letters* (to be submitted)
8. T. L. Courtney, "Bringing Two-Dimensional Fourier Transform Electronic Spectroscopy into the Short-Wave Infrared," Ph.D. Thesis, p. 206, University of Colorado, Boulder, Colorado (2012).
9. J. Piel, E. Riedle, L. Gundlach, R. Ernstorfer and R. Eichberger, "Sub-20 fs visible pulses with 750 nJ energy from a 100 kHz noncollinear optical parametric amplifier," *Optics Letters* 31(9), 1289-1291 (2006)
10. R. A. Bartels, "Coherent Control of Atoms and Molecules " Ph.D. Thesis, p. 216, University of Colorado, Boulder, Colorado (2002).
11. M. J. Fernee, P. Jensen and H. Rubinsztein-Dunlop, "Origin of the large homogeneous line widths obtained from strongly quantum confined PbS nanocrystals at room temperature," *Journal of Physical Chemistry C* 111(13), 4984-4989 (2007)
12. C. Galland, Y. Ghosh, A. Steinbruck, M. Sykora, J. A. Hollingsworth, V. I. Klimov and H. Htoon, "Two types of luminescence blinking revealed by spectroelectrochemistry of single quantum dots," *Nature* 479(7372), 203-207 (2011)

13. D. E. Gómez, J. van Embden, P. Mulvaney, M. J. Fernée and H. Rubinsztein-Dunlop, "Exciton–Trion Transitions in Single CdSe–CdS Core–Shell Nanocrystals," *ACS Nano* 3(8), 2281-2287 (2009)
14. S. B. Block, L. A. Yurs, A. V. Pakoulev, R. S. Selinsky, S. Jin and J. C. Wright, "Multiresonant Multidimensional Spectroscopy of Surface-Trapped Excitons in PbSe Quantum Dots," *Journal of Physical Chemistry Letters* 3(18), 2707-2712 (2012)
15. D. B. Turner, Y. Hassan and G. D. Scholes, "Exciton Superposition States in CdSe Nanocrystals Measured Using Broadband Two-Dimensional Electronic Spectroscopy," *Nano Letters* 12(2), 880-886 (2011)
16. E. Harel, S. M. Rupich, R. D. Schaller, D. V. Talapin and G. S. Engel, "Measurement of electronic splitting in PbS quantum dots by two-dimensional nonlinear spectroscopy," *Physical Review B* 86(7), 5 (2012)
17. J. Bylsma, P. Dey, J. Paul, S. Hoogland, E. H. Sargent, J. M. Luther, M. C. Beard and D. Karauskaj, "Quantum beats due to excitonic ground-state splitting in colloidal quantum dots," *Physical Review B* 86(12), 125322 (2012)
18. I. Gdor, H. Sachs, A. Roitblat, D. B. Strasfeld, M. G. Bawendi and S. Ruhman, "Exploring Exciton Relaxation and Multiexciton Generation in PbSe Nanocrystals Using Hyperspectral Near-IR Probing," *ACS Nano* 6(4), 3269-3277 (2012)
19. I. Kang and F. W. Wise, "Electronic structure and optical properties of PbS and PbSe quantum dots," *J. Opt. Soc. Am. B* 14(7), 1632-1646 (1997)
20. J. M. An, A. Franceschetti, S. V. Dudy and A. Zunger, "The Peculiar Electronic Structure of PbSe Quantum Dots," *Nano Letters* 6(2728-2735) (2006)
21. J. M. An, A. Franceschetti and A. Zunger, "The Excitonic Exchange Splitting and Radiative Lifetime in PbSe Quantum Dots," *Nano Letters* 7(2129-2135) (2007)
22. S. Y. Ren, "Quantum confinement of edge states in Si crystallites," *Physical Review B* 55(7), 4665-4669 (1997)
23. B. P. Fingerhut, M. Richter, J.-W. Luo, A. Zunger and S. Mukamel, "2D optical photon echo spectroscopy of a self-assembled quantum dot," *Annalen der Physik* doi 10.1002/p/201200204 (2013)
24. V. Fomenko and D. J. Nesbitt, "Solution Control of Radiative and Nonradiative Lifetimes: A Novel Contribution to Quantum Dot Blinking Suppression," *Nano Letters* 8(1), 287-293 (2007)
25. A.L. Efros and M. Rosen, *Phys. Rev. Lett.* 78 1110 (1997)

26. P. A. Frantsuzov and R. A. Marcus, "Explanation of quantum dot blinking without the long-lived trap hypothesis," *Physical Review B* 72(15), 155321 (2005)
27. M. Law, J. M. Luther, Q. Song, B. K. Hughes, C. L. Perkins and A. J. Nozik, "Structural, Optical, and Electrical Properties of PbSe Nanocrystal Solids Treated Thermally or with Simple Amines," *Journal of the American Chemical Society* 130(18), 5974-5985 (2008)
28. D. A. R. Barkhouse, A. G. Pattantyus-Abraham, L. Levina and E. H. Sargent, "Thiols Passivate Recombination Centers in Colloidal Quantum Dots Leading to Enhanced Photovoltaic Device Efficiency," *ACS Nano* 2(11), 2356-2362 (2008)
29. M. Sykora, A. Y. Kuposov, J. A. McGuire, R. K. Schulze, O. Tretiak, J. M. Pietryga and V. I. Klimov, "Effect of Air Exposure on Surface Properties, Electronic Structure, and Carrier Relaxation in PbSe Nanocrystals," *ACS Nano* 4(4), 2021-2034 (2010)
30. Q. Q. Dai, Y. N. Wang, Y. Zhang, X. B. Li, R. W. Li, B. Zou, J. Seo, Y. D. Wang, M. H. Liu and W. W. Yu, "Stability Study of PbSe Semiconductor Nanocrystals over Concentration, Size, Atmosphere, and Light Exposure," *Langmuir* 25(20), 12320-12324 (2009)
31. I. Moreels, K. Lambert, D. De Muynck, F. Vanhaecke, D. Poelman, J. C. Martins, G. Allan and Z. Hens, "Composition and size-dependent extinction coefficient of colloidal PbSe quantum dots," *Chemistry of Materials* 19(25), 6101-6106 (2007)
32. M. C. Beard and R. J. Ellingson, "Multiple exciton generation in semiconductor nanocrystals: Toward efficient solar energy conversion," *Laser & Photonics Reviews* 2(5), 377-399 (2008)
33. J. M. Luther, M. C. Beard, Q. Song, M. Law, R. J. Ellingson and A. J. Nozik, "Multiple exciton generation in films of electronically coupled PbSe quantum dots," *Nano Letters* 7(6), 1779-1784 (2007)
34. J. T. Stewart, L. A. Padilha, M. M. Qazilbash, J. M. Pietryga, A. G. Midgett, J. M. Luther, M. C. Beard, A. J. Nozik and V. I. Klimov, "Comparison of Carrier Multiplication Yields in PbS and PbSe Nanocrystals: The Role of Competing Energy-Loss Processes," *Nano Letters* 12(2), 622-628 (2012)

BIBLIOGRAPHY

- U. Åberg, E. Åkesson, J. L. Alvarez, I. Fedchenia and V. Sundström, "Femtosecond spectral evolution monitoring the bond-twisting event in barrierless isomerization in solution," *Chemical Physics* 183(2-3), 269-288 (1994)
- R. S. Adrain, E. G. Arthurs, D. J. Bradley, A. G. Roddie and J. R. Taylor, "Amplification of picosecond dye laser pulses," *Optics Communications* 12(2), 140-142 (1974)
- Anonymous, "Vacuum Seals Design Criteria," in *Preferred Reliability Practices, Practice No. PD-ED-1223*, NASA, Lewis Research Center, Cleveland, OH (1998).
<http://engineer.jpl.nasa.gov/practices/1223.pdf>
- N. W. Ashcroft and N. D. Mermin, *Solid State Physics*, Saunders College, Philadelphia (1976).
- D. A. R. Barkhouse, A. G. Pattantyus-Abraham, L. Levina and E. H. Sargent, "Thiols Passivate Recombination Centers in Colloidal Quantum Dots Leading to Enhanced Photovoltaic Device Efficiency," *ACS Nano* 2(11), 2356-2362 (2008)
- R. A. Bartels, "Coherent Control of Atoms and Molecules " PhD Thesis, p. 216, University of Colorado, Boulder, Colorado (2002).
- S. Basu, "Nd-YAG and Yb-YAG rotary disk lasers," *IEEE Journal of Selected Topics in Quantum Electronics* 11(3), 626-630 (2005)
- S. Basu, T. Kane and R. Byer, "A proposed 1 kW average power moving slab Nd:Glass laser," *IEEE Journal of Quantum Electronics* 22(10), 2052-2057 (1986)
- S. Basu and R. L. Byer, "Average power limits of diode-laser-pumped solid state lasers," *Applied Optics* 29(12), 1765-1771 (1990)
- M. C. Beard, A. G. Midgett, M. C. Hanna, J. M. Luther, B. K. Hughes and A. J. Nozik, "Comparing Multiple Exciton Generation in Quantum Dots To Impact Ionization in Bulk Semiconductors: Implications for Enhancement of Solar Energy Conversion," *Nano Letters* 10(8), 3019-3027 (2010)
- M. C. Beard and R. J. Ellingson, "Multiple exciton generation in semiconductor nanocrystals: Toward efficient solar energy conversion," *Laser & Photonics Reviews* 2(5), 377-399 (2008)
- N. Belabas and D. M. Jonas, "Three-dimensional view of signal propagation in femtosecond four-wave mixing with application to the boxcars geometry," *J. Opt. Soc. Am. B* 22(3), 655-674 (2005)

- W. E. Bell, "Vacuum sealing of gas laser windows," *US Patent 3,390,351* (1968)
- P. Bender, D. Currie, R. Dicke, D. Eckhardt, J. E. Faller, W. Kaula, J. Mulholland, H. Plotkin, S. Poultnery and E. Silverberg, "The lunar laser ranging experiment," *Science* 182(4109), 229-238 (1973)
- M. Ben-Lulu, D. Mocatta, M. Bonn, U. Banin and S. Ruhman, "On the absence of detectable carrier multiplication in a transient absorption study of InAs/CdSe/ZnSe core/shell1/shell2 quantum dots," *Nano Letters* 8(4), 1207-1211 (2008)
- A. Berman, "Water vapor in vacuum systems," *Vacuum* 47(4), 327-332 (1996)
- S. B. Block, L. A. Yurs, A. V. Pakoulev, R. S. Selinsky, S. Jin and J. C. Wright, "Multiresonant Multidimensional Spectroscopy of Surface-Trapped Excitons in PbSe Quantum Dots," *Journal of Physical Chemistry Letters* 3(18), 2707-2712 (2012)
- Z. Bleier, I. Vishnia and J. Lipkins, "Hollow Retroreflectors Promote Precision Optical Alignment," *Photonics Spectra* 38(3), 82-91 (2004)
- R. D. Blomberg, A. Hale and D. F. Preusser, "Experimental evaluation of alternative conspicuity-enhancement techniques for pedestrians and bicyclists," *Journal of Safety Research* 17(1), 1-12 (1986)
- M. Boiteux and O. de Witte, "A Transverse Flow Repetitive Dye Laser," *Applied Optics* 9(2), 514-515 (1970)
- U. Brackmann, *Lamdachrome Laser Dyes*, Lambda Physik, Gottingen (1986).
- J. Bredenbeck and P. Hamm, "Versatile small volume closed-cycle flow cell system for transient spectroscopy at high repetition rates," *Review of Scientific Instruments* 74(6), 3188-3189 (2003)
- T. Briles, D. Yost, A. Cingöz, J. Ye and T. Schibli, "Simple piezoelectric-actuated mirror with 180 kHz servo bandwidth," *Optics Express* 18(10), 9739-9746 (2010)
- L. E. Brus, "A Simple-Model for the Ionization-Potential, Electron-Affinity, and Aqueous Redox Potentials of Small Semiconductor Crystallites," *Journal of Chemical Physics* 79(11), 5566-5571 (1983)
- Danielle M. Buckley, Austin P. Spencer; Dmitry Baranov; Trevor L. Courtney; David M. Jonas, "Degenerate Femtosecond Pump Probe Studies of Lead Sulfide Nanocrystals at the Band Gap," in *23rd Rocky Mountain Regional Meeting of the American Chemical Society*, Westminster, CO, United States (2012).
- P. N. Butcher and D. Cotter, *The Elements of Nonlinear Optics*, Cambridge University Press, New York (1991).

- R. L. Byer, "High power solid state laser," *US Patent 4555786* (1985)
- J. Bylsma, P. Dey, J. Paul, S. Hoogland, E. H. Sargent, J. M. Luther, M. C. Beard and D. Karaiskaj, "Quantum beats due to excitonic ground-state splitting in colloidal quantum dots," *Physical Review B* 86(12), 125322 (2012)
- H. V. Carter, B. J. McClelland and E. Warhurst, "Studies of organo-alkali metal complexes. Part 4.-Absorption spectra in the visible region," *Transactions of the Faraday Society* 56(0), 455-458 (1960)
- B. Cho, W. K. Peters, R. J. Hill, T. L. Courtney and D. M. Jonas, "Bulklike Hot Carrier Dynamics in Lead Sulfide Quantum Dots," *Nano Letters* 10(7), 2498-2505 (2010)
- B. Cho, W. K. Peters, R. J. Hill, T. L. Courtney and D. M. Jonas, "Hot Carrier Dynamics in Lead Sulfide Nanocrystals," in *Ultrafast Phenomena XVII*, Oxford University Press, New York (2010).
- T. L. Courtney, "Bringing Two-Dimensional Fourier Transform Electronic Spectroscopy into the Short-Wave Infrared," Ph.D., p.206, University of Colorado, Boulder, Colorado (2012).
- T. L. Courtney, S. D. Park, R. J. Hill and D. M. Jonas, "Enhanced Interferometric Detection in 2D Spectroscopy with a Sagnac Interferometer," *Optics Letters* (to be submitted)
- D. J. Crawley and L. de Csernatony, "Degassing characteristics of some 'O' ring materials," *Vacuum* 14(1), 7-9 (1964)
- Q. Dai, Y. Wang, Y. Zhang, X. Li, R. Li, B. Zou, J. Seo, Y. Wang, M. Liu and W. W. Yu, "Stability study of PbSe semiconductor nanocrystals over concentration, size, atmosphere, and light exposure," *Langmuir* 25(20), 12320-12324 (2009)
- A. S. De Vany, "Master optical techniques," *Wiley Series in Pure and Applied Optics*, New York: Wiley, 1981 1((1981)
- B.V. De Waele, M. Beutter, U. Schmidhammer, E. Riedle and J. Daub, "Switching dynamics of the photochromic 1,1-dicyano-2-(4-cyanophenyl)-1,8a-dihydroazulene probed by sub-30 fs spectroscopy," *Chemical Physics Letters* 390(4-6), 328-334 (2004)
- C. Dorrer, N. Belabas, J.-P. Likforman and M. Joffre, "Spectral resolution and sampling issues in Fourier-transform spectral interferometry," *J. Opt. Soc. Am. B* 17(10), 1795-1802 (2000)
- A.L. Efros and M. Rosen, *Phys. Rev. Lett.* 78(1110) (1997)

A. A. O. A.I. Ekimov, V.A. Tzehomskii, *Sov. Phys. Chem. Glass (Fiz. Khim. Stekla)* 6(511(1980)

C. M. Evans, M. E. Evans and T. D. Krauss, "Mysteries of TOPSe Revealed: Insights into Quantum Dot Nucleation," *Journal of the American Chemical Society* 132(32), 10973-10975 (2010)

R. Fanciulli, I. Cerjak and J. L. Herek, "Low-noise rotating sample holder for ultrafast transient spectroscopy at cryogenic temperatures," *Review of Scientific Instruments* 78(5), 053102-053105 (2007)

J. Farina and P. A. Bouis, "Use of ether solvents in organometallic synthesis the good the bad and the ugly," *Abstracts of Papers of the American Chemical Society* 214(Part 2), ORGN-132 (1997)

M. J. Fernee, P. Jensen and H. Rubinsztein-Dunlop, "Origin of the large homogeneous linewidths obtained from strongly quantum confined PbS nanocrystals at room temperature," *Journal of Physical Chemistry C* 111(13), 4984-4989 (2007)

B. P. Fingerhut, M. Richter, J.-W. Luo, A. Zunger and S. Mukamel, "2D optical photon echo spectroscopy of a self-assembled quantum dot," *Annalen der Physik* doi 10.1002/p/201200204 (2013)

B. P. Fingerhut, M. Richter, J.-W. Luo, A. Zunger and S. Mukamel, "Dissecting biexciton wave functions of self-assembled quantum dots by double-quantum-coherence optical spectroscopy," *Physical Review B* 86(23), 235303 (2012)

J. M. An, A. Franceschetti and A. Zunger, "The Excitonic Exchange Splitting and Radiative Lifetime in PbSe Quantum Dots," *Nano Letters* 7(2129-2135 (2007)

A. Franceschetti, J. M. An and A. Zunger, "Impact ionization can explain carrier multiplication in PbSe quantum dots," *Nano Letters* 6(10), 2191-2195 (2006)

J. M. An, A. Franceschetti and A. Zunger, "The Excitonic Exchange Splitting and Radiative Lifetime in PbSe Quantum Dots," *Nano Letters* 7(2129-2135 (2007)

J. M. An, A. Franceschetti, S. V. Dudiy and A. Zunger, "The Peculiar Electronic Structure of PbSe Quantum Dots," *Nano Letters* 6(2728-2735 (2006)

P. A. Frantsuzov and R. A. Marcus, "Explanation of quantum dot blinking without the long-lived trap hypothesis," *Physical Review B* 72(15), 155321 (2005)

S. M. Gallagher Faeder and D. M. Jonas, "Two-Dimensional Electronic Correlation and Relaxation Spectra: Theory and Model Calculations," *Journal of Physical Chemistry A* 103(49), 10489-10505 (1999)

- C. Galland, Y. Ghosh, A. Steinbruck, M. Sykora, J. A. Hollingsworth, V. I. Klimov and H. Htoon, "Two types of luminescence blinking revealed by spectroelectrochemistry of single quantum dots," *Nature* 479(7372), 203-207 (2011)
- I. Gdor, H. Sachs, A. Roitblat, D. B. Strasfeld, M. G. Bawendi and S. Ruhman, "Exploring Exciton Relaxation and Multiexciton Generation in PbSe Nanocrystals Using Hyperspectral Near-IR Probing," *ACS Nano* 6(4), 3269-3277 (2012)
- D. E. Gómez, J. van Embden, P. Mulvaney, M. J. Fernée and H. Rubinsztein-Dunlop, "Exciton–Trion Transitions in Single CdSe–CdS Core–Shell Nanocrystals," *ACS Nano* 3(8), 2281-2287 (2009)
- H. Gratz, A. Penzkofer, C. Abels, R. M. Szeimies, M. Landthaler and W. Bäuml, "Photo-isomerisation, triplet formation, and photo-degradation dynamics of indocyanine green solutions," *Journal of Photochemistry and Photobiology A: Chemistry* 128(1–3), 101-109 (1999)
- E. Harel, S. M. Rupich, R. D. Schaller, D. V. Talapin and G. S. Engel, "Measurement of electronic splitting in PbS quantum dots by two-dimensional nonlinear spectroscopy," *Physical Review B* 86(7), 075412 (2012)
- H.-P. Harri, S. Leutwyler and E. Schumacher, "Nozzle design yielding interferometrically flat fluid jets for use in single-mode dye lasers," *Review of Scientific Instruments* 53(12), 1855-1858 (1982)
- G. He and S. H. Liu, *Physics of Nonlinear Optics*, World Scientific Publishing Company Incorporated (1999).
- H. G. Heard and J. Peterson, "Super-Radiant Yellow and Orange Laser Transitions in Pure Neon," *Proc. IEEE* 52(10), 1258 (1964)
- D. Hecht, W. Bond, R. Pantell and H. Puthoff, "Dye lasers with ultrafast transverse flow," *IEEE Journal of Quantum Electronics* 8(1), 15-19 (1972)
- J. L. Herek, W. Wohlleben, R. J. Cogdell, D. Zeidler and M. Motzkus, "Quantum control of energy flow in light harvesting," *Nature* 417(6888), 533-535 (2002)
- R. J. Hill, [3/29/2010, notebook 2, page 90] *Unpublished raw data.* (2010)
- W. Holzer, M. Mauerer, A. Penzkofer, R. M. Szeimies, C. Abels, M. Landthaler and W. Bäuml, "Photostability and thermal stability of indocyanine green," *Journal of Photochemistry and Photobiology B: Biology* 47(2–3), 155-164 (1998)
- J. Hua, P. Wang and M. Wang, "Fourier interferometry for spaceborne atmospheric sounding," *Proceedings of SPIE* 4891(169-179 (2003)

- J. D. Hybl, A. W. Albrecht, S. M. Gallagher Faeder and D. M. Jonas, "Two-Dimensional Electronic Spectroscopy," *Chemical Physics Letters* 297(307-313 (1998)
- D. Ionascu, F. Rosca, F. Gruia, A. Yu and P. M. Champion, "Optical scanning instrument for ultrafast pump-probe spectroscopy of biomolecules at cryogenic temperatures," *Review of Scientific Instruments* 77(6), 064303-064307 (2006)
- K. Iwasawa, A. Iwama and K. Mitsui, "Development of a measuring method for several types of programmed tool paths for NC machine tools using a laser displacement interferometer and a rotary encoder," *Precision Engineering* 28(4), 399-408 (2004)
- P. P. Jha and P. Guyot-Sionnest, "Trion Decay in Colloidal Quantum Dots," *ACS Nano* 3(4), 1011-1015 (2009)
- D. M. Jonas, "Two-dimensional femtosecond spectroscopy," *Annual Review of Physical Chemistry* 54(1), 425-463 (2003)
- D. M. Jonas, M. J. Lang, Y. Nagasawa, T. Joo and G. R. Fleming, "Pump-probe polarization anisotropy study of femtosecond energy transfer within the photosynthetic reaction center of *Rhodobacter sphaeroides* R26," *Journal of Physical Chemistry* 100(30), 12660-12673 (1996)
- D. J. Jones, E. O. Potma, J. X. Cheng, B. Burfeindt, Y. Pang, J. Ye and X. S. Xie, "Synchronization of two passively mode-locked, picosecond lasers within 20 fs for coherent anti-Stokes Raman scattering microscopy," *Rev. Sci. Instrum.* 73(8), 2843-2848 (2002)
- P. Kambhampati, "Unraveling the Structure and Dynamics of Excitons in Semiconductor Quantum Dots," *Accounts of Chemical Research* 44(1), 1-13 (2010)
- I. Kang and F. W. Wise, "Electronic structure and optical properties of PbS and PbSe quantum dots," *Journal of the Optical Society of America* 14(7), 1632-1646 (1997)
- H. H. Karow, *Fabrication Methods for Precision Optics*, Wiley, New York (1993).
- W. Kiefer and H. J. Bernstein, "A Cell for Resonance Raman Excitation with Lasers in Liquids," *Applied Spectroscopy* 25(4), 500-501 (1971)
- V. Klimov, A. Mikhailovsky, S. Xu, A. Malko, J. Hollingsworth, C. Leatherdale, H. J. Eisler and M. Bawendi, "Optical gain and stimulated emission in nanocrystal quantum dots," *SPIE milestone series* 180(366-369 (2005)
- V. I. Klimov, A. Mikhailovski, J. A. Hollingsworth, C. A. Leatherdale and M. G. Bawendi, "Optical amplifiers and lasers," *US Patent 6819692* (2004)

- S. Kolodinski, J. H. Werner, T. Wittchen and H. J. Queisser, "Quantum efficiencies exceeding unity due to impact ionization in silicon solar cells," *Applied Physics Letters* 63(17), 2405-2407 (1993)
- D. Kraemer, M. L. Cowan, A. Paarmann, N. Huse, E. T. J. Nibbering, T. Elsaesser and R. J. D. Miller, "Temperature dependence of the two-dimensional infrared spectrum of liquid H₂O," *Proceedings of the National Academy of Sciences of the United States of America* 105(2), 437-442 (2008)
- M. Law, J. M. Luther, Q. Song, B. K. Hughes, C. L. Perkins and A. J. Nozik, "Structural, Optical, and Electrical Properties of PbSe Nanocrystal Solids Treated Thermally or with Simple Amines," *Journal of the American Chemical Society* 130(18), 5974-5985 (2008)
- W.-K. Lee, H. S. Suh and C.-S. Kang, "Vacuum wavelength calibration of frequency-stabilized He-Ne lasers used in commercial laser interferometers," *Opt. Eng.* 50(5), 054301 (2011)
- E. Lill, S. Schneider and F. Dörr, "Passive mode-locking of a flashlamp-pumped fluorol 7GA dye laser in the green spectral region," *Optics Communications* 20(2), 223-224 (1977)
- G. Nair, S. M. Geyer, L.-Y. Chang and M. G. Bawendi, "Carrier multiplication yields in PbS and PbSe nanocrystals measured by transient photoluminescence," *Physical Review B* 78(12), 125325 (2008)
- M. Lim, T. A. Jackson and P. A. Anfinsen, "Nonexponential protein relaxation: dynamics of conformational change in myoglobin," *Proceedings of the National Academy of Sciences of the United States of America* 90(12), 5801-5804 (1993)
- M. S. Lipkins, "Hollow retroreflector mount," *US Patent 3,977,765* (1976)
- M. S. Lipkins, "Method and Device for Assembling Hollow Retroreflectors," *US Patent 3,936,194* (1976)
- J. L. Lubbeck, K. M. Dean, H. Ma, A. E. Palmer and R. Jimenez, "Microfluidic Flow Cytometer for Quantifying Photobleaching of Fluorescent Proteins in Cells," *Analytical Chemistry* 84(9), 3929-3937 (2012)
- J. Luoma, J. Schumann and E. C. Traube, "Effects of retroreflector positioning on nighttime recognition of pedestrians," *Accident Analysis & Prevention* 28(3), 377-383 (1996)
- J. M. Luther, M. C. Beard, Q. Song, M. Law, R. J. Ellingson and A. J. Nozik, "Multiple exciton generation in films of electronically coupled PbSe quantum dots," *Nano Letters* 7(6), 1779-1784 (2007)

- J. J. Lyons and P. A. Hayes, "High-optical-quality cryogenic hollow retroreflectors," *Proc. SPIE* 2540(15 September), 94-100 (1995)
- Y. F. Ma, H. J. Li, J. P. Lin and X. Yu, "Greatly improved stability of passively Q-switched Ce:Nd:YAG laser by using corner cube prism," *Laser Phys.* 20(9), 1802-1805 (2010)
- B. Marchon and T. Olson, "Magnetic Spacing Trends: From LMR to PMR and Beyond," *IEEE Transactions on Magnetics* 45(10), 3608-3611 (2009)
- J. A. McGuire, J. Joo, J. M. Pietryga, R. D. Schaller and V. I. Klimov, "New Aspects of Carrier Multiplication in Semiconductor Nanocrystals," *Accounts of Chemical Research* 41(12), 1810-1819 (2008)
- A. G. Midgett, H. W. Hillhouse, B. K. Hughes, A. J. Nozik and M. C. Beard, "Flowing versus Static Conditions for Measuring Multiple Exciton Generation in PbSe Quantum Dots," *The Journal of Physical Chemistry C* 114(41), 17486-17500 (2010)
- K. Misawa and T. Kobayashi, "Femtosecond Sagnac interferometer for phase spectroscopy," *Optics Letters* 20(1550-1552) (1995)
- J. H. Moore, C. C. Davis, M. A. Coplan and S. C. Greer, *Building Scientific Apparatus*, Cambridge University Press, New York (2009).
- I. Moreels, K. Lambert, D. De Muynck, F. Vanhaecke, D. Poelman, J. C. Martins, G. Allan and Z. Hens, "Composition and size-dependent extinction coefficient of colloidal PbSe quantum dots," *Chemistry of Materials* 19(25), 6101-6106 (2007)
- G. Nair, L.-Y. Chang, S. M. Geyer and M. G. Bawendi, "Perspective on the prospects of a carrier multiplication nanocrystal solar cell," *Nano letters* 11(5), 2145-2151 (2011)
- K. K. Nanda, F. E. Kruis, H. Fissan and S. N. Behera, "Effective mass approximation for two extreme semiconductors: Band gap of PbS and CuBr nanoparticles," *Journal of Applied Physics* 95(9), 5035-5041 (2004)
- "NIST Atomic Spectra Database Levels Data (Ne I)," <http://physics.nist.gov/cgi-bin/ASD/energy1.pl>
- I. Notinger, R. E. Imhof, P. Xiao and F. C. Pascut, "Spectral Depth Profiling of Arbitrary Surfaces by Thermal Emission Decay – Fourier Transform Infrared Spectroscopy," *Applied Spectroscopy* 57(12), 1494-1501 (2003)
- A. J. Nozik, "Spectroscopy and hot electron relaxation dynamics in semiconductor quantum wells and quantum dots," *Annual Review of Physical Chemistry* 52(1), 193-231 (2001)

- P. Nuernberger, G. Krampert, T. Brixner and G. Vogt, "Rotation-translation device for condensed-phase spectroscopy with small sample volumes," *Review of Scientific Instruments* 77(8), 083113-083116 (2006)
- J. Oberle, E. Abraham, A. Ivanov, G. Jonusauskas and C. Rulliere, "Picosecond CARS and transient absorption studies of 1,4-diphenylbutadiene and trans-stilbene: A study of photoinduced formation of a radical cation," *Journal of Physical Chemistry* 100(24), 10179-10186 (1996)
- J. J. Peterson and T. D. Krauss, "Fluorescence Spectroscopy of Single Lead Sulfide Quantum Dots," *Nano Letters* 6(3), 510-514 (2006)
- W. K. Peters, B. Cho, R. J. Hill, T. L. Courtney and D. M. Jonas, "Band Filling Dynamics and Auger Recombination in Lead Sulfide Nanocrystals," in *Ultrafast Phenomena XVII*, Oxford University Press, New York (2010).
- J. Piel, E. Riedle, L. Gundlach, R. Ernstorfer and R. Eichberger, "Sub-20 fs visible pulses with 750 nJ energy from a 100 kHz noncollinear optical parametric amplifier," *Optics Letters* 31(9), 1289-1291 (2006)
- N. Poklonskii, A. Syaglo and S. Vyrko, "Analog of the Auger effect in radiative decay of a trion in a quantum well," *Journal of Applied Spectroscopy* 68(3), 371-376 (2001)
- A. Preston and S. Merkwitz, "Hollow Retroreflectors for Lunar Laser Ranging at Goddard Space Flight Center," in *International Technical Laser Workshop 2012 (ITLW-12)* M. Pearlman and S. Dell'Agnello, Eds., pp. Thursday 8 November, Session 6: Talk 2, Frascati (Rome), Italy (2012).
- N. Pugliano, S. Gnanakaran and R. M. Hochstrasser, "The dynamics of photodissociation reactions in solution," *Journal of Photochemistry and Photobiology A: Chemistry* 102(1, Supplement 1), 21-28 (1996)
- H. S. Rana and N. B. Mullett, "Fabrication challenges in large prisms," *Proc. SPIE* 4411(5 February), 140-141 (2002)
- I. Rasnik, S. A. McKinney and T. Ha, "Nonblinking and long-lasting single-molecule fluorescence imaging," *Nature Methods* 3(11), 891-893 (2006)
- Y. I. Ravich, "Lead Chalcogenides: Basic Physical Features," in *Lead Chalcogenides: Physics & Applications* D. Khokhlov, Ed., pp. 3-34, Taylor and Francis, New York (2003).
- S. Y. Ren, "Quantum confinement of edge states in Si crystallites," *Physical Review B* 55(7), 4665-4669 (1997)
- F. Rosca, A. T. N. Kumar, D. Ionascu, T. Sjodin, A. A. Demidov and P. M. Champion, "Wavelength selective modulation in femtosecond pump-probe spectroscopy and its

- application to heme proteins," *The Journal of Chemical Physics* 114(24), 10884-10898 (2001)
- R. Rossetti, S. Nakahara and L. E. Brus, "Quantum size effects in the redox potentials, resonance Raman spectra, and electronic spectra of CdS crystallites in aqueous solution," *The Journal of Chemical Physics* 79(2), 1086-1088 (1983)
- J. B. Sambur, T. Novet and B. A. Parkinson, "Multiple Exciton Collection in a Sensitized Photovoltaic System," *Science* 330(6000), 63-66 (2010)
- R. D. Schaller and V. I. Klimov, "High Efficiency Carrier Multiplication in PbSe Nanocrystals: Implications for Solar Energy Conversion," *Physical Review Letters* 92(18), 186601 (2004)
- O. E. Semonin, J. M. Luther, S. Choi, H.-Y. Chen, J. Gao, A. J. Nozik and M. C. Beard, "Peak External Photocurrent Quantum Efficiency Exceeding 100% via MEG in a Quantum Dot Solar Cell," *Science* 334(6062), 1530-1533 (2011)
- D. T. Shen, "Frameless Hollow Roof Mirror and Method of Manufacture," *US Patent* 7,324,733 B2 (2008)
- M. E. Siemens, G. Moody, H. Li, A. D. Bristow and S. T. Cundiff, "Resonance lineshapes in two-dimensional Fourier transform spectroscopy," *Optics Express* 18(17), 17699-17708 (2010)
- A. P. Spencer, R. J. Hill, W. K. Peters, D. V. Baranov and D. M. Jonas, "Shot-to-shot Sample Renewal Using Beam Scanning with Applications to Pump-Probe Spectroscopy," *Review of Scientific Instruments* (To be submitted)
- W. H. Steel, *Interferometry*, Cambridge University Press, Cambridge (1967).
- J. T. Stewart, L. A. Padilha, M. M. Qazilbash, J. M. Pietryga, A. G. Midgett, J. M. Luther, M. C. Beard, A. J. Nozik and V. I. Klimov, "Comparison of Carrier
- J. W. Stouwdam, J. Shan, F. van Veggel, A. G. Pattantyus-Abraham, J. F. Young and M. Raudsepp, "Photostability of colloidal PbSe and PbSe/PbS core/shell nanocrystals in solution and in the solid state," *Journal of Physical Chemistry C* 111(3), 1086-1092 (2007)
- S. Y. Ren, "Quantum confinement of edge states in Si crystallites," *Physical Review B* 55(7), 4665-4669 (1997)
- Multiplication Yields in PbS and PbSe Nanocrystals: The Role of Competing Energy-Loss Processes," *Nano Letters* 12(2), 622-628 (2012)
- J. T. Stewart, L. A. Padilha, M. M. Qazilbash, J. M. Pietryga, A. G. Midgett, J. M. Luther, M. C. Beard, A. J. Nozik and V. I. Klimov, "Comparison of Carrier

- Multiplication Yields in PbS and PbSe Nanocrystals: The Role of Competing Energy-Loss Processes," *Nano Letters* 12(2), 622-628 (2012)
- Y. Su and G. N. R. Tripathi, "Time-Resolved Resonance Raman Observation of Protein-Free Riboflavin Semiquinone Radicals " *Journal of the American Chemical Society* 116(10), 4405-4407 (1994)
- M. Sykora, A. Y. Kuposov, J. A. McGuire, R. K. Schulze, O. Tretiak, J. M. Pietryga and V. I. Klimov, "Effect of Air Exposure on Surface Properties, Electronic Structure, and Carrier Relaxation in PbSe Nanocrystals," *ACS Nano* 4(4), 2021-2034 (2010)
- J. Tang, L. Brzozowski, D. A. R. Barkhouse, X. H. Wang, R. Debnath, R. Wolowiec, E. Palmiano, L. Levina, A. G. Pattantyus-Abraham, D. Jamakosmanovic and E. H. Sargent, "Quantum Dot Photovoltaics in the Extreme Quantum Confinement Regime: The Surface-Chemical Origins of Exceptional Air- and Light-Stability," *ACS Nano* 4(2), 869-878 (2010)
- M. J. Tauber, R. A. Mathies, X. Chen and S. E. Bradforth, "Flowing liquid sample jet for resonance Raman and ultrafast optical spectroscopy," *Review of Scientific Instruments* 74(11), 4958-4960 (2003)
- B. N. Toleutaev, T. Tahara and H. Hamaguchi, "Broadband (1000 cm⁻¹) multiplex CARS spectroscopy: Application to polarization sensitive and time-resolved measurements," *Applied Physics B* 59(4), 369-375 (1994)
- D. B. Turner, Y. Hassan and G. D. Scholes, "Exciton Superposition States in CdSe Nanocrystals Measured Using Broadband Two-Dimensional Electronic Spectroscopy," *Nano Letters* 12(2), 880-886 (2011)
- P. Tyagi and P. Kambhampati, "False multiple exciton recombination and multiple exciton generation signals in semiconductor quantum dots arise from surface charge trapping," *Journal of Chemical Physics* 134(9), 10 (2012)
- B. Wellegehausen, H. Welling and R. Beigang, "A narrowband jet stream dye laser," *Applied Physics* 3(5), 387-391 (1974)
- B. A. West, J. M. Womick and A. M. Moran, "Influence of temperature on thymine-to-solvent vibrational energy transfer," *The Journal of Chemical Physics* 135(11), 114505-114509 (2011)
- B. A. West and A. M. Moran, "Two-Dimensional Electronic Spectroscopy in the Ultraviolet Wavelength Range," *The Journal of Physical Chemistry Letters* 3(18), 2575-2581 (2012)
- F. W. Wise, "Lead Salt Quantum Dots: the Limit of Strong Quantum Confinement," *Accounts of Chemical Research* 33(11), 773-780 (2000)

- Y. Yamamoto, S. Nishida, X. H. Ma and K. Hayashi, "Pulse radiolysis of trans-stilbene in tetrahydrofuran. Spectral shift and decay kinetics of the radical anions in the presence of quaternary ammonium salts," *The Journal of Physical Chemistry* 90(9), 1921-1924 (1986)
- M. K. Yetzbacher, T. L. Courtney, W. K. Peters, K. A. Kitney, E. R. Smith and D. M. Jonas, "Spectral restoration for femtosecond spectral interferometry with attosecond accuracy," *J. Opt. Soc. Am. B* 27(5), 1104-1117 (2010)
- P. R. Yoder, "Mounting optics in optical instruments," SPIE-International Society for Optical Engineering (2008).
- P. Yoder Jr, "High Precision 10-cm Aperture Penta and Roof-Penta Mirror Assemblies," *Applied Optics* 10(10), 2231-2234 (1971)
- T. Yoshizawa and G. Wald, "Pre-Lumirhodopsin and the Bleaching of Visual Pigments," *Nature* 197(4874), 1279-1286 (1963)
- L. A. Yurs, S. B. Block, A. V. Pakoulev, R. S. Selinsky, S. Jin and J. Wright, "Multiresonant Coherent Multidimensional Electronic Spectroscopy of Colloidal PbSe Quantum Dots," *Journal of Physical Chemistry C* 115(46), 22833-22844 (2011)
- W. W. Yu, J. C. Falkner, B. S. Shih and V. L. Colvin, "Preparation and Characterization of Monodisperse PbSe Semiconductor Nanocrystals in a Noncoordinating Solvent," *Chemistry of Materials* 16(17), 3318-3322 (2004)
- T. Zhang, C. Borca, X. Li and S. Cundiff, "Optical two-dimensional Fourier transform spectroscopy with active interferometric stabilization," *Opt. Express* 13(19), 7432-7441 (2005)
- H. Zhu, Y. Yang and T. Lian, "Multiexciton Annihilation and Dissociation in Quantum Confined Semiconductor Nanocrystals," *Accounts of Chemical Research* (2012)
- X. R. Zhu and J. M. Harris, "Studies of excited state absorption and photoisomerization of cyanine dyes by using laser induced anharmonic thermal gratings," *JOSA B* 7(5), 796-802 (1990)

APPENDIX A: HOLLOW ROOFTOP MIRROR CONSTRUCTION

The literature on hollow retroreflectors is sparse. Technical drawings may be reported but without great detail, omitting important aspects such as jig construction and adhesives. Procedural details can greatly affect the precision and stability of bond angles in hollow retroreflectors and have therefore been included here.

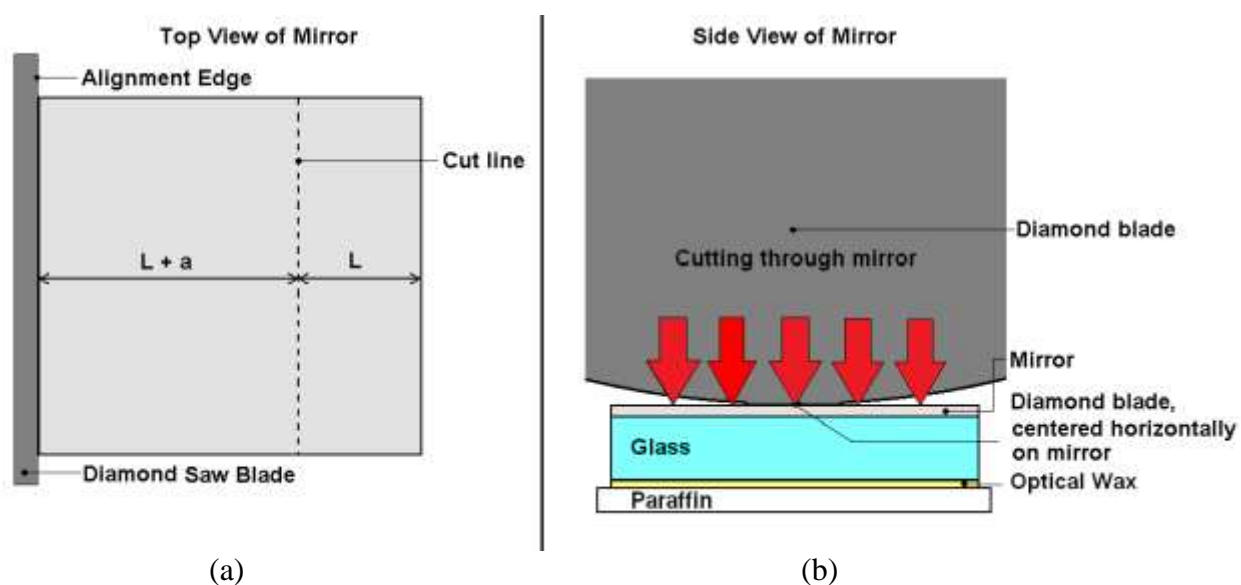


Fig. A.1. Cutting the retroreflector glass. (a) Saw blade alignment. (b) Cutting through substrate

The saw stage for mounting the surface to be cut has three degrees of freedom: two for translation and the other for rotation. Before mounting the mirror to the paraffin (as in Figure A.1), the saw was slowly dropped down vertically into the cutting plane over the mirror while adjusting a combination of the sample stage's rotation and two translational degrees (shown in Figure A.2) until the diamond blade barely grazes the edge of the paraffin, and rests with the blade tip approximately mid-center of the paraffin. This will allow the blade to drop to a depth at which it will ultimately make a vertical cut through the mirror, optical wax, and backing paraffin.

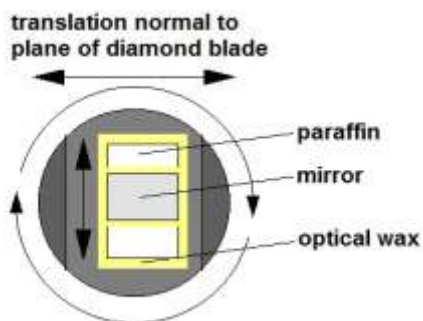


Fig. A.2. Aligning the retroreflector glass for cutting. The two translation and one rotational degrees of freedom of the sample stage show that one can set the position so that the diamond blade barely grazes the mirror edge. The blade should slice into the plane parallel to the vertical arrow. The rotation sets the face of the paraffin parallel to the blade, the “x-axis” translation along the horizontal arrow in the drawing moves that face into the blade for alignment and final cut, while the “y-axis” translation along the vertical arrow in the drawing allows the user to put the blade onto approximately midpoint of the paraffin.

Using hot optical wax, the mirror was then mounted to the paraffin mounting base on the diamond saw. The paraffin base allows cutting beyond the mirror without damaging the blade. A heat gun was then used to heat little bits of optical wax until barely liquid on the paraffin base, and the mirror was quickly transferred to the base. The melted optical wax layer was thin (less than 0.25 mm). Gloves were worn and only the edges of the mirror handled so as to minimize transfer of finger oils to the mirror. The mirror was pressed parallel to the blade, as in Figure A.1(a), and was firmly pressed flush against the paraffin mounting base. The side of the mirror was placed so that it barely grazed the thin and fragile diamond blade without deflecting it. Minor adjustments were made to the saw blade offset and to the stage rotation as necessary to accomplish this.

The base the paraffin was mounted to was slip-displaced parallel to the blade so that the blade touched, horizontally centered, at a single point of contact, as shown in Figure A.1(b). This was done by eye, using the side view of the mirror to ensure centering. The blade should *not* touch the mirror. Centering the blade allows an evenly forced cut through the mirror while

minimizing cutting time. With the blade barely grazing the edge of the mirror, the position of the micrometer was recorded. The blade was lifted and the micrometer displaced from its initial position at the alignment edge, a total displacement of $L+a$. This yielded a cut into the mirror, subdividing the total length $2L+a$ into L and $L+a$. The pressure on the blade was supplied by the adjustable counterweight on the saw (see diamond saw manual). A cut was then begun through the mirror, ensuring that the diamond saw blade never ran dry during its operation, and applying no more pressure on the mirror than required to make a smooth cut (not bending the blade).

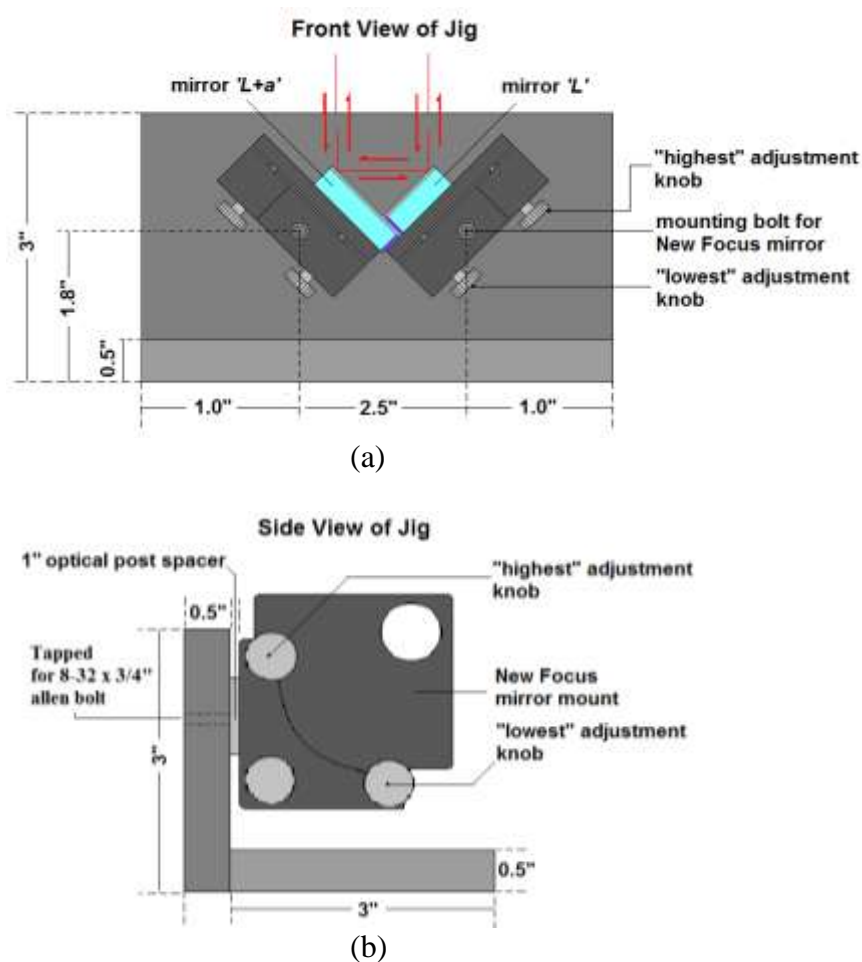


Fig. A.3. The retroreflector jig (a) Front view of the jig showing alignment knobs. The standard mirror mounts are bolted to a fabricated “L-shaped” block for support in the Fizeau interferometer. The highest adjustment knob above mounting bolt adjusts angle between hollow dihedral retroreflectors (purple denotes the cut edge). (b) Side view of the jig shows the highest and lowest adjustment knobs.

A home-built jig was assembled using two mirror mounts (New Focus, 9809 Classic Corner Mirror Mounts) mounted on a “wall,” with 8-32 bolts $\frac{3}{4}$ in. in length at an angle of approximately 90° with respect to each other and at an angle of 45 degrees with respect to the base, as shown in Figures A.3(a) and A.3(b). The home-built jig was constructed by bolting two plates, $4.5 \times 3 \times 0.5$ in. lengthwise, with $\frac{1}{4}$ -20 bolts. The cut edge of the mirror is shown in purple.

The mirrors were placed on the jig in the Fizeau interferometer as shown in Figure A.4. Looking down on the hollow rooftop mirror (HRM) from the top, the trough (where the mirrors form a joint) of the HRM was perpendicular to the front of the Fizeau (see Figure A.4).

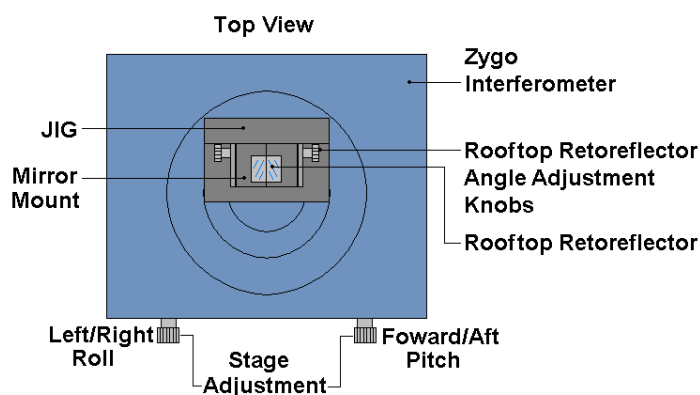


Fig. A.4. Inside the Zygo® Fizeau interferometer. Positioning the retroreflector assembly jig for alignment of the retroreflector.

This vertical alignment helped later in characterization and adjustment of the mirror angles, as it decoupled the angular alignment of the mirrors from the pitch or roll of the stage alignment. The HRM was located approximately in the smallest circle of the Fizeau centering marks, as shown in Figure A.4. This configuration may not be achievable on the first placement of the jig if the laser guide spot of the Fizeau is not present on the monitor, and if no amount of Fizeau stage adjustment will put it there.

The Fizeau uses a laser guide spot to aid in rough alignment of the optics by sending a beam to the optic and recording a return signature to a camera. The image shows up on a monitor with crosshairs for alignment purposes. In the simple case of a flat mirror, a single spot can be seen. Because there are two mirrors, not aligned at 90° with respect to each other, the spot will reflect off of two different mirrors to point to two different spots. The spots may not show up at all, and the jig may have to be rotated to see them. Once these spots are visible on the monitor screen, adjustment knobs were to used (Figure A.4) to guide the laser spot, or spots, until they were in the crosshairs. The right stage adjustment knob aligned front to aft (in pitch), while the left stage adjustment knob aligned right to left (in roll) of the Fizeau stage. As it is necessary to see the spots for alignment, the whole jig assembly may have to be rotated on the Fizeau stage until the spots show up; then the jig can be aligned to the position shown in Figure A.4 by switching back and forth between stage alignment and rotation of the jig.

Once the spots were visible on the screen, the left-right roll adjustment knob was not adjusted. All alignment along the left-right axis was done with the highest knob on the mirror mount of Figure A.3(a). Either “highest knob” may be chosen, but only one, so as to minimize the probability of the mirrors sliding with respect to each other along the optic mounts. A set of spots horizontally opposite each other across the vertical crosshair indicates that there are two return signatures off the HRM and that the mirror surfaces are not yet at 90° (see Fig. A.5(a)). When these spots were centered on the crosshairs as in Fig. A.5(b), then the two mirrors were aligned to $\sim 90^\circ$ with respect to each other.

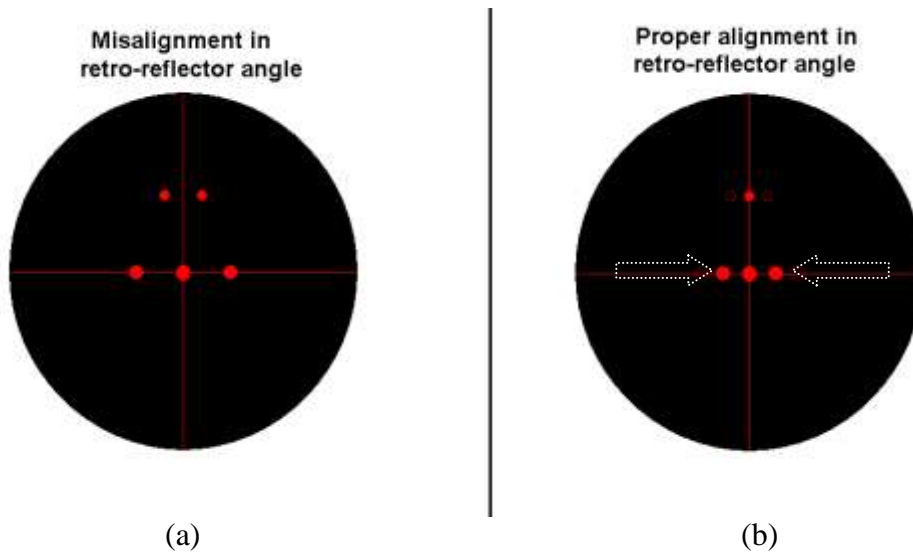


Fig. A.5. Rough retroreflector alignment (a) The retroreflector is too obtuse. (b) The correction to 90° is made by adjusting the highest knobs in the jig, shown in Figure A.3(a). Spots move toward the vertical crosshairs, indicated in direction by white arrows, as the highest knob is adjusted.

Adjusting the highest knob on the jig (see Figure A.3(a)) had the effect of spreading or contracting the mirrors apart at an angle, moving the spots closer together or farther apart. If the angle is too obtuse or too acute, then the two spots will move toward the vertical crosshairs as the angle approaches 90° . The goal of this part of the process was to adjust the mirrors until the two spots became a single spot on the vertical crosshair (in the alignment of Fizeau), and to move that spot as close as possible to the horizontal crosshair by adjusting the forward/aft pitch. When this was complete, the camera in the Fizeau interferometer was switched from a view of the alignment spot to a view of the interference pattern.

The alignment of the retroreflector using the interference pattern can be thought of as a two-dimensional walk across Newton's rings, imagining that each mirror has its own set of Newton's rings on it (see Figure A.6). The goal was to get to the center of the Newton rings on each mirror surface. When this occurred, the test beam, which was larger than both retroreflector

mirrors, was phase constant across the entire surface of the retroreflector. This was specified by a degree of phase flatness in units of λ (632.8 nm). It is straightforward to see that a beam of finite size incident to the retroreflector will return to its original direction with the phase on one side of the beam swapping places with the phase on the other side of the beam. For a plane wave front, symmetrical in radius, nothing will change if the retroreflector mirrors are at 90° , the line of intersection between mirrors is parallel to the wavefront, and the retroreflector is centered on the beam. Consequently, a good retroreflector will look no different from a flat mirror aligned perfectly normal to the incident beam.

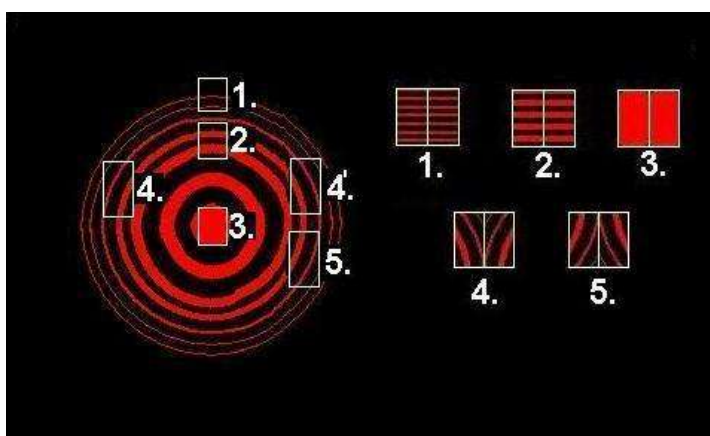


Fig. A.6. Fine retroreflector alignment. Alignment of the retroreflectors is a 2D walk across Newton's rings. The numbers on the left indicate where on Newton's rings one would expect to create the image of the retroreflectors on the right. Misalignment in retroreflector angle, for example, might look like it is passing from 4' to a fringe pattern approximately midway between 2 and 3 at 90° , then continuing to 4' as it is aligned from acute to obtuse angles. Walking from 1 to 2 to 3 is a 90° degree retroreflector that requires forward/aft pitch adjustment along the direction of the mirror crease, as shown in Figure A.4.

Mounting for Final Alignment

With the number of fringes on each mirror minimized, the jig was removed and some wax melted on only one of the mirror mounts in the jig. The longer of the two mirrors, length $L+a$, was quickly pressed flush into the hot wax on the mirror mount, ensuring that its edge barely grazed the opposite mirror mount. The hot wax was then allowed to solidify. If

mechanical interference exists between the longer mirror and the other (opposite) mirror mount, then it will not allow for angular adjustment of each mirror mount. If the longer mirror is not close enough to the opposite mirror mount, then the second mirror will not make good contact when they are bonded. The second mirror was set loosely on top of the longer mirror, as shown in Figure 2(a).

Bonding and Final Alignment

The rough alignment procedure was repeated with the short mirror, length L , resting on top of the first mirror, $L+a$ [see Figure A.3(a)]. When the retroreflectors were aligned at a 90° angle, the smaller mirror L was removed. A thin layer of mixed Torr Seal epoxy was placed on the end of the smaller mirror L , which was mounted to the longer mirror $L+a$. The amount of Torr Seal required was about half the diameter of a toothpick, and was applied using a toothpick by dabbing in a thin bead along the entire side. The goal is to use a sufficient amount of Torr Seal to form a solid bond, but not so much that excess drips out the sides. The Torr Seal was placed in the central one-third of the cut side of the mirror with length L (see the inset of Figure 1).

The mirror was then slid slowly down the mirror mount, using the mount as a guide, until the side of the mirror with length L rested on the reflective surface of the longer mirror, as shown in Figure 2.1. Adjustments to the retroreflector pair were made with the highest adjustment knob, shown in Figure A.3. This was done while keeping the return phase front as flat as possible, with a single fringe goal in mind (each mirror should have approximately one fringe on it).

Mounting Side Support

A small layer of Torr Seal was applied to the side of the central third of the retroreflector [as shown in Figure 2.2(a)] using a dab—about half the diameter of a toothpick—on the inner

side in the same manner as before. The shield shaped plate in Figure 2.2 was allowed to dry with the shield on top while the retroreflector rested on its side. It was allowed to dry on its side for 24 h. Only one side was bonded at a time in order to avoid misalignment and the risk of smearing Torr Seal onto the mirrored surface. Waiting to assemble each side on a separate day also allowed for characterization in careful steps, ensuring that nothing happened to misalign the otherwise well-aligned retroreflectors. Torr Seal may be pulled apart with application of a heat gun if a second attempt is necessary.

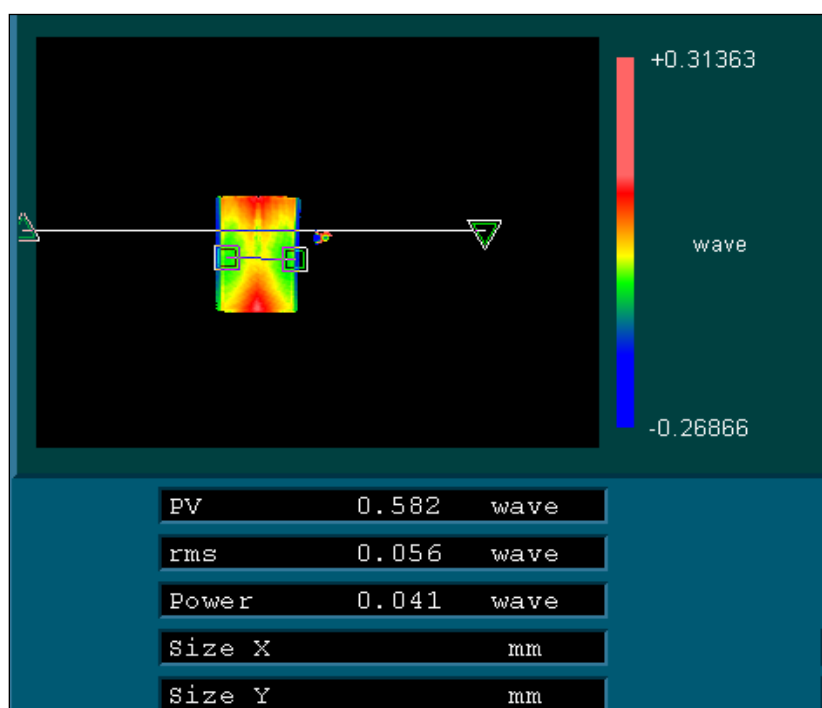


Fig. A.7. Completed Retroreflector 1 surface. Root mean squared (rms) 0.056 wave ($\lambda/20$) across the rooftop retroreflector. Mass 3.3914 \pm 0.0001 g. PV, *peak-to-valley*, is the distance in waves between the highest and lowest phase points within the sampled surface. *rms*, is root-mean-squared deviation from a centerline fit. In this case, the center line fit subtracted tilt and offset off the phase surface. Power is a measure of curvature in the wavefront, taking the difference between the center of the wavefront and the point farthest from the center, in cylindrical coordinates. The PV is not an accurate reflection of the phase across the surface because most of the large blue, negative phase region, is off a beveled edge of the mirror. This type of characterization error was corrected with a mask, distinguishing differences in reported values between Figures A.8 and A.9.

A cross section of the rooftop retroreflector in Figure A.8 shows approximately an rms roughness of $\lambda/20$, corresponding to ~ 31.6 nm rms. This horizontal rms profile is typical for any vertical translation across the retroreflector. Accounting for unique optical paths, this would allow 48 individual (200 μm diameter), non-overlapping beams to be stacked across the 9.5 mm \times 13.8 mm surface and for 69 non-overlapping beams to be stacked vertically. A usable surface area for multiple beams is of primary importance in the Mach–Zehnder interferometer where we want to pass a broadband laser source through a beam splitter while spatially displacing the narrowband reference lasers used for locking and measuring displacement.

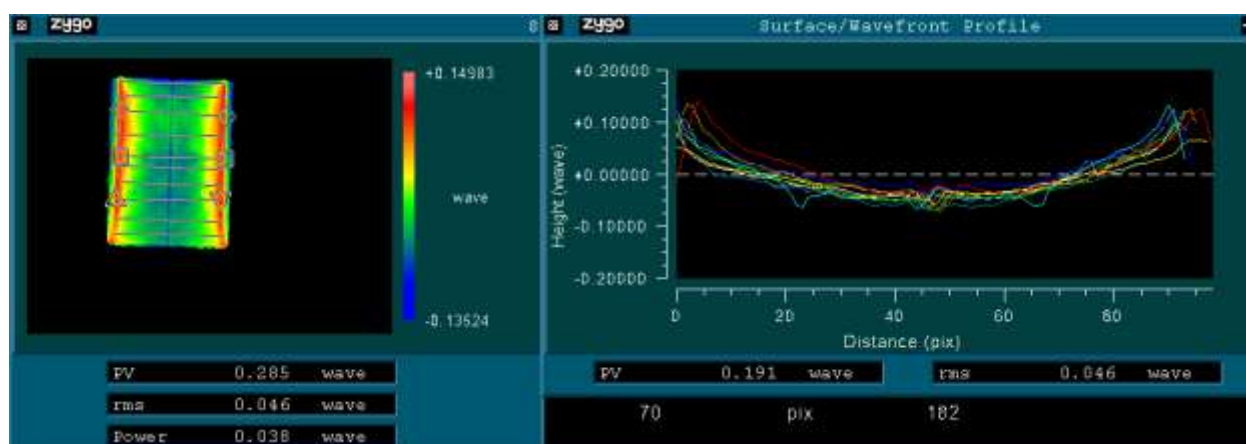


Fig. A.8. Completed Retroreflector 2 surface. Root mean squared (rms) of 0.046λ , where $\lambda = 632.8$ nm characterizes the surface roughness across the rooftop retroreflector surface. The software set a centerline for rms based on a fit to a tilted plane. Without a mask applied, this includes all of the noise from the edges. On the right, horizontal cross sectional profiles show phase height expressed as a fraction of λ , and insets report peak-to-valley and rms for a sample cross section. The total mass, including the base, is 3.2141 grams \pm 0.0001 g.

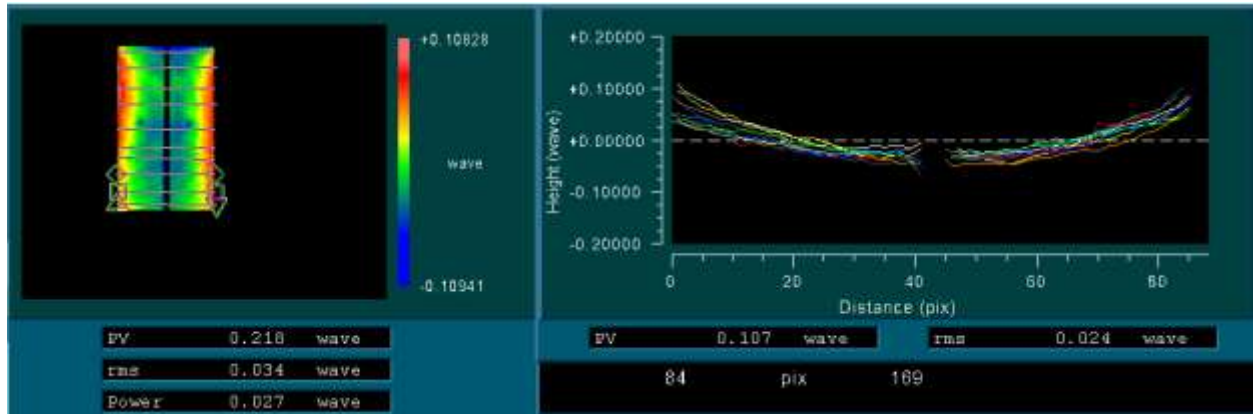


Fig. A.9. The effects of measurement masks on PV, rms, and power characteristics of the hollow retroreflector mirror. By applying the mask, the noise from the edges is removed. Comparing this with the uncorrected portion in Figure A.8, the peak to valley is reduced by about 25%.

APPENDIX B: FLUID SAMPLE CELL CONSTRUCTION

ALTERNATIVE SOURCES OF HARD DISK GLASS SUBSTRATE

Due to a difficulty in procuring hard disk drive glass, initial designs utilized glass that could be sourced from a variety of laptop hard disk drives. The glass substrate, used in hard disk drives as a storage medium, is often coated in a proprietary blend of cobalt alloy and some amount of platinum. The coatings are impervious to both aqua regia and boiled piranha solution. The electrochemical removal of the hard disk coatings proved somewhat successful. A 12 V, 800 mA current-limited, DC wall transformer was used to drive the electrochemical reaction. The substrate disk is lowered into a solution bath of 14.099 g cupric sulfate pentahydrate dissolved in 150 mL of deionized water. The coating is removed at the air-water interface where the cathode is slowly scanned across the surface of the substrate. As the coating is completely removed at the air-water boundary, the substrate is progressively lowered into solution until the entire coating is removed. The residual surface was cleaned with aqua regia. The yield of this process was about 1 clear substrate cleaned per 16 attempted.

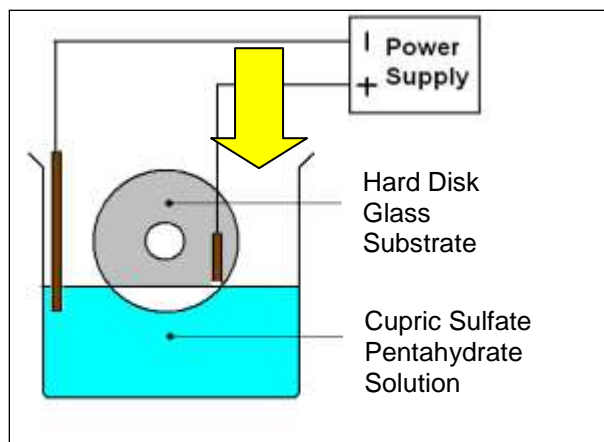


Fig. B.1. Electrochemical removal of hard disk drive coatings. The metalized hard disk drive substrate is slowly lowered into solution. The positive electrode remains at the interface between water and air, just barely inserted into the solution. As the substrate is slowly lowered into solution, the tip of the positive electrode scans the substrate surface to remove the coatings.

GLASS SUBSTRATE SELECTION

Each glass substrate was hand-selected after characterizing the two-dimensional surface phase profile in the Fizeau interferometer, (Zygo, GPI-XP). Figure B.2 indicates that certain substrates have defects that may scatter light, making them unfit for low-noise spinning experiments.

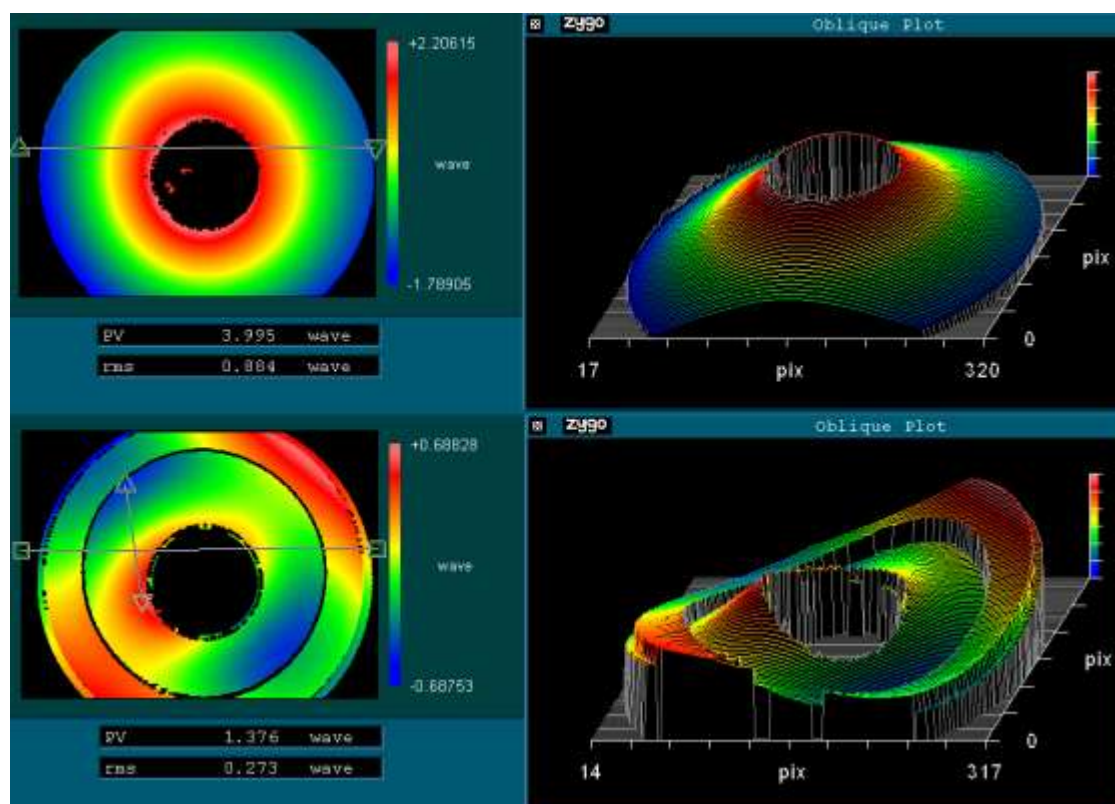


Fig. B.2.: Comparison between glass substrate surfaces. The same Fizeau interferometer, (Zygo, GPI-XP), used to characterize the rooftop retroreflectors in Chapter 2 was used to examine the surface quality of the hard disk drive glass substrates. To set the horizontal scale the hole in the middle of the disk is exactly 20 mm diameter, while everything labeled by wave units is expressed as a fraction of 632.8 nm HeNe laser light. PV (*peak-to-valley*) gives the difference between the maxima and minima of the characterized surface. The *rms* is the root mean square surface roughness. The top surface shows uninterrupted 2D spatial reflection while the bottom shows discontinuous breaks in the reflected 632.8 nm phase, suggesting localized surface height changes. In the corresponding camera image, the fringe pattern loses contrast completely in the region of phase discontinuity. The piece of glass in the lower image would not be used for a fluid disk cell. The images on the left are top views of the hard disk substrate surfaces while the images on the right are a 3-dimensional rendering of the same.

SPINNER CELL CONSTRUCTION

Key Steps in the fabrication of the spinning sample cell are illustrated in Figures B.3 to B.5.



Fig. B.3. Ring alignment for fluid cell. Rings attached to an aluminum base with double-sided Scotch tape. A spindle-sized slug in the middle was used for alignment of the glass substrate. Glue is applied to the top of both rings.



Fig. B.4. Bonding the first substrate in fluid cell. While hand pressure is applied to the glass surface, a second person cures the glue with a UV curing lamp (the UV curing lamp is turned off in the photo).

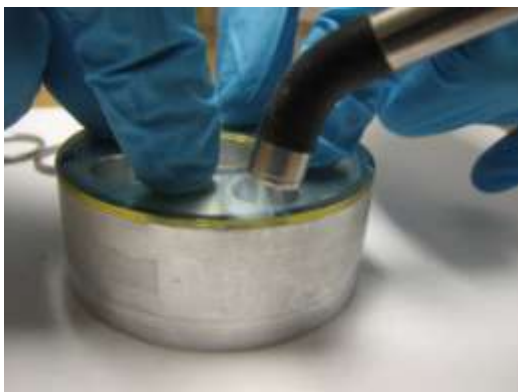


Fig. B.5. Bonding the second substrate in fluid cell. For the final step of the assembly, the first glass substrate with rings attached is flipped over. A thin layer of glue is spread over the rings, and a needle's width of extra optical glue is deposited on the interior of both titanium rings. The top glass substrate is lowered as a lid. The aluminum slug is again used for alignment and removed. Pressure is applied to the surface by hand. The outer and inner rings are sequentially cured.

OXYGEN AND MOISTURE TESTING

Placement of the vial with NaBZ and assembly of the chamber were performed in the argon-filled glovebox. First, the disassembled sample cell chamber was placed into the glovebox antechamber, and vacuum/argon cycles were applied to it for the purpose of degassing and removing physisorbed water through a form of flush desorption process.⁽¹⁾ During the cycle, the sample chamber was kept under vacuum (~ 24 Torr) for at least 5 min. and subsequently flushed with argon. This cycling process was repeated ~ 10 times. Secondly, the chamber (still disassembled) was left in the glovebox for two days before the beginning of the test.

Additionally, the O-ring was baked for 9 h at $100\text{ }^{\circ}\text{C}$ on a hotplate inside the glovebox. Thirdly, a small vial (1 mm quartz cuvette, Starna Cells, 21-G-1) was filled with a NaBZ solution (0.25 ml) and placed inside the chamber. Finally, Apiezion® L vacuum grease was applied to the O-ring as directed before the chamber was sealed. It is important to leave the closed sample chamber with NaBZ-filled cuvette in the glovebox overnight to ensure the absence of false discoloration due to “virtual leaks” from outgassing. By performing this “false positive” test, it

was found that NaBZ discolors in the presence of Scotch® Magic™ tape, which was initially used to fix the cuvette inside the chamber. Subsequent experiments did not fix the cuvette position inside the chamber. Finally, the chamber was taken out of the glovebox and stored on the lab bench wrapped in aluminum foil.

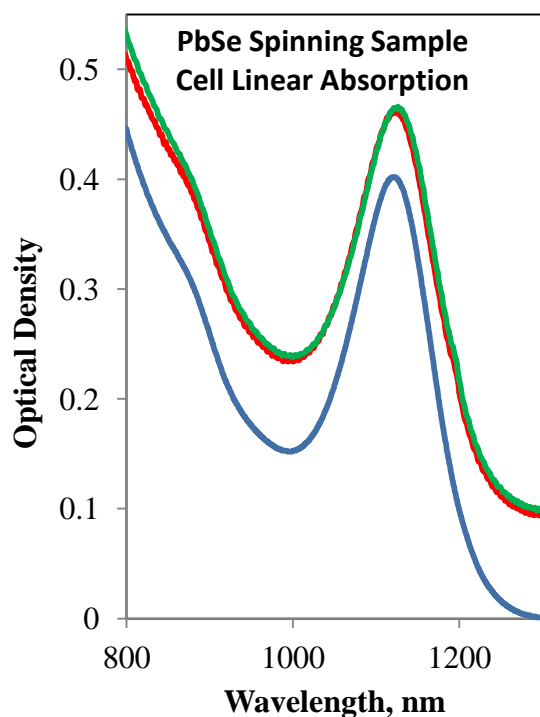


Fig. B.6. Linear absorption spectrum testing for oxygen or water in quantum dots. Comparison of the linear absorption spectra of 2.5 nm PbSe nanocrystals dispersed in hexane (dark blue) or isocetane (green, red) under different conditions. Reference spectrum (blue) of a hexane solution of freshly made PbSe nanocrystals (synthesized and processed under argon) taken in 1 mm path length quartz cuvette capped with a high vacuum valve (Chem-Vac™, CG-934-02). The absorption peak at 1121 ± 1.6 nm is attributed to the first exciton and would shift toward blue wavelengths if the absorption of oxygen or water occurred. The spectrum was taken with a Cary 500 UV-VIS-IR spectrophotometer on December 12, 2012. Green: Spectrum of the fluid sample cell filled with the isocetane solution of PbSe nanocrystals with the cell spinning (1125.5 ± 1 nm). The spectra were taken with Shimadzu UV-3101 spectrophotometer on January 7, 2013. Red: Spectrum of the same fluid sample cell as in green spectrum but recorded three days later under similar conditions (1123.5 nm, ± 1 nm). The fluid sample cell was wrapped in aluminum foil to avoid photo-bleaching.

REFERENCES FOR APPENDIX B

1. A. Berman, "Water vapor in vacuum systems," *Vacuum* 47(4), 327-332 (1996)